PETROLOGIC STUDIES OF PROCESS INTERACTIONS IN METAMORPHIC SYSTEMS: DEFORMATION AND METAMORPHISM IN THE SELKIRK ALLOCHTHON OROGENIC WEDGE; AND FEEDBACK MECHANISMS DURING REACTIVE FLUID FLOW

by

MARIE-FRANCE NATHALIE MARCHILDON

B.Sc., Université de Montréal, 1989
M.Sc., Rensselaer Polytechnic Institute, 1992

A THESIS SUBMITTED IN PARTIAL FULFILMENT OF
THE REQUIREMENTS FOR THE DEGREE OF

DOCTOR OF PHILOSOPHY

in

THE FACULTY OF GRADUATE STUDIES

(Department of Earth and Ocean Sciences; Faculty of Science)

THE UNIVERSITY OF BRITISH COLUMBIA

December 1999

© Nathalie Marchildon, 1999

National Library of Canada
Acquisitions and Bibliographic Services
395 Wellington Street
Ottawa ON K1A 0N4
Canada

Bibliothèque nationale du Canada
Acquisitions et services bibliographiques
395, rue Wellington
Ottawa ON K1A 0N4
Canada

Your file Votre référence

Our file Notre référence

The author has granted a non-exclusive licence allowing the National Library of Canada to reproduce, loan, distribute or sell copies of this thesis in microform, paper or electronic formats.

L'auteur a accordé une licence non exclusive permettant à la Bibliothèque nationale du Canada de reproduire, prêter, distribuer ou vendre des copies de cette thèse sous la forme de microfiche/film, de reproduction sur papier ou sur format électronique.

The author retains ownership of the copyright in this thesis. Neither the thesis nor substantial extracts from it may be printed or otherwise reproduced without the author's permission.

L'auteur conserve la propriété du droit d'auteur qui protège cette thèse. Ni la thèse ni des extraits substantiels de celle-ci ne doivent être imprimés ou autrement reproduits sans son autorisation.

0-612-48658-3

Canada

ABSTRACT

The first part of this thesis focuses on the tectono-metamorphic evolution of the Selkirk Allochthon, a welt of supracrustal rocks deformed and metamorphosed during Mesozoic to early Cenozoic time as a result of terrane collision at the western edge of North America. The studied area is part of the Selkirk Allochthon. Pelitic rocks in the area record a Barrovian metamorphic field gradient. Detailed mapping of metamorphic assemblage distribution and textural analysis of pelitic rocks has unraveled two distinct metamorphic events (M1 and M2). Emplacement of the Bigmouth Creek stock, which intrudes rocks of the Big Fish Creek area was dated as mid-Jurassic, with evidence for substantial reheating in early Cretaceous time. Based on regional correlation, M1 is assigned a mid-Jurassic age, synchronous with emplacement of the Bigmouth Creek stock. M2 is interpreted to have resulted from the early Cretaceous thermal event. The development of early-M2 kyanite and late-M2 andalusite indicates decompression over at least 3 kbar, implying at least 10 km of denudation. Detailed analysis of structural elements suggests that the area was part of a long-lived, mid-crustal zone of intense distributed strain. Uplift and denudation of metamorphic rocks by tectonic extension and coaxial thinning were synchronous with continued contraction. A tectono-thermal model is proposed for the Allochthon as a long-lived, dynamic orogenic wedge within which deformation accommodated contraction due to terrane convergence and accretion, and polycyclic metamorphism resulted from thickening and maintenance of the wedge over at least 20 My. Significant early Cretaceous thinning of the wedge recorded by extensional strain and late-M2 decompression resulted from waning of far-field contraction, and/or from rheological modification of the wedge due to thermal relaxation.

The second part of this thesis reports on a study of heterogeneous reactive transport of H_2O-CO_2 fluids during contact metamorphism of siliceous dolomites. Comparison of mineral assemblage distributions resulting from numerical simulations of heterogeneous flow with assemblage distribution in the Alta (Utah) contact aureole indicates that mineral reactions record flow through highly heterogeneous permeability. This is interpreted to result from positive feedback between reaction enhancement of permeability and flow-focusing. Comparison with other contact aureoles suggests that this is a common mechanism of permeability evolution during contact metamorphism of carbonate rocks. More homogeneous permeability recorded in regional metamorphic rocks may reflect fundamental differences in the relative rates of fluid flow and compaction in regional and contact metamorphic environments.

TABLE OF CONTENTS

LIST OF FIGURES

Chapter 2

Chapter 3

Chapter 4

Appendices

LIST OF PLATES

ACKNOWLEDGEMENTS

I would like to thank my parents, Monic Belzile and Jean-Paul Marchildon for opening my horizons, for challenging me to do well, and for instilling in me the curiosity which has lead to my pursuing a scientific career path. Their love and moral support have been tremendous assets throughout my life, and in particular, in seeing the present endeavor to its end.

I am extremely grateful to my thesis advisor, Greg Dipple, for giving me the opportunity to tackle such diverse problems as those discussed in this thesis. He has generously provided intellectual, moral and material support during the long periods of searching for answers, and the short intervals of wonderment at the new insights we had gained. I also warmly thank the other members of my committee: Lori Kennedy, who has played an essential role in shaping my ideas about the structural evolution of the Selkirk Allochthon, and who was readily available for discussion, whenever I needed clarification about stress and strain, or just a beer-and-burger buddy; and Kelly Russell, whose extremely sharp mind has provided many an intellectual challenge, and whose hockey prowess has provided many an on-ice frustration. These people have been friends as well as advisors.

I thank my fellow graduate students and metamorphic petrology group members for discussion of ideas metamorphic or otherwise: Annette Bingemer, Chris Clarkson, Ben Edwards, Stuart Knoop, Maria Niermann, Maile Smith, Mathias Westphal.

A number of people in the department have provided technical support invaluable to this project, and for which I am grateful: Mark Baker, Bryon Cranston, Matti Raudsepp, and Mike St-Pierre. I also thank Jim Mortenson and Rich Friedman for their analytical work in dating the Bigmouth Creek stock. I extend my thanks to Claire Floriet, Tom Clemo, Sarah Vance and Barb Davey for cheerful assistance in the field.

I would like to thank Raphael Wüst and Eliane Mandli, Paulette Tercier, Mark Caplan and Isabelle Chanoine Caplan, Claire Floriet, Boyd Benson, Mike St-Pierre, Tom Clemo, Michelle Lamberson and Arne Toma, for their friendship and good company during my stay in Vancouver, and beyond. I am grateful to the generations of Rock Dogs with whom I have shared a bench for five very successful years- Let's go Hoopsters! I would also like to thank Mr. and Mrs. Pierce, my landlords at 2832 W. 3rd Ave for being so nice and accommodating and for providing the least expensive housing in all of Vancouver!

Finally, I would like to thank Bill Minarik for his love, sustained support, and encouragement throughout this endeavor, even if it meant we were three time zones apart.

Chapter 1

INTRODUCTION

The results of two separate but related petrologic studies are presented in this dissertation: 1) a study of the tectono-metamorphic evolution of a dynamic orogenic wedge, the Selkirk Allochthon of southeastern British Columbia; and 2) a study of the effect of fluid flow on the distribution of metamorphic assemblages during metamorphism of carbonate rocks. The underlying approach in both cases is to apply various petrologic methods in order to gain a better understanding of the factors which affect the evolution of metamorphic processes, and hence metamorphic terranes, through time. This approach is grounded in detailed field and laboratory characterization of metamorphic rocks. Of particular interest throughout this thesis is the spatial distribution of mineral assemblages resulting from one, or more, metamorphic events, and the history of metamorphic reactions which lead to preservation of this macroscopic spatial distribution. Such descriptive information is used to answer questions regarding the nature and temporal evolution of processes attending metamorphism, including, specifically, deformation, fluid infiltration and evolution of hydraulic properties.

The first study, which is presented in Chapters 2 and 3, is concerned with the interplay of tectonic, deformational and metamorphic processes within a dynamic orogenic wedge. The area of interest is the Selkirk Allochthon, a package of supracrustal and associated intrusive rocks deformed and metamorphosed during Mesozoic to Early Cenozoic time as a result of terrane collision at the western margin of North America. Chapter 2 presents a detailed characterization of the distribution of metamorphic assemblages in pelitic rocks of the Big Fish Creek area, which is underlain by rocks deformed and metamorphosed at intermediate depth in the orogenic wedge. Textural analysis of recrystallization sequence brings to light two distinct prograde metamorphic events (M1 and M2) separated in time by a period of cooling, infiltration and growth of retrogressive assemblages. Geochronological dating of the Bigmouth Creek stock, which intrudes rocks of the Big Fish Creek area allows the establishment of a mid-Jurassic age for M1, synchronous with emplacement of the stock. M2 resulted from Early Cretaceous reheating, recorded by titanite from the Bigmouth Creek stock. The spatial distribution of high- and low-pressure mineral assemblages developed during early and late stages of M2, respectively, requires that substantial exhumation affected these rocks in Early Cretaceous time. A detailed analysis of structural elements presented in Chapter 3 allows the reconstruction of a tectonic model for the wedge which accommodates the complex metamorphic history recorded in rocks of the Big

Fish Creek area. What permeates is a picture of a long-lived, dynamically evolving wedge controlled by the interplay of tectonic, thermo-metamorphic, and deformational processes. Far-field contraction due to collision and continued convergence led to internal deformation and thickening of the sedimentary package. This resulted in thermal relaxation, metamorphism and rheological changes in the interior of the wedge, which allowed for gravitational collapse, local extensional deformation, and decompression and cooling of the upper part of the wedge, even as overall contraction continued. Episodic fluctuations in the intensity of far-field contractional stresses and/or spatially heterogeneous internal deformation over several tens of millions of years at least, allowed for repeated heating of parts of the wedge, accounting for the polycyclic metamorphic recrystallization. Thus, the overall picture is one of "yo-yo" tectonics and metamorphism affecting a wedge active over a substantial period of time. This model may be applicable to other long-lived, highly diachronous orogenic belts such as the Appalachians and Caledonides of eastern North America and western Europe, the Hercynian belt of southern Europe, and the Himalayan chain.

The second study, presented in Chapter 4, is concerned with the interplay of fluid infiltration, fluid infiltration-driven metamorphic reactions, and the resulting changes in rock permeability during metamorphism. Metamorphic permeability can not be directly measured, as rocks now exposed were probably affected by a range of permeability-altering processes during uplift and exhumation. However, the spatial variability of mineral assemblages produced by metamorphic fluid infiltration provides a picture of the spatial distribution of "time-integrated" metamorphic permeability distribution. Furthermore, by comparing natural distributions of metamorphic assemblages to quantitative numerical models of infiltration and reaction in heterogeneously permeable rocks, the heterogeneity of flow in natural systems can be estimated. Mineral assemblage distributions obtained from numerical simulations of infiltration during contact metamorphism of siliceous dolomites were compared to the spatial distribution of mineral assemblages observed in siliceous dolomites of the Alta, Utah, contact aureole. Only simulations with highly heterogeneous permeability (considerably more heterogeneous than equivalent protolith permeability) reproduced the geometry of mineral zones observed at Alta, suggesting that permeability becomes more heterogeneous during metamorphism. This is readily explained by feedback mechanisms between infiltration, mineral reaction and the resulting permeability enhancement (due to negative changes in volume during reaction), which will tend to produce progressively more focused, and hence, more heterogeneous, flow patterns. Comparison with other contact metamorphic terranes such as the Ubehebe aureole, California, suggests that this feedback mechanism is generally important during contact metamorphism of carbonate-rich rocks. On the other hand, much smaller fluid

flow heterogeneity inferred for some regional metamorphic terranes suggests that different factors, such as compaction, may control permeability evolution during metamorphism in these environments.

Of the three main chapters which make up the bulk of this thesis, Chapter 4 has been published in a peer-reviewed journal (Marchildon and Dipple, 1998). The author contributed the larger portion of the work, including development of the two-dimensional flow and reaction algorithm and code, implementation of numerical simulations, analysis of results, drafting of figures (except Figure 4.1A which was modified from a figure supplied by the second author), and original full draft of the text of the chapter. The second author suggested the study, provided some of the computer code, most notably the mineral reaction subroutine, as well as extensive discussion of methods, results and interpretations, and abundant useful comments on numerous generations of working drafts.

Chapters 2 and 3 have not been published but are intended for eventual submission to peer-reviewed journals. But for the geochronological work, which was performed in large part by J. K. Mortensen and R.M. Friedman at the geochronology laboratory at UBC, the author is responsible for the field and laboratory results, for processing of these results into the format presented in this thesis, and for the bulk of the interpretations derived from these results and presented in this thesis.

Chapter 2

POLYCYCLIC METAMORPHIC EVOLUTION OF THE BIG FISH CREEK AREA, NORTHERN SELKIRK MOUNTAINS, SOUTHERN OMINECA BELT, BRITISH COLUMBIA

2.1 Introduction

The southern Omineca Belt of British Columbia, Canada, is a long-lived orogenic zone formed by continued accretion and contraction at the western edge of the North American plate during Mesozoic to Early Cenozoic time (e.g., Monger et al., 1982; Parrish, 1995; Fig. 2.1). Recent geochronological studies have shown the complex nature of the Mesozoic thermal evolution of the southern Omineca Belt (Sevigny et al., 1989, 1990; Scammell, 1993; Crowley et al., 1998). However, evidence for a complex metamorphic history has remained elusive. The question of the metamorphic evolution of the Omenica Belt in the Northern Selkirk and adjacent Monashee Mountains is critical because previous work suggests that apparently continuous metamorphic zones in this area (Fig. 2.2) resulted from widely diachronous metamorphic recrystallization. On the western flank of the Selkirk structural fan (Wheeler, 1965), greenschist- to upper amphibolite-grade metamorphism has been interpreted to be of mid-Jurassic age and contemporaneous with emplacement of a suite of hornblende- and biotite-bearing granitoid bodies (Van der Leeden, 1976; Brown and Tippett, 1978; Brown and Lane, 1988; Brown et al., 1992; Colpron et al., 1996). In contrast, amphibolite- to upper amphibolite-grade metamorphism on the east side of the SFA and in the adjoining Monashee Mountains (e.g., Ghent et al., 1977, 1983; Sevigny and Ghent, 1986) is interpreted to be coeval with the emplacement of peraluminous granites at approximately 100 Ma (Sevigny et al., 1989, 1990).

One interpretation of this diachroneity is that the metamorphic isograds record the displacement over time of a metamorphic "front" of regional extent, as associated deformation progressed spatially through the orogenic belt (Parrish, 1995). Alternatively, this apparent diachroneity may be due to incomplete preservation of multiple superimposed metamorphic events.

This study is based on observations from the west flank of the Selkirk Fan structure (Fig. 2.1). The area is underlain by rocks which record at least two distinct prograde regional metamorphic events. Based on geochronological evidence and on textural similarity with rocks of the Big Fish Creek area, I argue that other parts of the southern Omineca Belt also underwent a polycyclic metamorphic evolution.

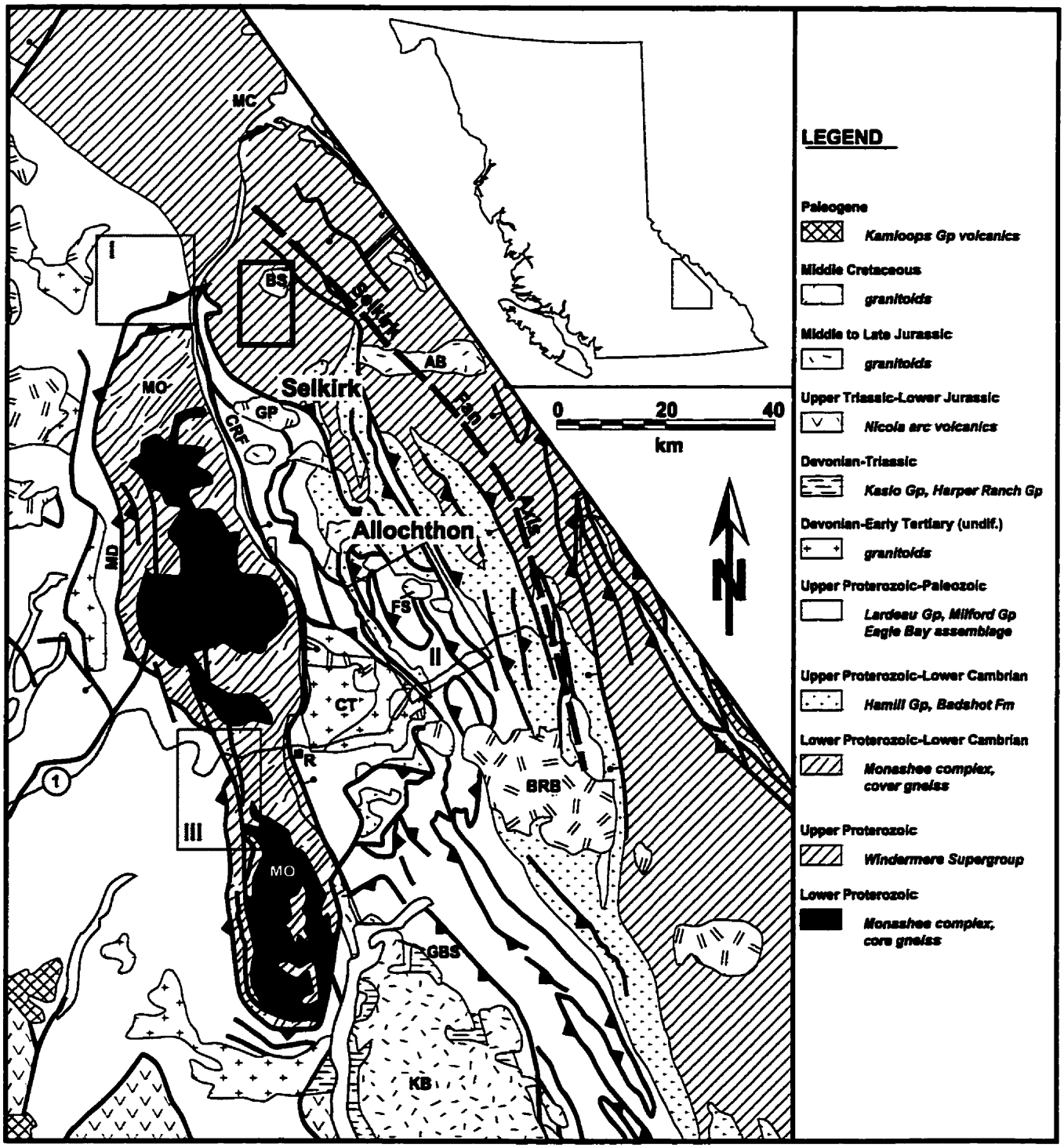

Figure 2.1 Lithotectonic map of the Southern Omineca Belt. Thick black box shows location of present study area. Gray boxes are locations of recent studies in nearby areas: I. Scammell (1993); II. Colpron et al. (1996); III. Johnston, 1996. AB: Adamant Batholith; BS: Bigmouth Creek Stock; BRB: Battle Range Batholith; CRF: Columbia River Fault; CT: Clachnacudainn Terrane; FS: Fang Stock; GBS: Galena Bay Stock; GP: Goldstream Pluton; KB: Kuskanax Batholith; MC: Mica Creek area; MD: Monashee Décollement; MO: Monashee Complex; R: town of Revelstoke. Modified after Wheeler and McFeely (1991).

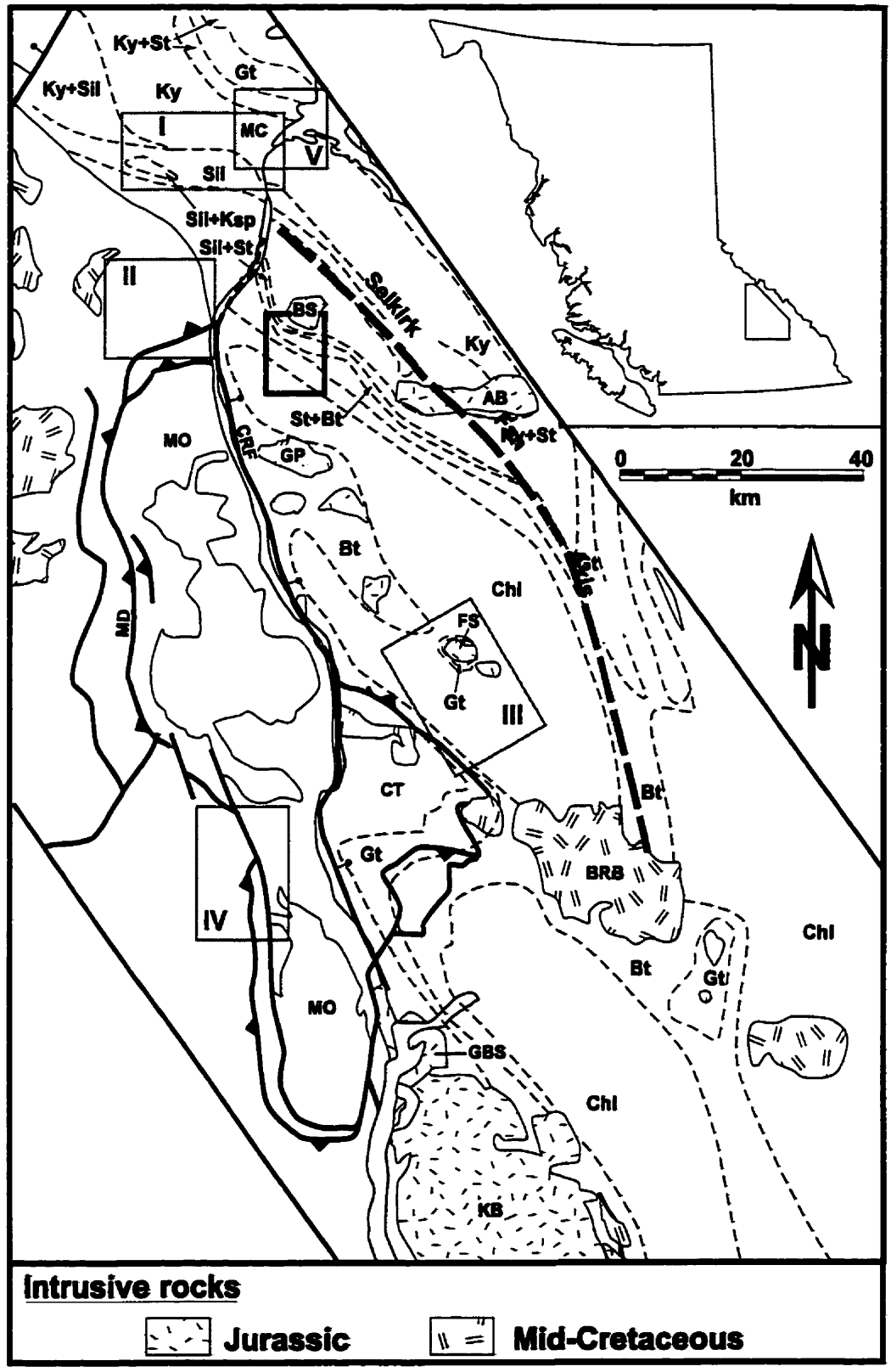

Figure 2.2 Map of metamorphic zones recorded in pelitic rocks of the southern Omineca Belt in the vicinity of Revelstoke, British Columbia. Inset shows map location. Gray boxes are locations of recent studies in nearby areas: I. Sevigny et al. (1989, 1990); II. Scammell (1993); III. Brown et al. (1992) and Colpron et al. (1996); IV. Johnston, 1996; V. Crowley et al. (1998). Mineral abbreviations are: Chl: chlorite; Bt: biotite; Gt: garnet; St: staurolite; Ky: kyanite; Sil: sillimanite; Ksp: K-feldspar. All other abbreviations are as in Figure 2.1. Modified from Read et al., 1991.

A tectono-metamorphic model is proposed for the Omineca Belt in the area of the Northern Selkirk Mountains, as a long-lived dynamic wedge which is controlled by external forces, an evolving rheological behaviour, and a complex associated thermal evolution. This model differs from previous models that require discrete pulses of deformation and a single prograde regional metamorphic event (e.g., Van der Leeden, 1976; Leatherbarrow, 1981; Raeside and Simony, 1983; Sevigny and Ghent, 1986; Brown et al., 1992a; Colpron et al., 1996).

2.2 Regional setting

The Selkirk Allochthon comprises a wedge of Late Proterozoic to Early Paleozoic continental margin sedimentary and minor volcanic rocks within the Omineca Belt. This wedge migrated eastward during crustal accretion and contraction in Mesozoic time (Monger et al., 1982; Brown et al., 1986; 1993). Eastward migration of the Allochthon is generally interpreted to have taken place primarily along a discrete crustal-scale, basement-rooted décollement surface, the Monashee Décollement (Read and Brown, 1981; Journeay, 1986; Brown et al., 1986; Brown and Journeay, 1987). Recently, however, Scammell (1993) and Johnston (1996; also see Williams and Jiang, 1999) proposed, on the basis of structural analysis of the Selkirk Allochthon in the Monashee Mountains west and south of the Big Fish Creek area (Fig. 2.2), that strain associated with eastward displacement of the Allochthon was distributed over mid-crustal high-strain zones of finite thickness.

The Selkirk Fan structure (Wheeler, 1965) is part of the Allochthon. It consists of a wedge of rocks showing southwest structural vergence on the west side, and northeast structural vergence on the east side, defining a structural axis along the spine of the Selkirk and Northern Monashee Mountains. A metamorphic culmination is roughly coincident with this structural axis (Fig. 2.2). The Big Fish Creek area is located within the western flank of the Selkirk Fan structure.

2.3 Previous work

Wheeler (1965) mapped several metamorphic zones which define the regional metamorphic culmination in the Northern Selkirk Mountains (Fig. 2.2). In the study area, Van der Leeden (1976) mapped metamorphic zones in pelitic rocks, including a chlorite-zone, a biotite zone, a garnet zone, a staurolite zone, and a kyanite zone, from south to north (Fig. 2.3). Leatherbarrow (1981) integrated information from different workers and using geothermobarometry, suggested that rocks on the southwest flank of the Selkirk Fan structure were metamorphosed at lower peak pressure (5 Kb) than rocks on the

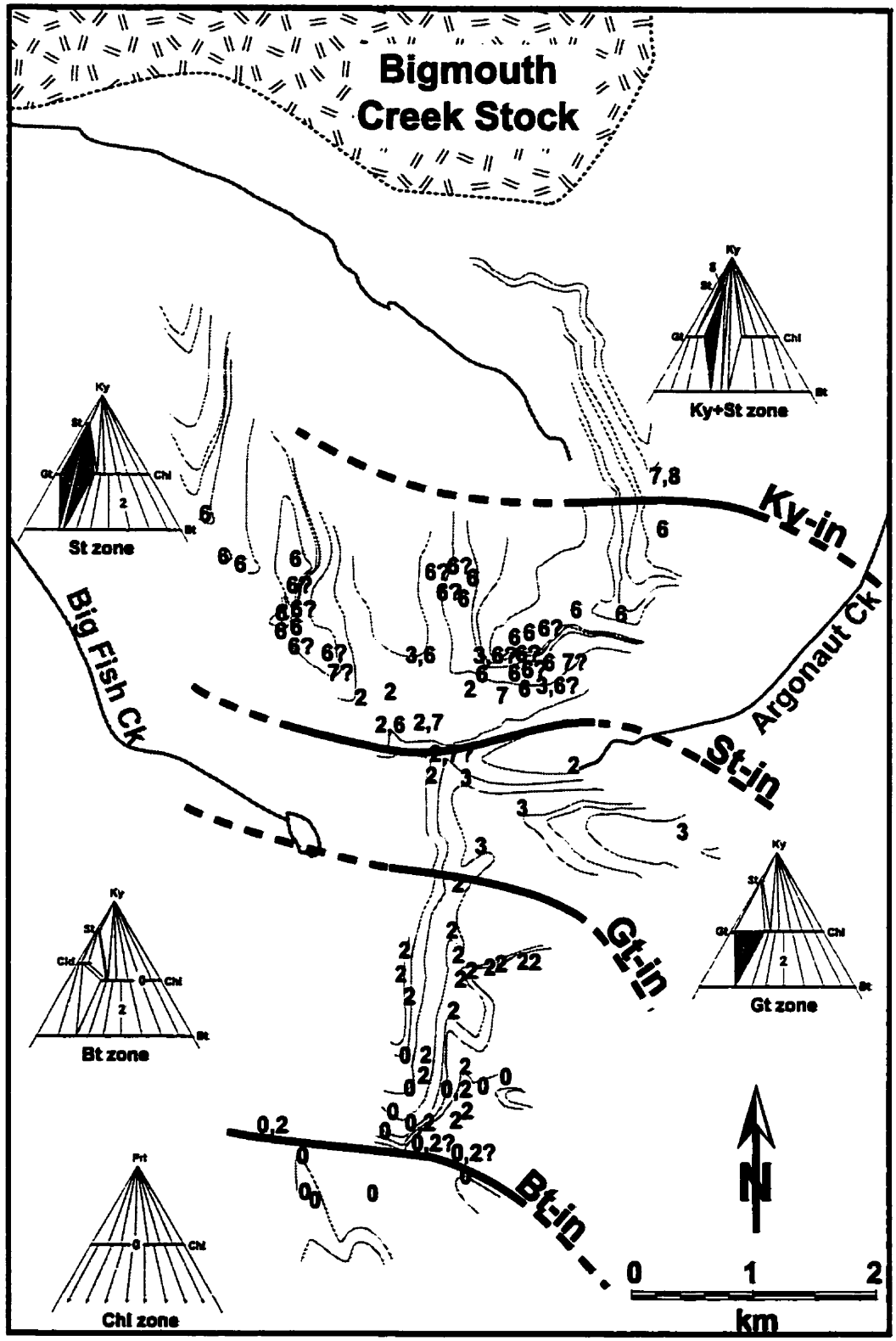

Figure 2.3 Distribution of mineral isograds and metamorphic assemblages recorded in pelitic rocks of the study area. Numbers correspond to AFM assemblages as shown in AFM diagrams for the different zones. Question marks following numbers indicate that one of the phases in the reported assemblage was completely retrogressed and that it was identified on the basis of the pseudomorphic shape of the retrograde replacement mineral(s). Divariant assemblages observed in these rocks are shaded on the appropriate AFM diagrams. Mineral abbreviations are: Cld: chloritoid; Prl: pyrophyllite. All others are as in Figure 2.2.

northeast flank (7 Kb). From this, he inferred post-metamorphic vertical displacement of 7 km on the poorly-constrained Argonaut Mountain normal fault, which he interpreted to trend NW-SE, between the Bigmouth Creek stock and the Adamant batholith (Fig. 2.1). The requirement for such a structural discontinuity to some extent hinges on the assumption that metamorphism is more or less contemporaneous throughout the metamorphic culmination. Perkins (1983) found that minerals developed as a result of prograde regional metamorphism across the metamorphic culmination showed similar relative timing relationships to deformation.

Ghent et al. (1977, 1983) and Simony et al. (1980) constrained the sequence of metamorphic isograds in the northernmost Selkirk Mountains and Monashee Mountains north of the Columbia River, on the northeast flank on the metamorphic culmination. They mapped isograds corresponding to (1) the first appearances of kyanite, which coincides with the first appearance of staurolite, (2) the disappearance of staurolite which coincides with the first appearance of leucosome, (3) the appearance of sillimanite, and (4) the co-existence of garnet and clinopyroxene. Ghent et al. (1979, 1982, 1983) constrained peak metamorphic pressures to be in the 6-8 kbar range, for rocks of the staurolite + kyanite, to the sillimanite zones.

Archibald et al. (1983) interpreted metamorphism in the southern part of the Selkirk Allochthon as synchronous with emplacement of mid-Jurassic intrusions (ca. 165-170 Ma). Van der Leeden (1976) argued that metamorphism in the present and adjacent areas must pre-date, or be synchronous with emplacement of the Bigmouth Creek stock (Figs. 2.2, 2.3), which he inferred to be of mid-Jurassic age based on similarity with known mid-Jurassic intrusive rocks in the area. Brown et al. (1992a) and Colpron et al. (1996) interpreted greenschist facies regional metamorphism and associated deformation in the vicinity of the Fang stock (Fig. 2.2) on the southwest flank of the Selkirk Fan, to have terminated by ca. 168 Ma.

Sevigny et al. (1989, 1990; Fig. 2.2) interpreted regional metamorphism in the Monashee Mountains to coincide in time with emplacement of syn-kinematic granitic bodies which yielded Cretaceous U-Pb crystallization ages (ca. 100 Ma). Crowley et al. (1998; Fig. 2.2) found evidence for mid- to Late Jurassic regional thermal events in the U-Pb systematics of metamorphic monazite from the Northern Selkirk and Monashee Mountains north of the study area. Based on partial resetting of some monazite grains, and on evidence for renewed growth of monazite at ca. 70 Ma, these authors also postulated that a Late Cretaceous thermal event affected rocks in this area. In addition, they provided evidence for ductile deformation as late as Early Tertiary (ca. 61 Ma). Scammell (1993) documented

protracted metamorphism extending over at least 40 m.y. from ca. 140 Ma to ca. 97 Ma in the Monashee Mountains west of the Columbia River (Fig. 2.2).

2.4 Methodology

The work presented in this and the following chapter was based on field mapping of lithological units and metamorphic assemblages during the course of thirteen weeks over three Summers (1994 to 1996). Field work also involved description and measurement of attitudes of the various structural elements observed in the Big Fish Creek area (see Appendix IV), and collection of over 250 samples in as random a fashion as allowed by outcrop abundance and quality. (Typically, several hand samples were collected from a given outcrop, from different structural levels, in order to obtain as representative as sample as possible.) Further analytical work involved petrographic analysis with a polarizing optical microscope and a Philips XL-30 scanning electron microscope, and microstructural description of over 200 thin sections cut from over 180 samples (see Appendix II for list of samples and outcrop locations), collection of compositional maps of garnet porphyroblasts and compositional point analyses of various minerals with a Cameca SX-50 electron probe microanalyzer (operating conditions: 15 KeV accelerating voltage, 5-20 nA beam current, 1-5 μm spot size, using natural standards for recalculation of raw count data; see Appendix III for results). One sample of intrusive rock (Bigmouth Creek granodiorite) was collected and dated at the Geochronology Laboratory at UBC in an attempt to constrain the timing of pluton emplacement, and its implication for the timing of metamorphism and deformation. Interpretations presented as part of this study are drawn from observations and analysis representative of an important proportion of relevant samples.

2.5 Local geology

A lithostratigraphic framework for rocks of the study area is presented in Section 3.2.2 of the following chapter. A very brief summary follows here.

The rocks are subdivided into four broadly defined packages separated by gradational contacts (Fig. 2.4), from low to high structural level: 1) a psammitic to semi-pelitic package whose base was not mapped in this study; 2) a pelitic package, approximately 100-200 m in thickness, comprising increasingly abundant, rusty weathering calc-pelitic schist and brown-weathering impure marbles towards the top of the interval, and which grades into, 3) a calc-pelitic package characterized by sporadic intervals of impure marble, and more rarely, of massive chlorite schist or amphibolite (Fig. 2.4); and 4) a sequence

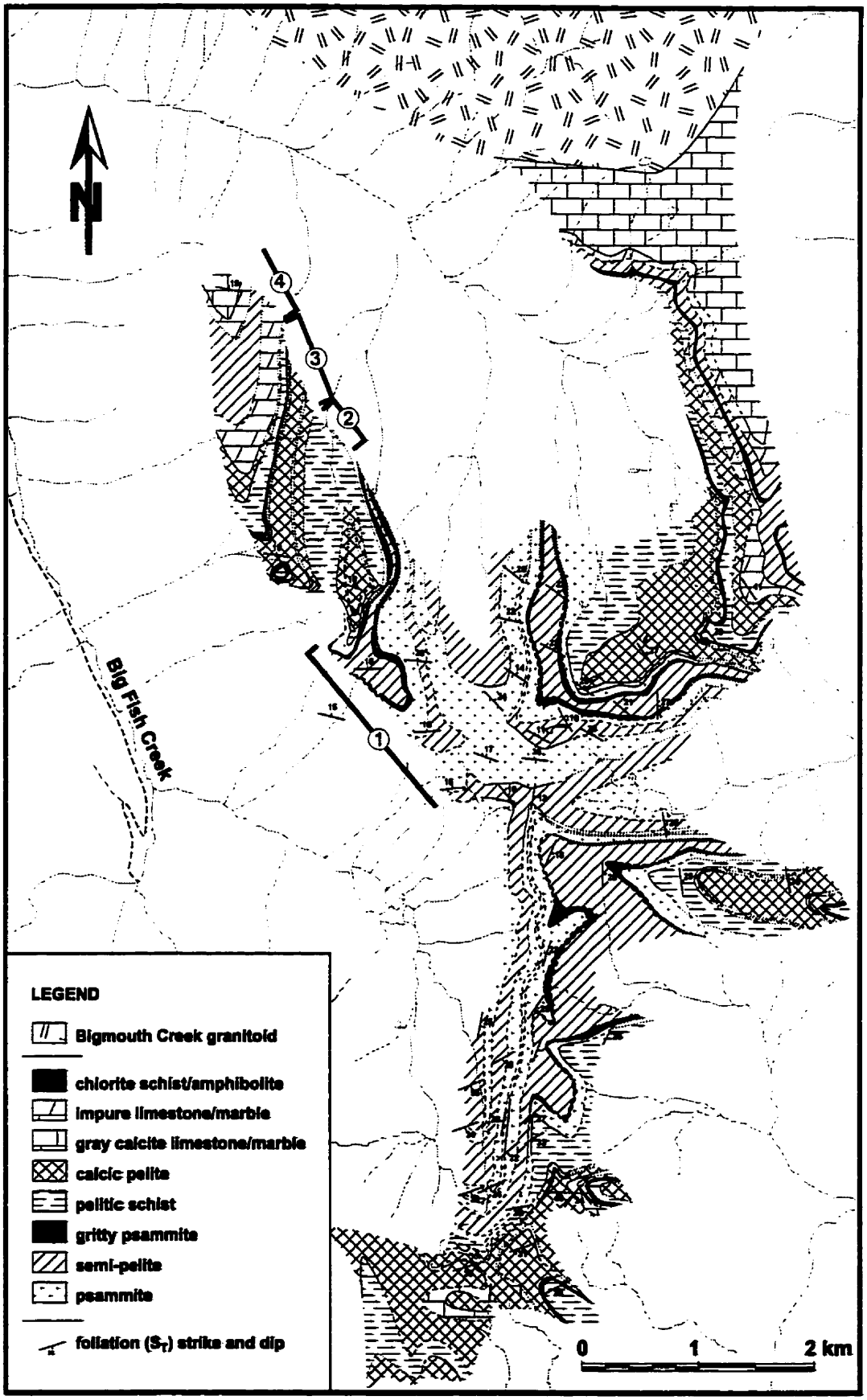

Figure 2.4 Lithologic map of the study area. Stratigraphic intervals described in text are indicated by thick brackets.

of brown-weathering, impure to relatively pure calcite, and/or dolomite marbles, associated with thickly layered quartzitic psammite, local amphibolite and thin intervals of talc-schist, which was observed only in the northern part of the study area.

The Bigmouth Creek pluton (Wheeler, 1965) is exposed at the northern limit of the study area. It consists of K-feldspar porphyritic, hornblende + biotite granodiorite. Epidote is present in the Bigmouth Creek pluton and it occurs as subhedral, pale yellowish brown crystals in close spatial association with hornblende. It is unresorbed and interpreted to be magmatic, with habit consistent with growth late in the crystallization history of the pluton. The presence of magmatic epidote is widespread in hornblende-bearing granitoids in the southern Omineca Belt (e.g., Rice, 1941; Reesor, 1973; Ghent et al., 1991; Colpron et al., 1996).

The principal structural element in the study area is a shallow to moderately-dipping foliation characterized by the alignment of minerals with shape-preferred orientation, and generally sub-parallel to compositional layering. As discussed in the following chapter, this is a transposition foliation (referred to as S_T) developed over a substantial time interval and associated with intense strain. S_T strikes northwest to northeast, defining a large-scale, open non-cylindrical fold. A late east-west-striking, steep crenulation foliation is commonly observed, especially in the southern half of the area. The reader is referred to Chapter 3 for an in depth treatment of the structural geology of the area.

2.6 Metamorphic events and metamorphic parageneses in pelitic rocks

The Northern Selkirk Mountains and the adjoining Monashee Mountains are underlain by regionally metamorphosed rocks recording greenschist to upper amphibolite facies conditions. Figure 2.2 shows the distribution of mineral zones in pelitic rocks. The southern part of the area is dominated by greenschist facies rocks (chlorite, biotite, and locally garnet zones for pelites). These give way northward to amphibolite facies rocks (garnet zone to sillimanite + K-feldspar zone in pelitic rocks; Fig. 2.2). The metamorphic culmination is defined by a north-northwest trending sillimanite + K-feldspar zone flanked to the northeast and southwest by progressively lower-grade rocks. The axis of the metamorphic culmination coincides approximately with the axis of the Selkirk Fan (Fig. 2.2). The Big Fish Creek area is located on the southwest flank of this culmination (Fig. 2.2). It exposes a metamorphic field gradient defined by a sequence of metamorphic zones characterized by the presence of chlorite in the south, to the coexistence of kyanite and staurolite in the north (Fig. 2.3).

Two distinct prograde regional metamorphic events are recorded in this area. Evidence for the early metamorphic event, M1, is cryptic and consists primarily of inclusion-rich, anhedral garnet cores in rocks affected by subsequent M2 recrystallization (Plates 1A,B, 2). The latter event, M2, is better preserved, and M2 mineral assemblages and isograds define the local field gradient (Fig. 2.3). Late growth of coarse-grained andalusite is interpreted to record late-M2 decompression. These different metamorphic recrystallization events are described in detail in the following sections.

2.6.1 M1 metamorphism

Early anhedral cores of garnet in composite M1+M2 garnet porphyroblasts are ubiquitous in the M2 garnet and staurolite zones in the Big Fish Creek area (Plates 1A,B, 2). These cores are usually inclusion-rich, and overgrown by inclusion-poor, euhedral rims. Garnet porphyroblasts typically preserve curved or inclined inclusion trails ($S_i \neq S_e$, where S_i and S_e are the foliations internal and external to the porphyroblasts, respectively; Plate 1A,B,C), which locally show a structural style distinct from that of the matrix. These early garnet grains are commonly broken into two or more fragments, and an M2 overgrowth is developed more or less concentrically around the individual clasts (Plates 1B, 2). A sharp compositional break is invariably associated with the textural break (Plate 2; Fig. 2.5).

A few occurrences of anhedral, inclusion-rich garnets devoid of euhedral overgrowth were found, primarily in the garnet zone. Typically, these are surrounded by a chlorite-rich (± biotite) rind which commonly pseudomorphs the original garnet grain (e.g., Plate 1C). These are interpreted as early, M1 garnets based on their textural similarity with cores of composite garnets. The chlorite-rich rind is interpreted to be the product of retrogression involving M1 garnet resorption.

M2 garnet and/or staurolite are commonly developed around M1 garnet cores (see Sections 2.6.2.3 and 2.6.2.4; Plates 1A,B, 2). Often, M2 garnet and/or staurolite overgrow the chlorite-rich rind (Plates 1B, 2), implying that formation of the retrograde rind around M1 garnet preceded the crystallization of M2 peak metamorphic minerals (garnet and/or staurolite). Retrogression of M1 garnet prior to M2 garnet growth is also supported by the anhedral, resorbed aspect of M1 cores (e.g., Plates 1A,B, 2).

From these observations and because no reaction sequence resulting from a single prograde evolution can explain the two texturally and chemically distinct garnet generations and the intervening production of chlorite ± biotite-rich aggregates after garnet (e.g., Spear and Cheney, 1989), growth of

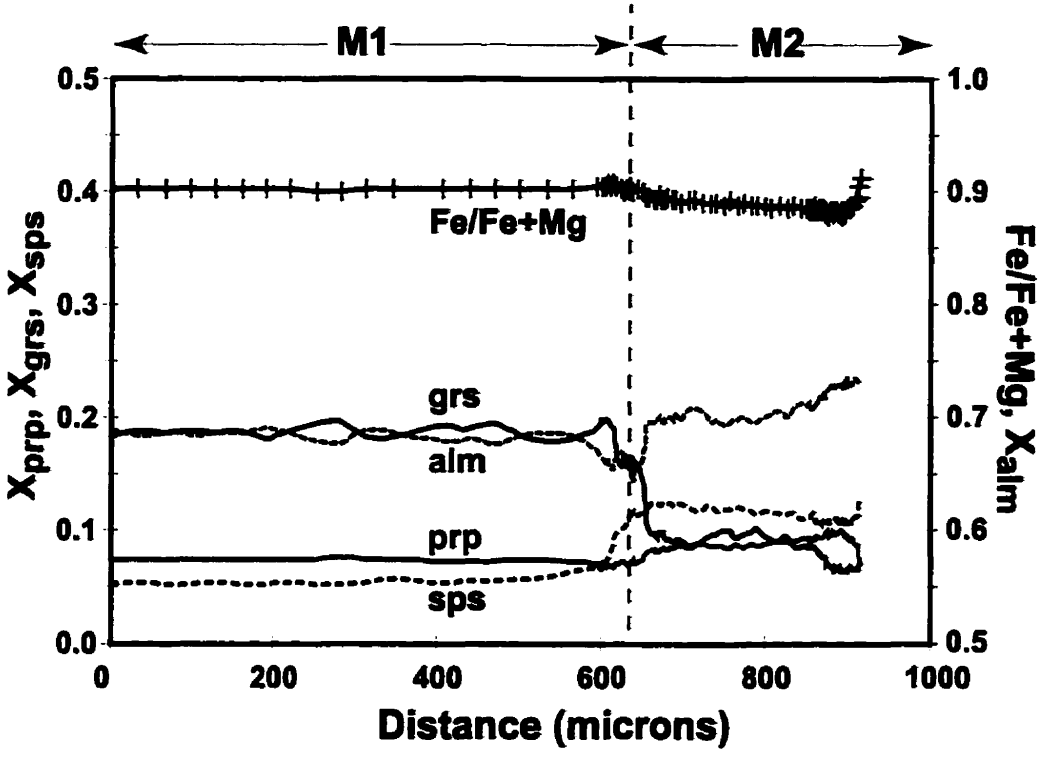

Figure 2.5 Core (left) to rim (right) compositional zoning profile of composite garnet porphyroblast, sample 94-NM-111B, M2 staurolite zone (this is from the left-hand-side porphyroblast of Plate 2.1B; also see Plate 2.2A). Boundary between M1 and M2 garnet (dashed vertical line) is inferred based on observed sharp decrease in the grossular, and increases in the almandine, pyrope, and spessartine components of the garnet. X_{prp}, X_{grs}, X_{sps}, X_{alm} are mole fractions of the pyrope, grossular, spessartine and almandine garnet components, respectively. Note the different scales for X_{prp}, X_{grs} and X_{sps}, and for X_{alm} and Fe/(Fe+Mg).

anhedral garnet cores and euhedral overgrowths must have been separated by an episode of retrograde growth of hydrous minerals, which required cooling and infiltration of hydrous fluid. In other words, early and late garnet growth are evidence for two distinct metamorphic or thermal pulses (M1 and M2) and an intervening episode of cooling and retrograde recrystallization.

2.6.2 M2 metamorphism

The following M2 mineral zones are encountered in the area, from south to north (Fig. 2.3): chlorite, biotite, garnet, staurolite, and kyanite + staurolite. Mineral parageneses and reaction textures in pelitic and associated rocks of these different metamorphic zones are described in detail in the following sections.

It is likely that observed matrix minerals such as muscovite, chlorite, and biotite crystallized during M1 metamorphism. However, as discussed in detail in Chapter 3, both M1 and M2 took place during protracted, progressive deformation which resulted in sustained transposition of structural elements in these rocks. Differentiating between M1 and M2 matrix minerals based on their spatial relationship to structural elements is therefore impossible. For this reason, the biotite-in isograd in Figure 2.3 may be partly diachronous (resulting from both M1 and M2). Higher-grade metamorphic isograds (garnet-in, staurolite-in, and kyanite-in), however, are based on unequivocal identification of 1) late-M2 garnet overgrowth on M1 garnet cores; or 2) other minerals (staurolite, kyanite) associated with the development of M2 garnet overgrowths.

The map in Figure 2.3 shows the distribution of M2 mineral assemblages and metamorphic zones. It is based on the observed distribution of metamorphic parageneses in rocks of pelitic composition, and shows isogradic traces generally at high angle to lithologic contacts. The different mineral zones are also positioned in the appropriate AFM projections (Fig. 2.3; Thompson, 1957).

The three-dimensional attitudes of M2 isograds are unconstrained. Leatherbarrow (1981) argued for steeply-dipping (> 60°) isograds on the basis of the presence of steeply-dipping isograds in the Mica Creek area (Ghent et al., 1977; 1980). No clear evidence for a steeply-dipping attitude of isograds in the Big Fish Creek area was observed in the present study.

2.6.2.1 Chlorite zone

The chlorite zone is located at the southern end of the study area (Fig. 2.3). The southern limit of this zone, the first occurrence of chlorite in pelitic rocks, was not encountered. The northern, and higher-grade limit of the chlorite zone is defined as the surface of first occurrence of biotite (the biotite-in isograd, Fig. 2.3). The minimum outcropping width of this zone is approximately 1 km.

Pelites in the chlorite zone are characterized by variable fresh coloration, which reflects variations in the contents of chlorite, muscovite, opaques, and locally, graphite. Grain size is generally fine to medium (≤ 1 mm), and increases irregularly towards the biotite isograd. In addition to a dominant penetrative foliation, S_T, defined by the alignment of minerals with grain-shaped preferred orientation and by compositional layering, there is a steep crenulation cleavage developed in many chlorite-grade rocks. An associated crenulation lineation (resulting from intersection of S_T with this cleavage) is almost ubiquitous (see Chapter 3, Section 3.3.2.7).

Chlorite-zone pelites typically comprise the assemblage muscovite + chlorite + quartz + opaques + K-feldspar ± albite ± ankerite ± calcite ± epidote (pistacite) + tourmaline + apatite ± allanite ± zircon. They generally show mm-scale compositional laminae characterized by variable amounts of quartz and phyllosilicates ± carbonates ± opaques. Muscovite and chlorite flakes lie parallel to this layering. This defines S_T. Locally, relicts of an earlier foliation, defined by the preferred orientation of fine, recrystallized muscovite flakes is preserved, which shows different degrees of transposition into S_T. Late folding resulted in a gentle undulation to a strong spaced crenulation cleavage overprinting S_T (Plate 3A,B). Where a crenulation cleavage is well-developed, muscovite and chlorite flakes are locally aligned along this cleavage (Plate 3B).

S_T-parallel chlorite grain-size generally increases towards the biotite isograd (from 0.2 to 0.5 mm). Large (1-2 mm) chlorite ± muscovite porphyroblasts and/or aggregates which locally show inclusion trails (S_i) mimicking crenulated S_T (S_e), are present which are locally deformed by, or around which are wrapped, the crenulation cleavage planes (Plate 3B). Such chlorite + muscovite aggregates have been widely reported in low-grade metamorphic rocks and may represent prograde chlorite growth on detrital white mica clasts (e.g., van der Pluijm and Kaars-Sijpesteijn, 1984; also see Craig et al., 1982 for a review of occurrences and possible modes of origin), or may be retrograde after earlier metamorphic minerals (see Sections 2.6.2.2 and 2.6.2.3 below).

2.6.2.2 Biotite zone

Immediately north of the chlorite zone is the biotite zone (Fig. 2.3). Its low-grade boundary corresponds to the surface of first appearance of biotite in pelitic rocks. The biotite zone is approximately two kilometers in width, and is bounded at its northern, high-grade limit by the first occurrence of M2 garnet in pelitic rocks.

Pelitic schists in the biotite zone are generally coarser-grained and paler in color than their equivalent in the chlorite zone. There is an irregular increase in grain size towards the garnet isograd. Coarser-grained rocks, especially in the upper part of the biotite zone, have a sheen due to the abundance of coarse muscovite flakes. As in the chlorite zone, a strong penetrative foliation, S_T, is ubiquitous, and a steep crenulation cleavage is also locally developed, although not as extensively as in the chlorite zone. An associated intersection lineation is still relatively widespread.

Typically, pelites of the biotite zone are characterized by the assemblage biotite + muscovite + chlorite + quartz + opaques ± plagioclase ± epidote + tourmaline + apatite ± allanite ± zircon.

The first appearance of biotite is as basal cleavage-controlled intergrowth or overgrowth on medium-grained chlorite flakes in mm-scale chlorite ± muscovite aggregates, or as discrete, small, randomly oriented, equant flakes in these aggregates. Up-grade from the first appearance of biotite, biotite flakes in chlorite + biotite clots are still the dominant mode of occurrence of biotite (Plate 3C); this biotite becomes coarser and the clots become progressively more biotite-rich, at the expense of chlorite. Fine (100-200 um) isolated biotite flakes parallel to S_T are rare at the low-grade end of the biotite zone, but become pervasive as the garnet isograd is approached. Biotite flakes showing random to S_T-parallel orientation become coarser and more abundant up-grade from the first appearance of biotite. Of particular interest are coarse biotite porphyroblasts which, from the upper part of the biotite zone onward, are widely developed (Plate 3D). The relationship of these porphyroblasts to matrix structures is not simple, but as discussed in detail in Chapter 3, provides important constraints on the nature of deformation in these rocks.

Muscovite and chlorite in biotite-grade rocks generally show textures similar to those observed in chlorite-grade rocks. In general, no carbonate is present in biotite-bearing pelites of this zone. Medium-grained epidote porphyroblasts which overgrow S_T as well as the later crenulation cleavage are locally abundant.

The typical pelitic paragenesis in biotite-zone rocks is biotite + chlorite + muscovite + quartz. Chloritoid was not identified. The close spatial relationship between biotite and chlorite flakes or aggregates in the lower half of the biotite zone suggests that a probable biotite-producing reaction was (e.g., Wang and Spear, 1991; Spear, 1993):

$$\text{chlorite} + \text{K-feldspar} \rightarrow \text{biotite} + \text{muscovite} + \text{quartz} + H_2O \qquad (2.1)$$

A limited amount of carbonate-bearing rocks occurs in the chlorite zone suggesting that subordinate reactions involving the consumption of a carbonate phase, such as:

$$\text{quartz} + \text{muscovite} + \text{siderite} + H_2O \rightarrow \text{biotite} + \text{chlorite} + CO_2 \qquad (2.2A)$$

or,

$$\text{quartz} + \text{muscovite} + \text{chlorite} + \text{ankerite} \rightarrow \text{biotite} + \text{plagioclase} + CO_2 + H_2O \qquad (2.2B)$$

(e.g., Ferry, 1984; Symmes and Ferry, 1991) may also have lead to biotite production in the biotite zone.

The biotite "isograd" is defined as the first appearance of biotite in pelitic rocks. Chlorite-grade (i.e., biotite-free) pelitic assemblages occur sporadically up-grade of the biotite isograd (Fig. 2.3). This may due to: 1) biotite stability attained at different conditions depending on the nature of the biotite-in reaction (reactions 2.1 or 2.2; e.g., Ferry, 1984); 2) the continuous nature of reactions 2.1 and 2.2, which will proceed at lower temperature in Fe-rich rocks than in Mg-rich rocks; 3) the effect of spatially variable H_2O and CO_2 activities on reactions 2.1 and 2.2 (e.g., Ferry, 1984; Symmes and Ferry, 1991); or 4) kinetic factors. As described above, incipient development of biotite in the low grade portion of the biotite zone is usually as basal cleavage-controlled intergrowth or overgrowth on chlorite flakes, suggesting that early biotite growth is controlled in part by the ability to nucleate on pre-existing chlorite flakes, and that material transfer to biotite growth sites may be a limiting factor.

In summary, the isogradic surface for first appearance of biotite is not a true reaction isograd but rather, is probably defined by a series of reactions governed primarily by bulk composition.

The close spatial association of biotite and chlorite in the lower part of the biotite zone could also result from retrogression of biotite (e.g., Veblen and Ferry, 1983), and some chlorite in the biotite zone

can be shown to be retrograde after biotite and/or garnet (see section 2.6.2.3 below). The irregular nature of the biotite-in isograd could therefore in part represent the effects of heterogeneous retrogression.

2.6.2.3 Garnet zone

The M2 garnet zone is located immediately north of the biotite zone (Fig. 2.3). The spatial extent of this zone is poorly constrained but appears to be relatively restricted (~1 km in width; Fig. 2.2). The low-grade boundary of this zone is defined by the appearance of M2 garnet overgrowth on M1 garnet cores. The upper limit of the M2 garnet zone is defined by the surface of first appearance of staurolite in pelitic rocks (Fig. 2.3).

There is a gradual increase in the grain size of matrix phyllosilicates from the chlorite zone onward. From the upper part of the biotite zone through to the kyanite + staurolite zone, matrix micas are generally relatively coarse-grained, giving pelitic schists a relatively pale color and a bright sheen (e.g., Plate 4A,B). As in the chlorite and biotite zones, a strong penetrative foliation, S_T, is everywhere observed. A steep crenulation cleavage is rarely observed, and a crenulation lineation is less extensively developed than in lower grade rocks.

Pelitic rocks in the garnet zone are characterized by the assemblage garnet + biotite + chlorite + muscovite + quartz + plagioclase ± epidote + opaques ± ilmenite + zircon + allanite + tourmaline.

Much of the biotite in the garnet zone is texturally similar to biotite found in the upper part of the biotite zone. In addition, biotite is also commonly found as a replacement product after garnet, with or without chlorite (Plate 1).

Chlorite is ubiquitous in garnet zone rocks and occurs as S_T-parallel to randomly-oriented flakes. Late, randomly- or concentrically-oriented chlorite is found in replacement rims around garnet (with or without biotite; Plate 1C).

Anhedral, inclusion-rich garnet porphyroblasts interpreted to be of M1 origin are common in rocks between the garnet isograd and the first appearance of staurolite (Fig. 2.3). These are generally partially to completely pseudomorphed by retrograde chlorite ± biotite (Plate 1C,D). The development of M2 garnet (euhedral, inclusion-poor) is generally limited to thin overgrowths on these early porphyroblasts. Occurrences of these overgrowths define the M2 garnet zone (Fig. 2.2).

No chloritoid was found in the study area. On the other hand, biotite and chlorite are abundant in pelitic rocks of the biotite and garnet zones. Therefore, the M2 garnet producing reaction in the garnet zone was probably:

$$\text{chlorite} + \text{biotite} + \text{quartz} + \text{muscovite} \pm \text{plagioclase} \rightarrow \text{muscovite} + \text{garnet} + H_2O \qquad (2.3)$$

(e.g., Spear and Cheney, 1989).

Several points are worth noting concerning garnet occurrences in the M2 garnet zone: 1) M2 garnet growth is restricted to overgrowths on M1 porphyroblasts; 2) the spatial range of M1 garnet porphyroblasts more or less coincides with that of M2 garnet (although some chlorite + biotite pseudomorphs in the M2 biotite and chlorite zones may be after early garnet); and 3) the width of the M2 garnet zone is quite restricted (~ 1 km).

The limited extent of the M2 garnet zone, and the restricted occurrences of M2 garnet in the garnet zone may in part be due to the paucity of appropriate lithological types in the area corresponding to the garnet zone. Outcrops in this area predominantly expose quartzo-feldspathic, psammitic to semi-pelitic rocks, and where pelites do occur, it is usually as thin, dip-slope intervals. M2 garnet overgrowths were found in relatively thin pelitic layers in otherwise dominantly quartzo-feldspathic intervals in four outcrops (Fig. 2.3). Constraining the position of the garnet-in isograd along the main north-south trending ridge in Figure 2.3 is hampered by the fact that psammitic rocks crop out over several hundred meters across strike of the isograd (Fig. 2.4). Hence the coincidence of M1 and M2 garnet occurrences may be due to bulk compositional controls restricting the development of garnet rather than actual spatial coincidence of P-T conditions for development of garnet during M1 and M2 metamorphic recrystallization.

Another possible cause for some of the foregoing observations is the restricted stability of garnet + chlorite in bulk compositions typical of pelites in the study area. M1 and M2 garnets tend to be relatively Mn-poor (Fig. 2.5). Spear and Cheney (1989) noted that the temperature range within which garnet + chlorite are stable is related to the Mn content of garnet (or the bulk rock). The more Mn-poor the garnet, the more limited is the stability of the garnet + chlorite paragenesis.

Yet another explanation is that the surface corresponding to the first appearance of M2 garnet in these rocks, the M2 "garnet isograd", may in fact be a surface defining the limit of total retrograde resorption of garnet subsequent to peak M2 metamorphism. A number of instances of completely retrogressed garnet (i.e., chlorite ● biotite pseudomorphs after garnet) were encountered in the garnet zone of Figure 2.3 (e.g., Plate 1D). In addition, chlorite ± biotite clots are commonly encountered in rocks of the biotite and chlorite zones (Plate 3C). Phyllosilicates in these clots are S_T-parallel to randomly-oriented, suggesting that the timing of formation of these clots relative to matrix structures is variable. Some of these clots may be of diagenetic origin (e.g., Craig et al., 1982). However, those which appear to be late with respect to deformation, and occur in the high-grade part of the biotite zone, may have originated by retrograde replacement of M2 and/or M1 garnet porphyroblasts. The locally extensive retrogression of M2 mineral assemblages in higher-grade rocks (see below) is consistent with this interpretation.

Alternatively, the restricted spatial extent of the M_2 garnet zone and the coincidence of M1 and M2 garnet occurrences may be due to a kinetic control on the development of M2 garnet. Occurrences of M2 garnet in the M2 garnet zone are exclusively as overgrowths on M1 cores. Even in the staurolite zone (and possibly also in the kyanite + staurolite zone), M2 garnet occurs predominantly as overgrowths on early M1 cores, suggesting that nucleation may be a limiting factor in the development, and hence spatial distribution of M2 garnet. This, in turn, may reflect the short-lived nature of M2 metamorphism.

The question of the spatial coincidence of M1 and M2 garnet remains without an unequivocal answer at this time. It may consist of a combination of the possible causes discussed above, but insufficient information is presently available to evaluate their relative importance.

2.6.2.4 Staurolite zone

The M2 staurolite zone is a little over two kilometers wide in map view (Fig. 2.3). Its lower-grade limit is the first appearance of staurolite (which everywhere coexists with biotite). Its higher-grade limit is constrained by the appearance of kyanite in staurolite-bearing rocks. In the western part of the area shown in Figure 2.3, rocks of staurolite grade are the highest-grade pelitic rocks encountered. This is probably due to the lack of exposure in general and in particular, to the paucity of outcrops of pelitic rocks in that area. However, rocks characterized by staurolite + biotite parageneses were found, in reconnaissance mapping, to crop out west of Big Fish Creek, to the northwest of the area shown in Figure

2.2 (see Fig. 2.6). Northward, these give way to staurolite + sillimanite parageneses. The significance of this will be addressed in Section 2.6.2.5.

Staurolite-grade pelites are generally coarser-grained than lower-grade rocks, and show more discrete compositional layering at the millimeter scale, i.e., thin (1-2 mm, typically) mica-rich laminae separating thicker (~3-10 mm), more quartzo-feldspathic layers. This layering coincides broadly with the foliation defined by the preferred orientation of anisotropic minerals, S_T, although, as demonstrated in Chapter 3, the nature of this foliation is very complex in detail.

A crenulation lineation on S_T is observed which is more or less parallel to intersection lineations in lower-grade rocks, suggesting the development of a steep crenulation cleavage.

Pelitic rocks in the staurolite zone typically include the assemblage staurolite + garnet + biotite + muscovite + chlorite + quartz + opaques + plagioclase ± zoisite ± allanite ● tourmaline ● zircon ● apatite ± monazite ± xenotime.

Through most of the staurolite zone, garnet typically occurs as composite porphyroblasts consisting of inclusion-rich, anhedral M1 cores, and inclusion-poor, euhedral M2 rims (Plates 1B, 2, 5A). The porphyroblasts commonly consist of fragments of split M1 cores overgrown on all sides by M2 garnet. Euhedral, inclusion-poor grains devoid of obvious M1 cores also occur throughout the staurolite zone. In the low-grade half of the staurolite zone, these are usually small (< 0.5 mm) and almost exclusively spatially associated with much larger composite garnet porphyroblasts (Plate 5A). Locally, they are included in staurolite (Plate 5A). In the higher-grade portion of this zone, subhedral, inclusion-poor garnet porphyroblasts are also observed which are not spatially associated with composite garnets. These are also interpreted to be of M2 generation. Where staurolite has developed adjacent to M2 garnet, the garnet is embayed, suggesting that garnet consumption is involved in staurolite production (Plates 1B, 5A). In the higher-grade part of the staurolite zone, garnet porphyroblasts are locally very deeply embayed, commonly forming atolls. These porphyroblasts are spatially associated with staurolite, and embayments are typically filled in large part by biotite (e.g., Plate 5C).

Biotite occurs in the staurolite zone as medium- to coarse-grained, S_T-parallel to randomly-oriented flakes. The causes and implications of this distribution will be addressed in detail in Chapter 3. In addition, biotite flakes are developed around garnet in close association with staurolite (Plates 1B, 5A).

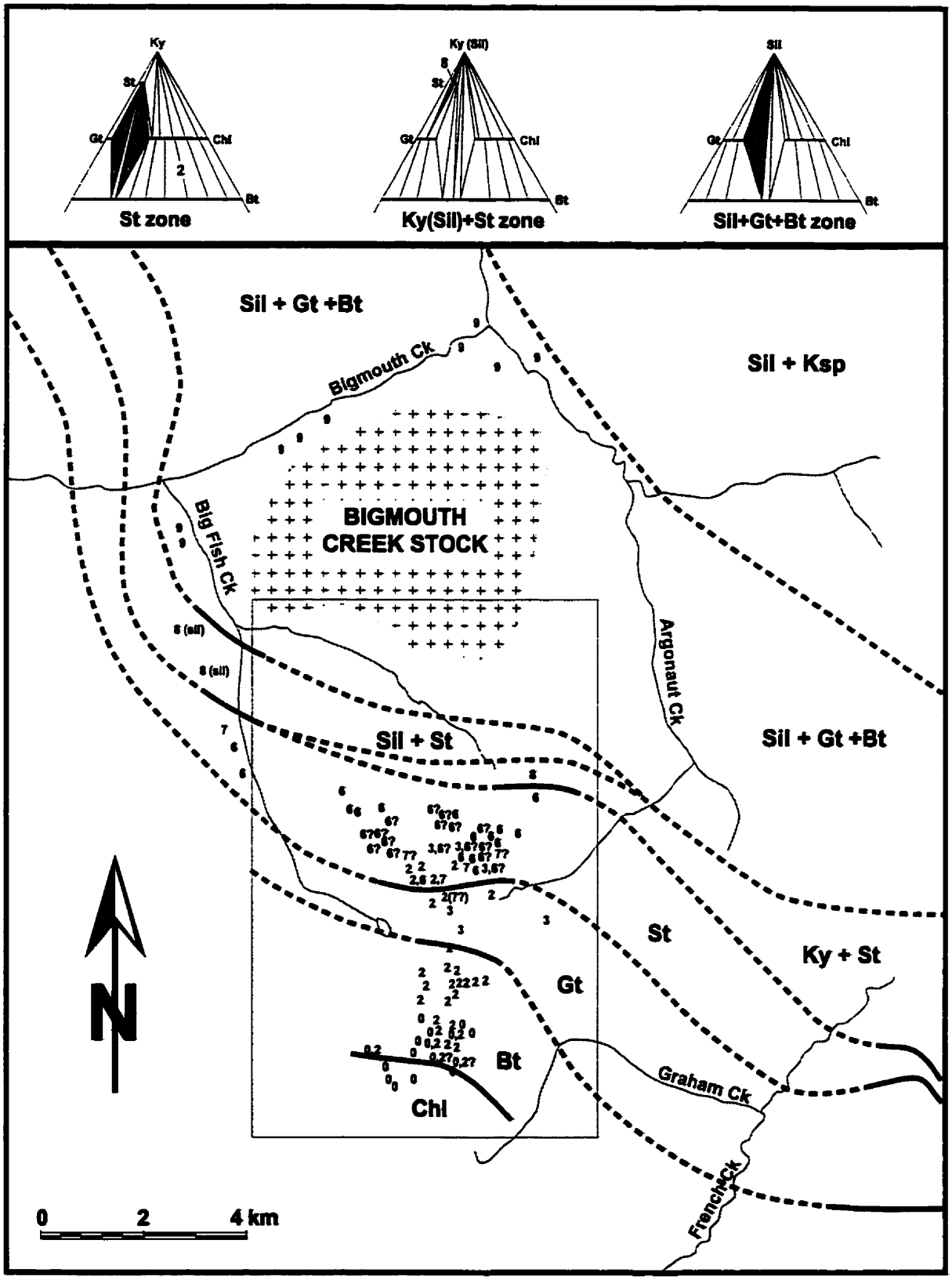

Figure 2.6 Distribution of mineral isograds and metamorphic assemblages recorded in pelitic rocks in the area surrounding the Bigmouth Creek stock. Mineral isograds are shown as heavy lines, and locations are either known (solid lines) or inferred (dashed lines). Location of main study area is indicated by box. Compiled from data by Franzen (1974), Van der Leeden (1976), Leatherbarrow (1981), Gibson and Höy (1985), and the present study. Mineral abbreviations are as in Figure 2.2.

Chlorite is generally present in rocks of the staurolite zone. Locally, it occurs as S_T-parallel, medium-grained flakes which are interpreted to be prograde with respect to M2 metamorphism. More commonly, it is found surrounding garnet porphyroblasts, but overgrown by staurolite. Abundant late chlorite of probable post-peak M2, retrograde timing, occurs as flakes which either cross-cut matrix structures or replace M2 prograde minerals (e.g., Plate 6A,B).

The development and/or preservation of staurolite in rocks of the staurolite zone is extremely heterogeneous. Throughout this zone, staurolite is commonly found adjacent to garnet porphyroblasts, associated with biotite ± chlorite (Plates 1B, 4A, 5A, 6A). Staurolite appears to post-date garnet in these instances, and this is confirmed by the local occurrence of small, euhedral, M2 garnets included in staurolite porphyroblasts (Plate 5A). Some staurolite occurs in the matrix away from garnet porphyroblasts (Plate 5D). Staurolite generally forms subhedral to euhedral, poikiloblastic grains. Grain size increases irregularly from about 1 mm in the lower staurolite zone, to over 1 cm in the upper part of this zone. Inclusion trails within staurolite porphyroblasts are generally straight, but the S_i/S_e relationships are irregular: some staurolite grains show relative rotation, others do not, and these variations may be observed within a single outcrop (Plate 5C,D). Staurolite is commonly partially to completely retrogressed to an intergrowth of fine muscovite ± chlorite flakes. Often, retrograde phyllosilicates after staurolite are aligned parallel to S_T (Plate 6B). In many pelitic outcrops in the staurolite zone no fresh staurolite was found. However, widespread occurrences on the outcrop or in thin section of staurolite-shaped mats rich in muscovite ± chlorite, typically in close association with garnet porphyroblasts which are more or less chloritized (Plate 6B) are interpreted to represent retrogressed, staurolite porphyroblasts. These occurrences are indicated in Figures 2.3 and 2.6 with a question mark.

The general association of staurolite and biotite overgrowing garnet with which chlorite is commonly associated, suggests that the staurolite producing reaction in these rocks is related to (Fig. 2.7):

garnet + chlorite + muscovite

-> staurolite + biotite + quartz + H_2O (2.4A).

This is the typical staurolite isograd univariant reaction in pelitic rocks metamorphosed at intermediate pressure for an ideal bulk composition in the K_2O - FeO - MgO - Al_2O_3 - SiO_2 - H_2O (KFMASH) system. In this system, equilibrium 2.4A is univariant so co-existing staurolite + garnet + biotite + chlorite should be restricted to the staurolite + biotite isograd surface. The widespread co-existence of these four phases in the study area is likely due to the increased thermodynamic variance

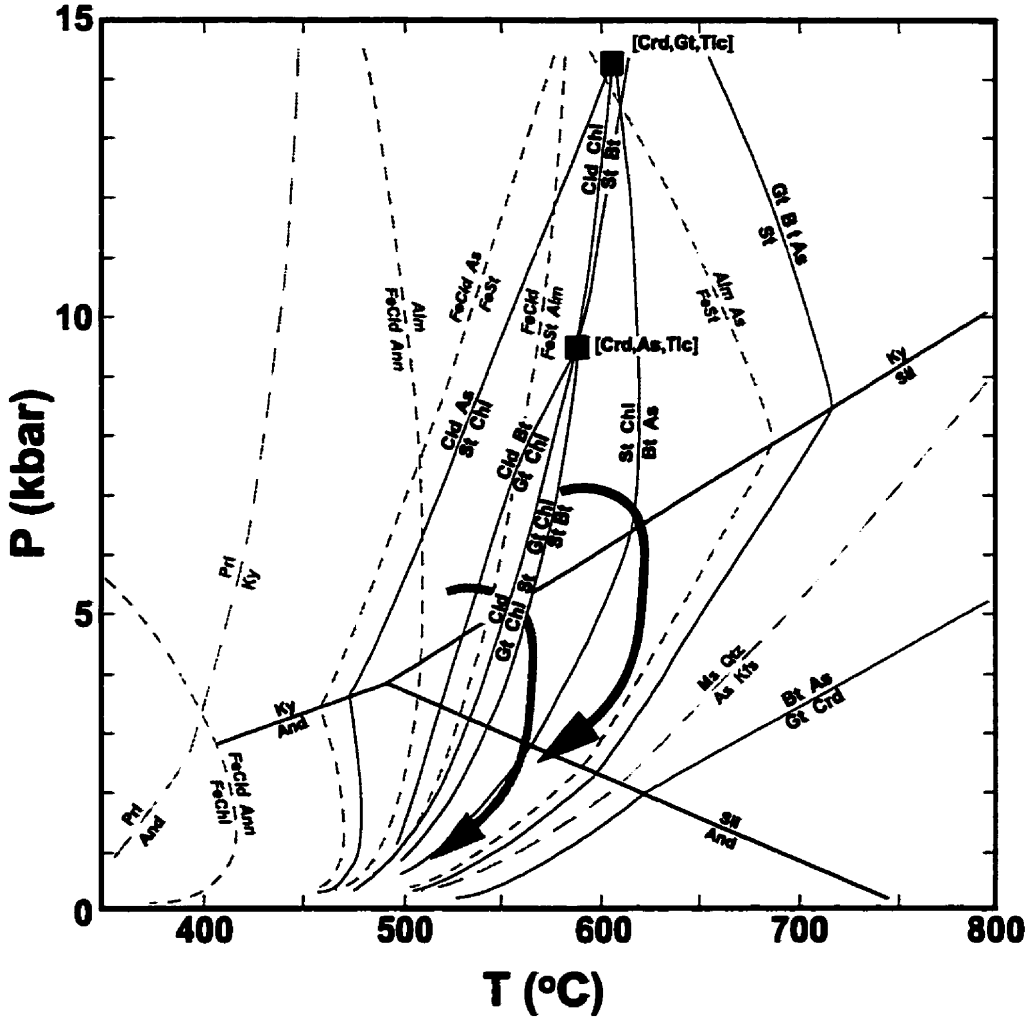

Figure 2.7 Petrogenetic grid for pelitic rocks in the K_2O - FeO - MgO - Al_2O_3 - SiO_2 -H_2O (KFMASH) system, modified after Spear and Cheney (1989). Short-dashed lines are equilibria in the KFASH sub-system, and long-dashed lines are equilibria in the KASH sub-system. Black squares are KFMASH invariant points with absent phases shown in brackets. Inferred pressure-temperature paths for rocks of the M2 staurolite zone (gray) and of the kyanite + staurolite zone (black) are shown. See text for discussion. Abbreviations are: Alm: almandine; And: andalusite; Ann: annite; As: alumino-silicate; Crd: cordierite; FeCld: Fe-chloritoid; FeSt: Fe-staurolite; Ms: muscovite; Qtz: quartz; Tlc: talc; others are as in Figures 2.3.

resulting from additional components, such as Mn and Ca, consistent with the observation of significant spessartine and grossular components in garnet (Fig. 2.5), and widespread occurrence of plagioclase. A more realistic staurolite producing reaction in the study area is therefore:

garnet + chlorite + muscovite
-> staurolite + biotite + quartz + plagioclase + H_2O (2.4B).

Whitney and Ghent (1993) interpreted the co-existence of staurolite and garnet, as well as garnet compositional discontinuities, in pelitic rocks of the Solitude Range to the northeast of the Big Fish Creek area, to result from prograde reactions involving the consumption of chloritoid, which is preserved in these rocks as inclusions in garnet. Because chloritoid was not observed in the Big Fish Creek area, and because textural evidence strongly suggests a link between staurolite growth and garnet consumption, this scenario probably did not play a significant role here.

2.6.2.5 Kyanite + staurolite zone and beyond

Rocks in which kyanite and staurolite coexist were observed in a single outcrop in the northeast corner of the mapped area (Fig. 2.3). These rocks are similar to staurolite zone rocks, except for the sporadic occurrence of kyanite porphyroblasts spatially associated with garnet and staurolite (Plate 5B). As with other M2 minerals, kyanite commonly bears fractures at high angle to the dominant matrix foliation, S_T (Plate 5B). Kyanite is found in some pelitic layers and not in others, and where kyanite is absent, kyanite-grade rocks are similar to staurolite-grade rocks. The reader is referred to the previous section for a detailed description of phases other than kyanite.

Pelites in the kyanite + staurolite zone (Fig. 2.3) are characterized by a paragenesis including kyanite + staurolite + garnet + biotite + muscovite + quartz ± chlorite ± plagioclase. The persistence of staurolite in the kyanite stability field implies the isograd reaction (e.g., Spear and Cheney, 1989; Fig. 2.7):

staurolite + chlorite + muscovite + quartz ->
kyanite + biotite + H_2O (2.5A).

However, the reaction (Fig. 2.7),

staurolite + muscovite + quartz ->

kyanite + garnet + biotite + H_2O (2.6A)

can not be ruled out because kyanite is encountered only in one outcrop (the isograd-defining outcrop), in an assemblage which may represent the terminal AFM staurolite-breakdown reaction defined by reaction 2.6A. On the other hand, the lack of evidence for late garnet growth (e.g., Plate 5B), and the presence of a kyanite + staurolite zone of finite width immediately to the southeast of the study area (Figs. 2.2, 2.6; Leatherbarrow, 1981) is consistent with reaction 2.5A being the kyanite-in reaction in these rocks.

Kyanite was not found in the western part of the study area (Fig.2.3). West of Big Fish Creek, a staurolite + biotite zone gives way northward to a zone where staurolite and fibrolitic sillimanite co-exist in apparent equilibrium (Fig. 2.6). The spatial association of staurolite, chlorite (after garnet), biotite and fibrolite, and in particular, intergrowths of sillimanite and biotite (Plate 7A), suggest the reaction:

staurolite + chlorite + muscovite + quartz ->

sillimanite + biotite + H_2O (2.5B).

Alternatively, the occurrence of fibrolite and biotite intergrowths mimicking pre- to syn-kinematic garnet shapes (Plate 7A,B,C) could indicate that fibrolite grew on biotite pseudomorphs after garnet, produced by reaction 2.4. Kerrick (1987) postulated that fibrolite production after biotite is possible in the presence of Cl-rich fluids via a reaction such as:

biotite + HCl -> fibrolite + SiO_2 + KCl + $(Mg_xFe_{1-x})Cl_2$ + H_2O (2.7)..

and that reaction 2.7 can occur at temperatures below coarse ("crystalline") sillimanite stability.

Further north along Big Fish Creek, and north of the Bigmouth Creek stock are pelitic rocks characterized by the assemblage sillimanite + garnet + biotite. Staurolite is absent, and euhedral garnet overgrows fibrolitic to coarse-grained sillimanite + biotite aggregates (Plate 7B,C). At least some of these aggregates are pseudomorphs after early garnet as indicated by the preservation of inclusion-rich cores to these euhedral garnet porphyroblasts, which are locally rotated with respect to the external foliation, S_T, and are interpreted at least in part to be of M1 origin based on textural similarities with M1 garnet elsewhere, such as splitting (Plate 7B) and the inclusion-rich, anhedral nature of these cores (Plate 7C). Other aggregates of sillimanite and biotite may be pseudomorphs after staurolite. Sillimanite is

coarser in these rocks. It coexists with biotite as pseudomorphs of garnet ± staurolite and is a common matrix constituent (Plate 7D). These observations suggest the reaction (Fig. 2.7):

staurolite + muscovite + quartz ->

sillimanite + garnet + biotite + H_2O (2.6B).

The observed mineral assemblages are inferred to be synchronous with M2 mineral assemblages found throughout the map area (Fig. 2.3) based on two lines of evidence. First, occurrences of S_T-parallel, deformed sillimanite and biotite were encountered (Plate 7D), indicating that these assemblages developed before the end of ductile deformation. The second line of evidence hinges on the continuity of the mineral isograds they define with mineral isograds in adjacent areas. Based on the distribution of assemblages west of Big Fish Creek, isograds have been extrapolated to the northwest from the main study area, as illustrated in Figure 2.6. The mineral zones thus defined in the present study area tie in well with those of Gibson and Höy (1985) to the northwest (Fig. 2.6). The spatial continuity of the minerals zones shown in Figure 2.4 suggests that they are related to the same metamorphic recrystallization episode.

In the Mica Creek area (Fig. 2.2), the sillimanite isograd is sharp, defined by a zone a few tens of meters-wide at most, where kyanite and sillimanite co-exist (Ghent et al., 1977, 1980). In contrast, to the west of that area, kyanite and fibrolitic sillimanite co-exist over a 15 km-wide zone (Doucet et al., 1985; Sevigny and Ghent, 1986; and Digel et al., 1989; Digel et al., 1998; Fig. 2.2). One type of fibrolite occurrence described is "small knots intergrown with biotite" (Digel et al., 1989; p. 96), a texture very similar to that observed in the west and north of the Bigmouth Creek stock (Plates 7A,B,C). These authors postulated that fibrolite development may be related to temperature increase due to sporadic emplacement of small granitic bodies.

Although kyanite was not observed to co-exist with fibrolite in the present study area, it occurs in the kyanite + staurolite zone more or less along isogradic strike of the first fibrolitic sillimanite occurrence found to the west of the Bigmouth Creek stock (Fig. 2.6). It is possible that recrystallization, resulting either from a temperature increase (e.g., Digel et al., 1989) or decompression, of kyanite-bearing rocks to produce fibrolite resulted in the complete resorption of kyanite, during M2 metamorphism. Alternatively, the presence of fibrolitic sillimanite rather than kyanite in rocks west of the Bigmouth Creek stock may reflect a regional pressure gradient along strike of the isograds during M2 metamorphism.

2.6.2.6 Late-M2 andalusite

Splays of large muscovite ± chlorite pseudomorphs after andalusite (Plates 4B) are widespread in the M2 staurolite and, locally, garnet zones (Fig. 2.8). Andalusite retrogression is generally complete, but fresh andalusite was observed in a handful of outcrops. On the outcrop, the splays of porphyroblasts appear relatively undeformed (Plate 4B); they are well exposed in mica-rich layers parallel to the dominant foliation, S_T, but also cross-cut this foliation.

In thin section, andalusite porphyroblasts include grains of earlier-formed M2 mineral assemblages (Plate 4C,D). Locally, these porphyroblasts are boudinaged, with resulting fractures at high angle to S_T (Plate 6C). Matrix phyllosilicates locally wrap around the porphyroblasts. Muscovite ± chlorite pseudomorphs after andalusite consist of aggregates of fine flakes which are aligned with S_T to variable extents. In many cases, retrograde phyllosilicates showed strong alignment parallel to S_T (Plate 4D).

Where fresh andalusite and other M2 minerals are preserved, no evidence of intervening retrogression is observed (e.g., Plate 4C,D). Therefore, andalusite is interpreted to have developed in the late stages of M2 metamorphism. This interpretation is also consistent with the spatial correlation of occurrences of andalusite or pseudomorphs after andalusite, and the M2 staurolite zone (in particular, the fact that the appearance of andalusite coincides approximately with the M2 staurolite isograd; Fig. 2.8). Given the close spatial (Fig. 2.8) and textural (Plate 4C,D) association of andalusite and staurolite, the probable andalusite-forming reaction in these rocks is:

staurolite + chlorite + muscovite + quartz ->

andalusite + biotite + H_2O (2.5C).

This reaction is shown in Figure 2.7 to proceed at pressure below 2.5 kbar. In contrast, M2 kyanite production through reaction 2.5A took place at pressure in excess of 6 kbar (Fig. 2.7). This implies a pressure differential from the low-grade half of the staurolite + biotite zone to the kyanite-in isograd (i.e., approximately 1500 m) of almost 4 kbar, or a *minimum* pressure gradient of 2.6 kbar/km, which is unreasonable for crustal rock densities. Therefore, production of andalusite in the staurolite zone via reaction 2.5C implies substantial decompression (in excess of 3 kbar) during the late stages of M2 metamorphism (Fig. 2.7), following attainment of conditions leading to kyanite production in higher-

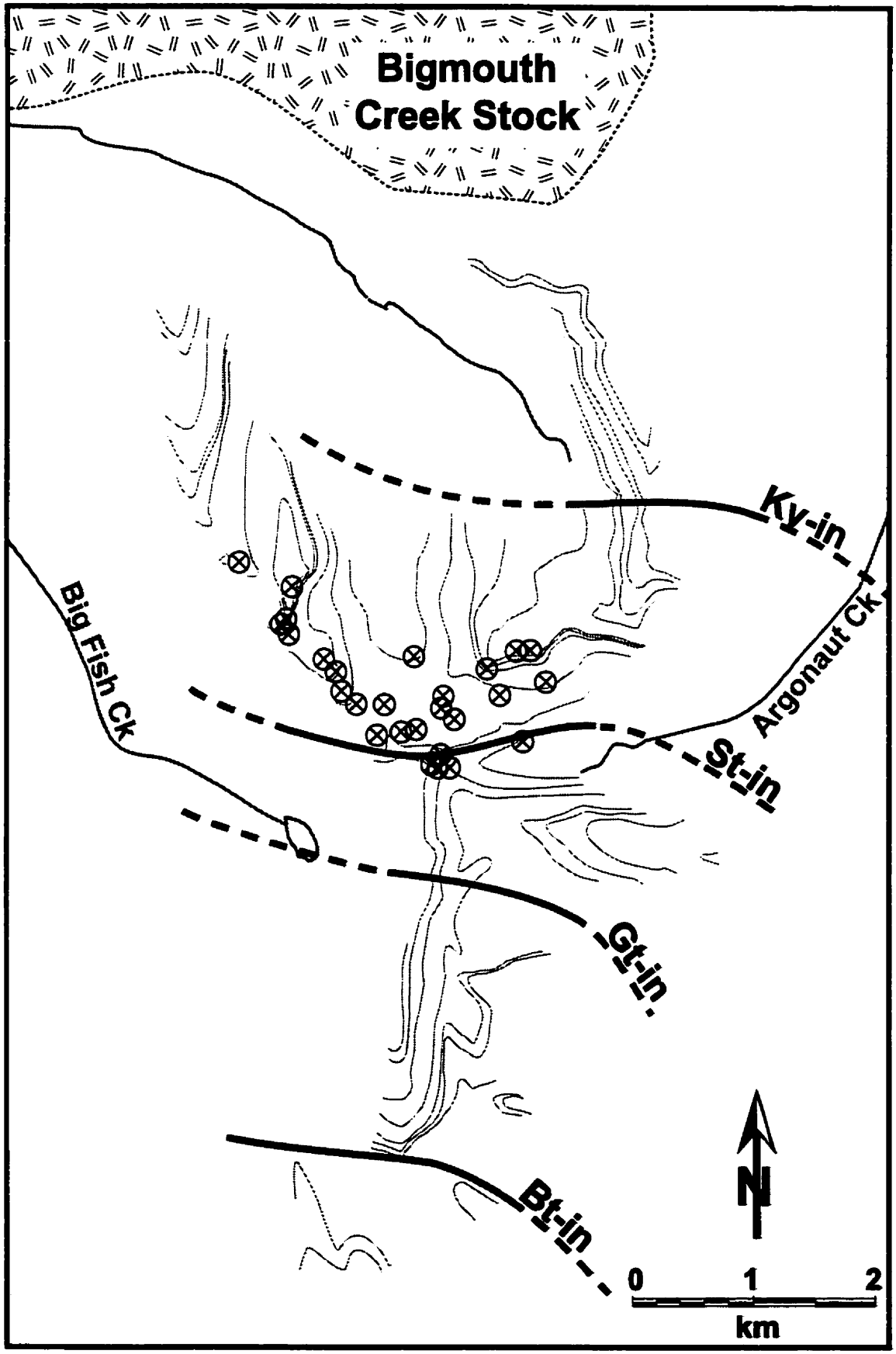

Figure 2.8 Occurrences of late, coarse-grained andalusite and retrograde pseudomorphs after andalusite in the study area.

grade rocks. Figure 2.7 shows schematic M2 pressure-temperature paths for rocks of the staurolite and of the kyanite + staurolite zones which are consistent with this interpretation. As shown in this figure, some staurolite-zone rocks, especially in the western part of the study area, may have reached M2 peak temperature in the sillimanite stability field, consistent with the observation of co-existing staurolite and sillimanite west of Big Fish Creek (Fig. 2.6; Plate 7A).

An alternative explanation for the presence of andalusite developed late in the metamorphic recrystallization history is that it is related to emplacement of an igneous body, such as the Bigmouth Creek pluton, within rocks of the Big Fish Creek area. Given the limited outcropping extent of the pluton (with a diameter of approximately 5 km; Fig. 2.6), it is unlikely that heat advected by this body would have effected substantial prograde recrystallization 3 km away, where andalusite is encountered. This conclusion is also supported by the lack of evidence for recrystallization to low-pressure assemblages of kyanite-bearing rocks in the M2 kyanite + staurolite zone, between the outcropping area of andalusite and the Bigmouth Creek stock. The interpretation of the presence of an intrusive body below (or above, and now eroded) the area characterized by andalusite, although somewhat ad hoc, can not be ruled out. However, occurrence of andalusite with kyanite inclusions at a locality approximately 10 km southeast of the Big Fish Creek area (M. Colpron, personal communication, 1994), suggests that andalusite development was regional in scale, and not restricted to the immediate vicinity of a hidden intrusive body.

2.7. Timing of Bigmouth Creek intrusion and metamorphism

The timing of regional metamorphism on the west flank of the Selkirk Fan structure has been interpreted as mid-Jurassic based on observed timing relationship between deformation, metamorphism and emplacement of intrusive bodies which have yielded mid-Jurassic crystallization ages (e.g., Wheeler, 1965; Archibald et al., 1983; Brown et al., 1992a; Colpron et al., 1996).

Wheeler (1965) and Van der Leeden (1976) have interpreted the age of emplacement of the Bigmouth Creek stock, exposed in the northern part of the study area, to be ca. 170 Ma based on compositional and textural similarities with other mid-Jurassic intrusions in the area. Van der Leeden (1976) interpreted the peak of regional metamorphism in the area to pre-date or to be synchronous with emplacement of the Bigmouth Creek stock, and based on this, inferred that peak regional metamorphism in the area was mid-Jurassic or older.

A sample of K-feldspar-megacrystic, hornblende- and biotite-bearing quartz monzonite from the Bigmouth Creek stock was dated by U-Pb geochronology of magmatic zircon and titanite. Instrumental analysis was performed by Richard Friedman and Jim Mortensen in the geochronology laboratory at the University of British Columbia and results are presented in Figure 2.9. Six zircon fractions define a linear trend with an upper intercept at 1.75 ● 0.02 Ga, and a lower intercept at 157 ± 3.3 Ma (MSWD = 182). The lower intercept age corresponds to the magmatic zircon crystallization age during emplacement of the Bigmouth Creek pluton; the upper intercept represents a component of inherited zircon that was present in all fractions. The two concordant titanite fractions gave $^{206}Pb/^{238}U$ ages of 140.5 ± 0.8 Ma and 137.4 ● 1.4 Ma.

These results indicate that emplacement and crystallization of the Bigmouth Creek stock occurred in latest Middle to earliest Late Jurassic (i.e., 157 Ma). The younger titanite ages could be interpreted in two ways: 1) the pluton cooled very slowly to reach titanite U-Pb closure temperature (ca. 600 °C) approximately 17-20 m.y. after crystallization of zircons; 2) the pluton cooled to below 600 °C prior to 140 Ma, and titanite ages record resetting of the U-Pb system by a heating event at ca. 140 Ma. Although the data are permissive of both interpretations, the second scenario is tentatively favored for a number of reasons. Firstly, the presence of magmatic epidote in Bigmouth Creek granodiorite suggests that initial emplacement of the intrusive body was at depths well in excess of 20 km (i.e., pressure in excess of 6 kbar; Zen and Hammarstrom, 1984; Zen, 1985). Magmatic epidote is commonly observed in mid-Jurassic hornblende-bearing intrusions in the southern Omineca Belt, and has been interpreted by previous authors to be consistent with crystallization at substantial depth (Ghent et al., 1991; Colpron et al., 1996). Magmatic epidote in the Bigmouth Creek pluton implies that country rocks were at mid-crustal temperature and pressure conditions in late mid-Jurassic time. Because mid-Jurassic metamorphism is common in other parts of the SFA (e.g., Archibald et al., 1983; Brown et al., 1992; Colpron et al., 1996), M1 metamorphism recorded in rocks of the study area is tentatively interpreted to reflect these mid-crustal conditions attained at about the time of emplacement of the Bigmouth Creek pluton (i.e., M1 metamorphism is mid-Jurassic). Retrograde assemblages developed on M1 garnet porphyroblasts, and on which M2 garnet overgrowths were overprinted (see Section 2.6.1 above) indicate that a significant cooling interval affected rocks in the area between M1 and M2 prograde recrystallization events. M2 metamorphism therefore represents a distinct thermal pulse which is interpreted to be related to resetting of titanite U-Pb systematics in rocks of the Bigmouth Creek stock. In other words, the M2 metamorphic overprint in the area is interpreted as Early Cretaceous, the timing of this resetting.

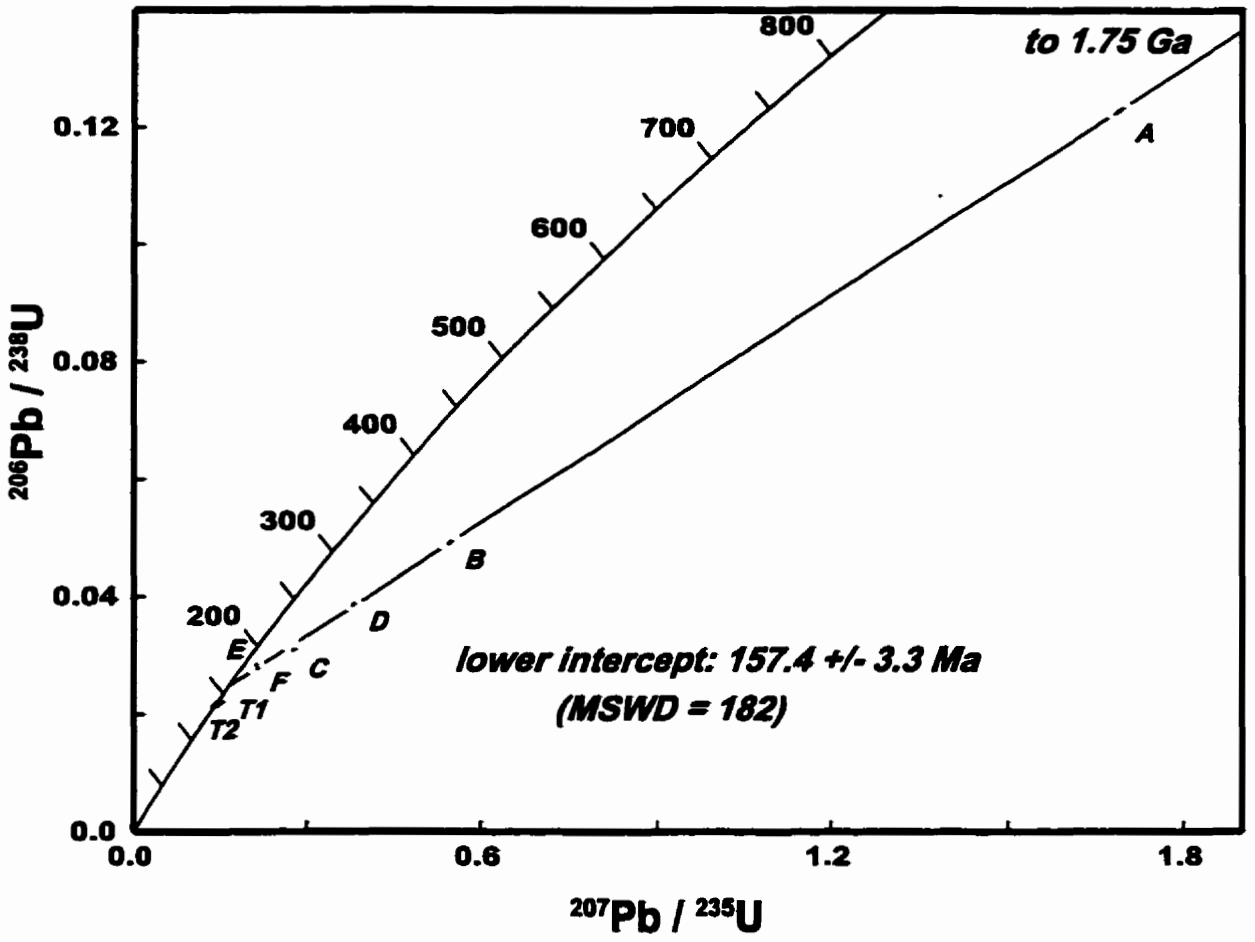

Figure 2.9 U-Pb concordia plot of zircon and titanite analyses for Bigmouth Creek K-feldspar megacrystic, hornblende and biotite-bearing granodiorite sample. Straight line is best fit linear regression to results obtained from five zircon fractions (A-F, a sixth fraction, C, was excluded); lower intercept is at 157 ± 3.3 Ma, upper intercept is at 1.75 ± 0.02 Ga. Titanite results for two fractions are also shown (T1 and T2). They define $^{206}Pb/^{238}U$ ages of 140.5 ±0.8 Ma and 137.4 ± 1.4 Ma, respectively.

It should be noted that the above discussion and ensuing conclusions regarding the timing of M1 and M2 metamorphic events are based on limited absolute timing constraints on an intrusive body, and that direct ages for metamorphic recrystallization in the country rocks are as yet unavailable. Therefore, interpretations based on these conclusions remain tentative until more extensive absolute timing constraints are available.

2.8 Discussion

Rocks of the study area record a polycyclic Mesozoic metamorphic history. As discussed at length in the following chapter, ductile deformation associated with long-lived development and maintenance of a regional transposition foliation, S_T, was attended and outlived by both M1 and M2 metamorphic pulses. This is evidenced by the S_T-parallel inclusion trails in M1 porphyroblasts (e.g., Plate 1A), and S_T parallel alignment of retrograde minerals after M2 porphyroblasts (Plate 6B,D). Geochronological constraints on crystallization and subsequent thermal resetting of minerals of the Bigmouth Creek granitoid intrusion, as well as correlation with timing of metamorphism in nearby areas places a Middle to Late Jurassic age (ca. 157 Ma, the U-Pb age of zircon crystallization) on M1 metamorphism, and suggests that M2 prograde recrystallization occurred in latest Jurassic to Early Cretaceous time (ca. 140 Ma, age of final U-Pb closure of titanite). This implies that rocks in and around the study area were part of a long-lived orogenic belt affected by episodic deformation and metamorphism over several tens of millions of years at least, in Jurassic to Cretaceous time.

Evidence for multiple garnet growth episodes have been reported from the Northern Selkirk Mountains and nearby areas by previous works (immediately to the northeast, Perkins, 1983; in the North Adams river area to the north, Sevigny and Ghent, 1986; in the Cariboo Mountains to the northwest, Currie, 1988; in the Solitude Range to the east, Gal and Ghent, 1990; Whitney and Ghent, 1993). None of these authors related these textures to distinct, overprinting thermal pulses. On the other hand, geochronological arguments have been presented which suggest a complex and prolonged thermal history for rocks of the Selkirk Allochthon. Based on geochronological evidence, Scammell (1993) argued that rocks in the hangingwall of the Monashee Décollement, in the Monashee Mountains to the west of the present study area (Fig. 2.2) record diachronous metamorphism and deformation over a time interval in excess of 40 m.y., from ca. 140 Ma to ca. 100 Ma. More recently, Crowley et al. (1998) presented geochronological evidence for two distinct thermal pulses, of mid-Jurassic and mid-Cretaceous age, respectively, having affected rocks in the Mica Creek area, to the north of the study area. In addition,

Colpron (personal communication, 1996) obtained Late Cretaceous (ca. 75 Ma) Ar-Ar ages on micas from the Groundhog Basin, at the southern end of the study area.

Based on barometry and Ar-Ar geochronometry, Colpron et al. (1996) argued that rocks in the vicinity of the Fang stock, to the south of the Big Fish Creek area (Fig. 2.2), underwent substantial and rapid exhumation immediately after regional metamorphism around 170-168 Ma. In contrast, development of kyanite-bearing assemblages during M2 in Early Cretaceous time in the Big Fish Creek area implies that if these rocks were substantially exhumed in mid-Jurassic time, they subsequently underwent significant burial between the Middle Jurassic and the Early Cretaceous. Alternatively, the discrepancy may represent spatially variable tectonic evolutions for rocks in different parts of the Selkirk Allochthon.

Parrish (1995) integrated available geochronological information on the timing of regional metamorphism in the Selkirk Allochthon and argued that there exists a consistent relationship between timing of metamorphism and structural level in the Selkirk Allochthon: progressively structurally deeper rocks appear to record progressively younger regional metamorphic recrystallization. The results of this study are consistent with, and reinforce this interpretation of the spatial diachroneity of regional metamorphism by showing that the timing of M2 metamorphism in the northern portion of the southwest flank of the Selkirk Fan structure is intermediate between that of metamorphism in areas to the south, at higher structural levels (Figs. 2.1, 2.2; Archibald et al., 1993; Brown et al., 1992a; Colpron et al., 1996), and to the north and west, at lower structural levels (Figs. 2.1, 2.2; Sevigny et al., 1989, 1990; Scammell, 1993). However, this study shows that in addition to being spatially diachronous, metamorphism in the Selkirk Allochthon was episodic and polycyclic.

Crowley et al. (1999) present geochronologic evidence for spatially limited and diachronous thermal events in the Monashee Mountains north of the Big Fish Creek area. These authors argue for local heat sources (e.g., plutonism) to account for this restricted spatial extent of thermal overprints. The Bigmouth Creek pluton is the only exposed magmatic body of volumetric significance in the area, and its emplacement may have contributed to the thermal event which led to prograde metamorphic recrystallization (e.g., M1, in mid-Jurassic time). On the other hand, despite the apparent geometric relationship between M2 metamorphic zones and isograds, and the outcropping area of the Bigmouth Creek pluton, it is unlikely that a pluton 5-6 km in diameter (see Fig. 2.6) would have a significant thermal effect on country rock located $\geq$ 4 km away, which is the case for rocks which define M2 metamorphic zones and isograds in the Big Fish Creek area. It is possible that the Bigmouth Creek pluton

extends at depth below these rocks, or that there is a distinct intrusive body in that location, but the lack of surface exposure of these potential heat sources makes it impossible to assess their importance. On the other hand, spatial continuity of M2 metamorphic isograds in the area, with those mapped in adjacent areas to the southeast and northwest (Fig. 2.6; Van der Leeden, 1976; Leatherbarrow, 1981) suggests a regional cause for the thermal overprint.

A tectonic model, based on numerical models of a critically-tapered, doubly-vergent orogenic wedge (Willett et al., 1993), is presented in Fig. 2.10 which integrates the foregoing observations and interpretations of metamorphic evolution of rocks of the study area. Docking of the Quesnellia Superterrane at the western edge of North America (e.g., Monger et al., 1982), and continued contraction, in Early to mid-Jurassic time, resulted in thickening of the North American miogeoclinal sequence into a critically-tapered, active tectonic wedge (Fig. 2.10A). Middle to Late Jurassic M1 metamorphism resulted from thermal relaxation of this thickened wedge (e.g., England and Thompson, 1984), coeval with emplacement of the Bigmouth Creek pluton at depths well in excess of 20 km. Thermal relaxation at depth lead to establishment of a ductile crustal root, which may have allowed the maintenance of a stable plateau area, during continued contraction and eastward translation of Quesnellia and of the continental margin sedimentary sequence (Fig. 2.10B). Evidence of retrogression between M1 and M2 prograde metamorphic events suggests that growth of the orogenic wedge was episodic, with intervening periods during which erosion (tectonic or otherwise) might have prevailed over contraction. Significant relaxation of far-field stresses, and/or expansion of the area of ductile lower crust due to M2-related heating in latest Jurassic-Early Cretaceous resulted in gravitational collapse of the wedge, accommodated at upper to middle crustal levels by orogen-parallel and orogen-transverse spreading, as demonstrated in the following chapter (Fig. 2.10C). In addition to abundant structural evidence presented in Chapter 3 for extensional ductile deformation, late-M2 development of andalusite supports the interpretation of tectonic erosion by extensional deformation. This model of a long-lived, dynamical orogenic wedge affected by compressional deformation due to overall crustal contraction, and by extensional deformation associated with gravitational collapse of the overly thickened wedge is in agreement with similar interpretations proposed recently for rocks of the Selkirk Allochthon in nearby areas of the Monashee Mountains (Scammell, 1993; Johnston, 1996; also see Brown et al., 1993).

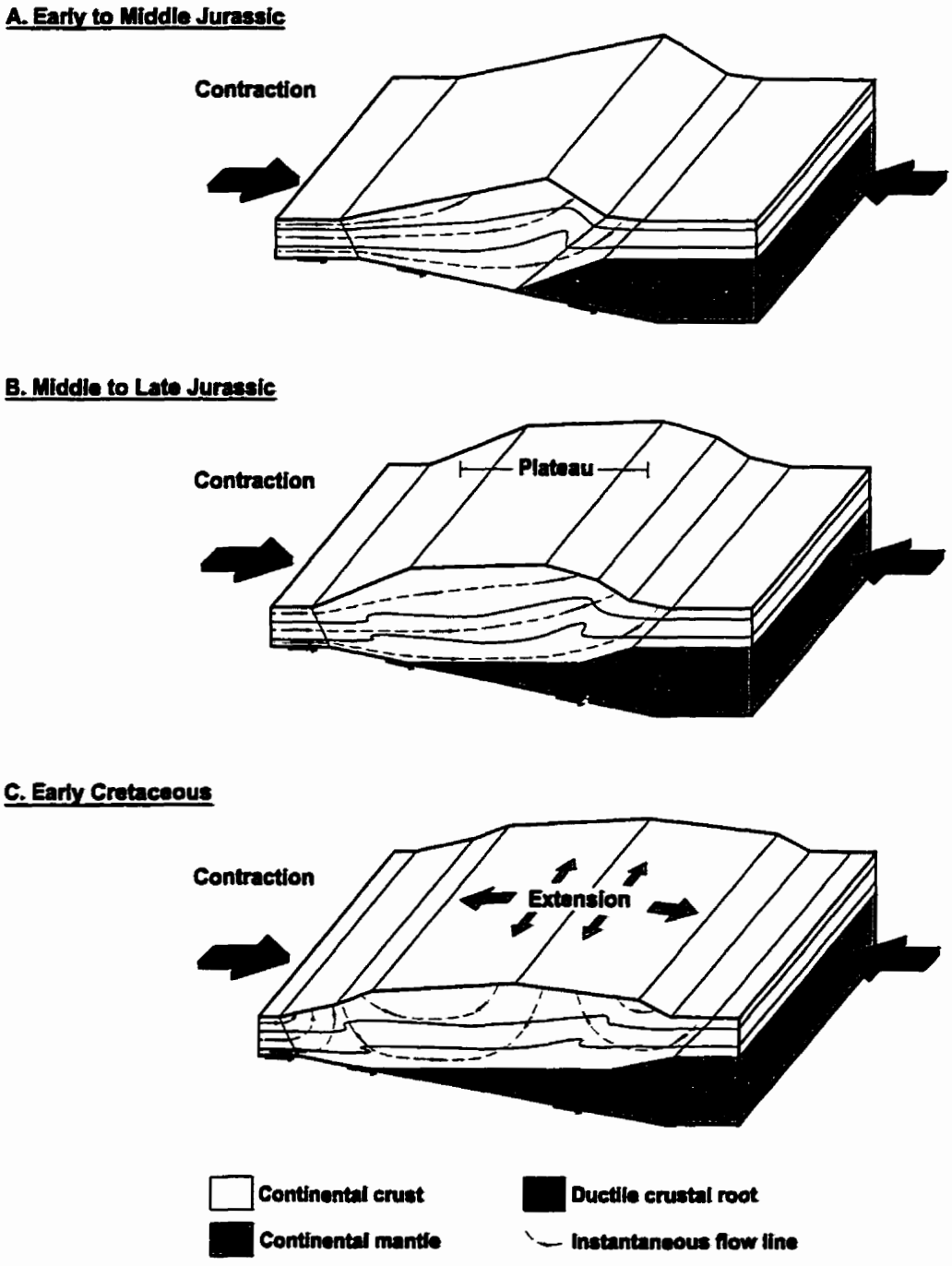

Figure 2.10 Proposed dynamic wedge tectonic model for the Selkirk Allochthon to account for inferred metamorphic and structural evolution. Modified after Willett et al., 1993. A: Early accretion of westerly-derived terrane to the western edge of North America and associated contraction leads to crustal thickening, thermal relaxation of thickened wedge, and results in M1 metamorphic event. B: A stable wedge geometry is established which is maintained by the balance of far-field contractional stresses and expansion of ductile crustal root due to continued thermal relaxation. Parts of the orogenic wedge undergo burial while others are uplifted, accounting for limited retrogression between M1 and M2 metamorphic event. Continued growth of the wedge and associated thermal relaxation locally (at least) produce heating and result in M2 metamorphism C: Relaxation of far-field contractional stresses and/or expansion of the ductile crustal root leads to substantial gravitational collapse of the dynamic wedge, during the late stages of M2 metamorphism. Resulting extension produces denudation and decompression as recorded by development of late-M2 andalusite.

2.9 Conclusions

This chapter presents the results of a field and laboratory study of the thermal and metamorphic evolution of rocks of the Selkirk Allochthon on the western flank of the Selkirk Fan structure of the southern Omineca Belt of British Columbia. Implications of these results are discussed in the previous section. The main conclusions derived from these results are listed below.

1. Two distinct metamorphic events affected rocks in the Big Fish Creek area:

- M1, the earlier event, is recorded by relict porphyroblastic minerals which were subjected to cooling and retrogression prior to development of M2 prograde mineral assemblages. M1 was probably regional in extent;

- M2 is characterized by a Barrovian sequence of metamorphic zones in the Big Fish Creek area. From south to north, this field gradient includes the following metamorphic zones in rocks of pelitic composition: chlorite, biotite, garnet, staurolite, kyanite + staurolite. Late-M2 andalusite is widespread in rocks of the garnet and staurolite zones, suggesting substantial late-M2 decompression.

2. The Bigmouth Creek stock was emplaced in late Middle Jurassic as indicated by magmatic zircon U-Pb ages (157 ● 3.3 Ma). Magmatic epidote in Bigmouth Creek granodiorite suggests that emplacement depth was substantially greater than 20 km. Earliest Cretaceous U-Pb ages (140.7 ± 0.8 Ma and 137.4 ± 1.4 Ma) from titanite from the granodiorite are interpreted to be due to thermal resetting at that time.

3. Based on evidence for widespread mid-Jurassic metamorphism in other areas of the Selkirk Allochthon, and for deep emplacement of the Bigmouth Creek pluton at that time, M1 metamorphism is interpreted to be of mid-Jurassic age.

4. M2 is interpreted to be the result of the same thermal pulse which caused resetting of U-Pb systematics of titanite in the Bigmouth Creek pluton in Early Cretaceous time Thus, timing of M2 metamorphism is Early Cretaceous.

5. Ductile deformation associated with a long-lived transposition foliation was ongoing, in that part of the Selkirk Allochthon, from prior to the peak of M1 metamorphism in mid-Jurassic time, to after the peak of M2 in Early Cretaceous time.

6. Consistent with the foregoing conclusions, the Selkirk Allochthon in and around the study area is interpreted to represent a dynamic orogenic wedge which actively reacted to changes in external and internal parameters (far-field stresses and rheological modifications) over at least 20 m.y. in Jurassic to Cretaceous time, and probably longer, as suggested by constraints from adjacent areas. This model is supported by the structural analysis of these rocks presented in the following chapter.

Chapter 3

OROGEN-PARALLEL AND OROGEN-TRANSVERSE SYN-COMPRESSIONAL EXTENSION, AND LONG-LIVED STRUCTURAL EVOLUTION OF THE SELKIRK ALLOCHTHON OROGENIC WEDGE, BRITISH COLUMBIA, CANADA

3.1 Introduction

In the last 15 years, the concept of a fold and thrust belt as a dynamic, critically-tapered wedge (Davis et al., 1983; Dahlen et al., 1984; Dahlen, 1984) has been applied to whole orogenic belts (e.g., Malavieille, 1984; Stockmal et al., 1986; Jamieson and Beaumont, 1988; Willett et al., 1993). In parallel, evidence for syn-compressional extension in a number of orogenic belts has been assigned to maintenance of a stable ("critical") geometry in response to crustal thickening by compression, and associated rheological changes due to thermal relaxation following thickening (e.g., Burchfield and Royden, 1985; Jamieson and Beaumont, 1988; Holdsworth and Grant, 1990; Hodges and Walker, 1992; Hodges et al., 1993; Diez Balda et al., 1995).

Recently, Scammell (1993) brought to light evidence for long-lived deformation resulting in sustained transposition of structural elements in rocks at the base of the Selkirk Allochthon (Read and Brown, 1981), an orogenic wedge exposed in the southeastern Canadian Cordillera (Fig. 3.1). Scammell (1993) interpreted extensional structures in these rocks as syn-compressional, and proposed a tectonic model involving extrusion (e.g., Burchfield and Royden, 1985; Thompson et al., 1997) at the base of the Allochthon by contemporaneous east-directed thrusting linked to development of the Rocky Mountain Foreland belt to the east, and extension along a west-vergent ductile shear zone (also see Johnston, 1996). Scammell (1993) argued that the Selkirk Allochthon represents a long-lived dynamic wedge, and that syn-compressional extension recorded near the base of the wedge is the result of gravitational collapse following overthickening.

This extrusion model for the base of the Selkirk Allochthon, however, contrasts with interpretations of the deformation at higher levels in the Selkirk Allochthon wedge in terms of discrete events linked to specific changes in the geometry of the wedge boundaries (e.g., Brown et al., 1986; Price, 1986; Brown and Lane, 1988; Colpron et al., 1998). Long-lived, "dynamic" maintenance of an active orogenic wedge is also difficult to reconcile with a recent interpretation by Parrish (1995) of eastward,

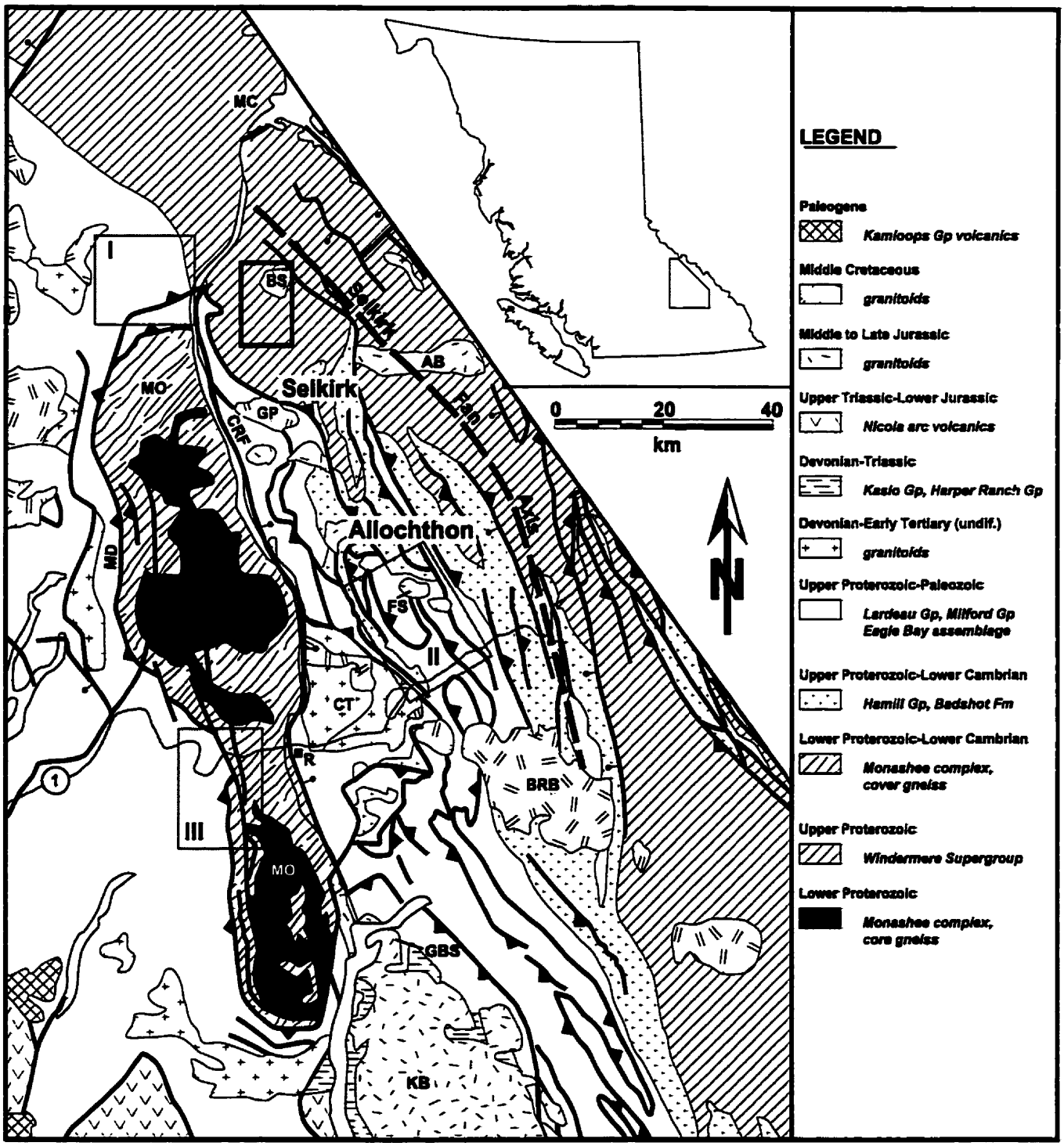

Figure 3.1 Lithotectonic map of the Southern Omineca Belt. Thick black box shows location of present study area. Gray boxes are locations of recent studies in nearby areas: I. Scammell (1993); II. Colpron et al. (1996); III. Johnston, 1996. AB: Adamant Batholith; BS: Bigmouth Creek Stock; BRB: Battle Range Batholith; CRF: Columbia River Fault; CT: Clachnacudainn Terrane; FS: Fang Stock; GBS: Galena Bay Stock; GP: Goldstream Pluton; KB: Kuskanax Batholith; MC: Mica Creek area; MD: Monashee Décollement; MO: Monashee Complex; R: town of Revelstoke. Modified after Wheeler and McFeely (1991).

and downward progression, over time, of metamorphic and associated deformational activity in the Selkirk Allochthon.

Of particular importance in resolving these apparent conflicts is the nature and timing of deformation in the internal parts of the orogenic wedge. Recognition of long-lived deformation, and in particular, cycles of compression and thickening, and resulting heating and gravitationally-driven extension, would favor a long-lived "dynamic wedge" model for the Selkirk Allochthon. On the other hand, evidence for discrete, and stylistically distinct deformation events, and for a spatial progression in the temporal distribution of metamorphic recrystallization events (i.e., structurally downward younging trend of metamorphism; Parrish, 1995) would tend to favor a model dominated by downward, and foreland migration of deformation and metamorphic "fronts" over time.

This chapter presents a study of the structural elements observed in the Big Fish Creek area of the Selkirk Allochthon, in the Northern Selkirk Mountains of British Columbia (Fig. 3.1). Rocks in this area are of particular interest because they preserve the record of a protracted and complex history of metamorphic recrystallization (see previous chapter) which can be used to unravel the associated deformation events. This is in contrast to other areas in the Selkirk Allochthon where the record of deformation and metamorphism is less complete, either because of early cessation of deformation and metamorphic activity, or because of continued reworking until the late stages of orogenic evolution which obliterated the record of early evolution of the orogenic wedge. Structural elements and style observed at intermediate levels of the Selkirk Allochthon suggest a history of protracted ductile deformation in a regionally significant shear zone from as early as the Middle Jurassic, to at least as late, and probably later than the Early Cretaceous. As argued below, ductile deformation involved non-coaxial strain associated with eastward thrusting of the wedge, and with west-verging syn-compression extensional strain internal to the wedge, as well as substantial sub-vertical shortening (i.e., orogen-parallel and orogen-transverse coaxial extension). The style of deformation in the Big Fish Creek area suggests that the Selkirk Allochthon orogenic wedge was a long-lived, dynamic entity affected by external and internal forces (terrane convergence, gravity), and by deformation (compressional and extensional) of the wedge in response to these driving forces.

3.2 Geological setting

3.2.1 Tectonic environment

The study area is located within the southern Omineca Belt, an orogenic core zone developed as a result of collision and accretion to the western margin of North America of westerly-derived terranes during Mesozoic to Early Cenozoic time (Fig. 3.1; Monger et al., 1982). Rocks underlying the study area are part of the Selkirk Allochthon, a package of Late Proterozoic to Paleozoic North American continental margin rocks which was thrust eastward as much as 250-300 km during accretion and continued convergence (e.g., Price and Mountjoy, 1970; Read and Brown, 1981; Brown et al., 1993). Displacement of the Selkirk Allochthon has been interpreted to have taken place in part along the Monashee Décollement, a zone of intense ductile shear exposed to the west of the study area (Read and Brown, 1981; Journeay, 1986; Brown and Journeay, 1987). The Monashee Décollement is interpreted to separate the basement and cover sequence of the Monashee Complex structural culmination from the overlying Selkirk Allochthon (e.g., Read and Brown, 1981; Brown and Read, 1983; Journeay, 1986; Scammell, 1993), and to extend as the root zone of the basal décollement to the Rocky Mountain thrust and fold belt to the east (Brown et al., 1992b). Brown et al. (1992b) have also interpreted the Monashee Décollement itself as representing the roof thrust to a series of basement-rooted, east-directed thrusts, the combined displacement of which matches the inferred shortening in the Rocky Mountain foreland belt (also see Cook et al., 1992). Recently, however, some workers have questioned the existence of the Monashee Décollement as a discrete shear zone (e.g., Williams and Jiang, 1999).

Regionally, rocks of the Selkirk Allochthon record a complex and protracted deformation and metamorphic history associated with Mesozoic convergence, and regional extensional deformation at least as early as the Late Paleocene (e.g., Parrish et al., 1988; Carr, 1991, 1992; Parrish, 1995). The stratigraphic and metamorphic framework of rocks in and around the study area are briefly reviewed below. The structural evolution of these rocks is the main focus of this chapter.

3.2.2 Stratigraphy

Rocks in the study area have been alternatively interpreted as belonging to the Upper Proterozoic Windermere Supergroup (e.g., Wheeler, 1965; Brown et al., 1977, 1978; Brown and Tippett, 1978) or the Lower Paleozoic Lardeau Group (e.g., Brown and Lane, 1988; Logan and Colpron, 1995). The controversy stems in large part from the fact that these rocks are strongly deformed, recording intense

isoclinal folding, non-coaxial shearing and transposition, imparting significant uncertainty to attempts at regional correlation. In addition, few stratigraphic top indicators have been observed, and because of widespread isoclinal folding, it is extremely difficult to ascertain the large-scale stratigraphic facing in the area. In any case, detailed stratigraphic correlation is beyond the scope of this study and the "stratigraphic" framework described below does not rest on any interpretation of relative age: rock units are distinguished in terms of their respective structural, not stratigraphic, levels.

The rocks mapped can be subdivided into four broadly defined packages separated by gradational contacts (Fig. 3.2). The structurally lowest package comprises centimeter- to meter-thick psammitic and semi-pelitic layers typically separated by thin (mm) mica-rich laminae. The lower boundary of this package was not identified within the bounds of the study area. Of particular note is the presence, near the top of this package, of several intervals of coarse gritty psammite, up to several meters in thickness, characterized by quartz and feldspar porphyroclasts which are commonly highly strained. These gritty intervals are found across the study area and hence are useful markers (Fig. 3.2).

This psammite/semi-pelite package is structurally overlain by 100-200 meters of dominantly pelitic schist compositionally layered on a cm- to dm-scale. Calc-pelitic schist and brown-weathering impure marble become abundant towards the top of this pelitic interval. This transition defines a gradational contact with the overlying package, which consists of approximately equal amounts of pelitic, and calc-pelitic schist, with sporadic occurrences of cm- to dm-thick impure marble layers, and more rarely, of massive chlorite schist or amphibolite, depending on metamorphic grade (Fig. 3.2). In the northern part of the area, this calc-pelitic package gives way up-section to a sequence of brown-weathering, impure to relatively pure calcite, and dolomite marbles, associated with more amphibolite and locally, thin intervals of talc-schist (Fig. 3.2). Particularly noticeable are thick (several tens of meters) intervals of rusty brown-weathering dolomitic marble.

The Bigmouth Creek pluton (Wheeler, 1965) is exposed at the northern limit of the study area. It consists of K-feldspar porphyritic, magmatic epidote-bearing, hornblende granodiorite. Late Jurassic to Early Cretaceous U-Pb ages on zircon and titanite from the Bigmouth Creek granodiorite were obtained as part of this study (see previous chapter). As discussed in the latter part of this chapter, the presence of magmatic epidote, indicating emplacement of the granodiorite body at substantial depth, along with the U-Pb ages provide a lower limit on the timing of a high-pressure metamorphic event which affected rocks of the study area (see next section). This has implications for the timing of extensional deformation and associated decompression in the area. These points are discussed in Section 3.4.

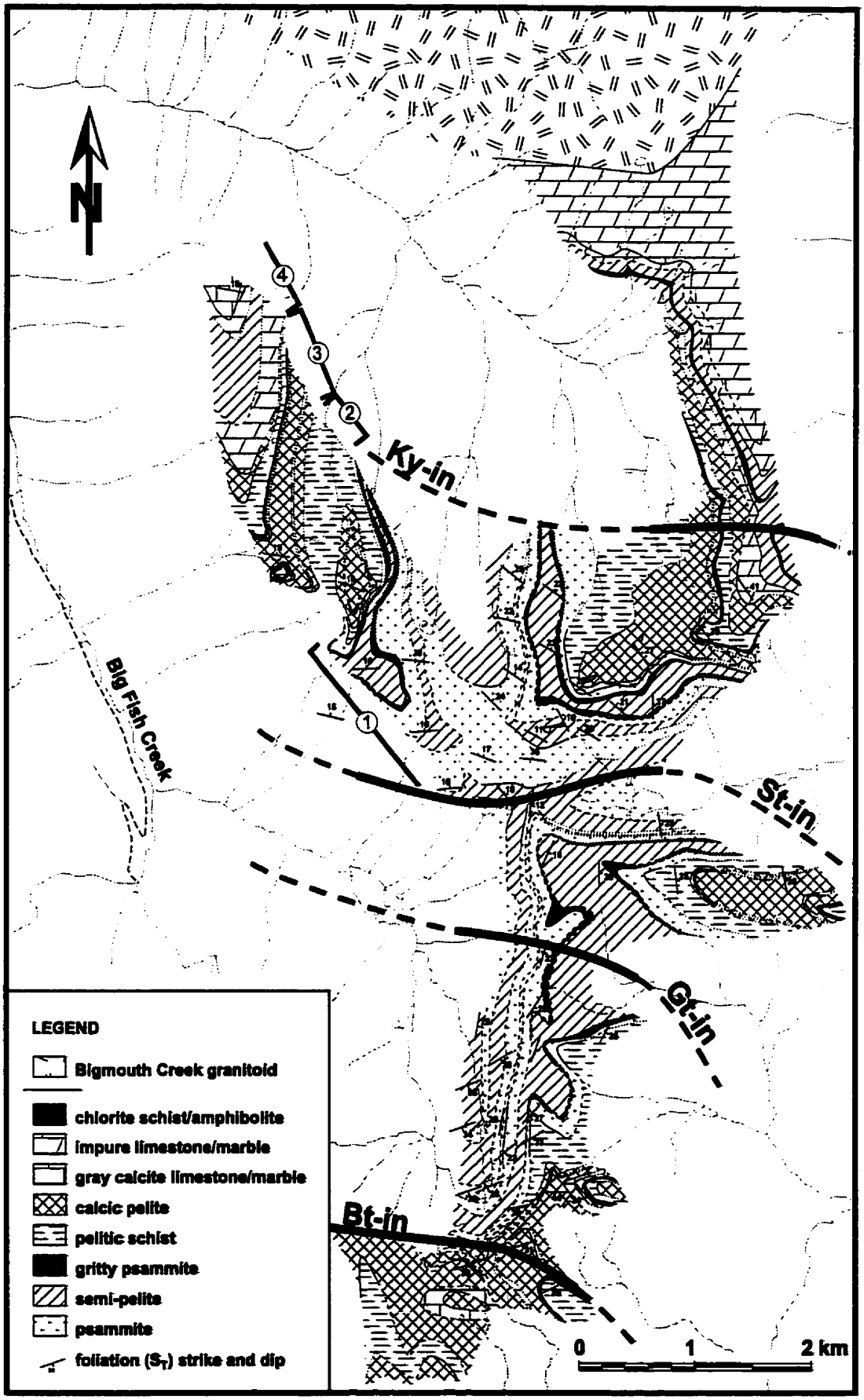

Figure 3.2 Lithologic map of the study area showing position of M2 mineral isograds. Stratigraphic intervals described in text are indicated by thick brackets.

3.2.3 Metamorphism

The previous chapter presents a detailed description of the distribution of metamorphic assemblages, the metamorphic reaction history, and an interpretation of the metamorphic evolution of rocks of the Big Fish Creek area. The salient points are summarized here.

An early metamorphic event, M1, is preserved as cores to composite, polycyclic garnet porphyroblasts in pelitic rocks. A later, medium-pressure prograde recrystallization event (M2) resulted in a sequence of metamorphic zones developed in rocks of pelitic composition, ranging from a chlorite zone in the south, to a kyanite + staurolite zone in the northern part of the Big Fish Creek area (Fig. 3.2). Extensive retrograde replacement of M1 assemblages preceded M2, indicating that the two metamorphic events were separated by an episode of cooling. Because of the extensive retrograde destruction of M1 assemblages prior to M2, the intensity and spatial distribution of prograde M1 recrystallization can not be accurately established. The M2 metamorphic overprint is well preserved. Andalusite is observed to overgrow M2 mineral assemblages in the north-central part of the area, and is inferred to represent decompression near or following the thermal peak of M2 metamorphism. Integration of these and other observations on the metamorphic history of the study area suggests that it was complex, polycyclic and protracted. The temporal and spatial relationships between deformation and metamorphic recrystallization are discussed in Section 3.4.2.1 below, where it is shown, based on textural criteria, that ductile deformation attended and outlasted prograde metamorphism in the area. In addition, there appears to be a close spatial and temporal correlation between intensity of metamorphism and style and intensity of deformation.

3.3 Structural geology

3.3.1 Previous work

The Big Fish Creek area lies on the southwest flank of the Selkirk Fan axis (SFA), a zone of structural divergence defined by a NW-trending axis separating rocks of southwest structural vergence to the southwest, from rocks of northeast structural vergence to the northeast (Fig. 3.1; Wheeler, 1963, 1965; Brown and Tippett, 1978). Since Wheeler's (1963, 1965) early work, a number of authors have described the structural geology and interpreted the deformational history of the Selkirk Fan in terms of discrete, spatially correlatable, deformation phases (e.g., Franzen, 1974; Van der Leeden, 1976; Tippett, 1976; Brown et al., 1977, 1986; Brown and Tippett, 1978; Read and Brown, 1979; Simony et al., 1980; Raeside

and Simony, 1982; Perkins, 1983). In this scheme, the overprinting of two generations of folds of opposite vergence (northeast and southwest) and of variable spatial intensity produces the structural fan (Brown and Tippett, 1978; Price, 1986; Brown et al., 1986).

A significant problem with this approach is that structures assigned to a given deformation phase based on similarity of style are known to be widely diachronous. For instance, on both flanks of the Selkirk Fan, D2, the second phase of deformation, is interpreted to pre-date, or be coeval with the main phase of metamorphic recrystallization (Van der Leeden, 1976; Brown and Tippett, 1978; Leatherbarrow, 1981; Simony et al., 1980; Perkins, 1983; Sevigny and Simony, 1989). However, this metamorphic event is thought to be of Jurassic age on the west flank of the SFA (Archibald et al., 1983; Brown et al., 1992a; Colpron et al., 1996), whereas on the east flank, it is interpreted to be of mid- to Late Cretaceous age (e.g., Sevigny et al., 1989, 1990).

Parrish (1995) integrated geochronological data for the Selkirk Allochthon and the underlying Monashee Complex and argued that metamorphism and associated deformation are progressively younger with structural depth, consistent with foreland-propagating deformation in the Selkirk Allochthon wedge. However, as described in the previous chapter and briefly summarized above, the history of prograde metamorphism and associated deformation in the study area is complex and probably spanned a substantial temporal range from mid-Jurassic to Cretaceous time. The relatively extensive record of metamorphism preserved in rocks of the Big Fish Creek area provides an excellent opportunity to address the question of the relative timing of different structural elements. The fact that they record at least two distinct prograde regional metamorphic pulses is atypical of rocks in nearby areas. This is either because later metamorphism in other areas was sufficiently intense to mask evidence of earlier metamorphism (e.g., Scammell, 1993; Crowley et al., 1998); or because these areas did not see as complex a metamorphic history and were only affected by one metamorphic event (e.g., Colpron et al., 1996). Whereas the mineralogical signature for polycyclic metamorphism may be cryptic, recent geochronological evidence suggests that high grade metamorphic rocks of the Selkirk Allochthon north and west of the present study area were, in fact, affected by at least two distinct thermal events during Mesozoic time (Sevigny et al., 1989; 1990; Scammell, 1993; Crowley et al., 1998).

As discussed at length below, many structural elements encountered in the study area were produced by progressive deformation and transposition over a significant period of time, as constrained by the syn-deformational metamorphic recrystallization history. This poses an additional problem when attempting the spatial correlation of structures based on style because similar structural elements may

have developed at widely different times (e.g., Williams and Zwart, 1977; Williams, 1985; Tobisch and Paterson, 1988, 1990). Furthermore, the diachronous nature of *both* deformation and metamorphism tempers the significance of temporal correlations of deformation and metamorphic events based on textural arguments. These problems are further addressed in the following sections.

3.3.2 Structural elements in the Big Fish Creek area

The structural grain of the Big Fish Creek area is controlled by the distribution of a moderate- to shallow-dipping penetrative foliation (Fig. 3.3A; see Appendix IV for listing of all field-based structural measurements). Closely associated with this foliation are tight to isoclinal folds, mineral and stretching lineations, extensional crenulation and shear bands. These early structures are associated with the main phase of deformation in this area. They are overprinted by at least two distinct sets of late crenulations. The following sections present a description of these different structural elements. Although no obvious structural discontinuity was encountered in the field, it will be argued that rocks of the study area represent part of a zone of intense distributed strain of probable regional significance. As discussed below, the dominant foliation is a transposition foliation developed during protracted non-coaxial deformation. In the following sections, distinction is made between structures formed prior to or during, and those formed after, the development of the transposition foliation.

3.3.2.1 Dominant foliation, S_T

The dominant outcrop-scale structural element in the Big Fish Creek area is a penetrative foliation defined by compositional layering and the alignment of minerals with grain-shape preferred orientations (e.g., Plate 8). Previous workers (Ghent et al., 1977; Simony et al., 1980; Raeside and Simony, 1983; Dechenes and Simony, 1984; Doucet et al., 1985; Sevigny and Simony, 1989) have ascribed the development of this foliation in areas in and around the Northern Selkirk Mountains to transposition resulting from superposition of two temporally distinct, but coaxial folding events and used an S_{1+2} notation to highlight its composite nature. In the Big Fish Creek area, the dominant foliation is locally discontinuous and is commonly observed to be axial planar to tight to isoclinal, commonly intrafolial, and locally refolded folds with attenuated to rootless limbs (Plates 8A, 9A). As discussed below, S_T is associated with intense and protracted deformation. For these reasons, it is interpreted to represent a transposition foliation because of its complex and composite nature (e.g., Plates 9A,D, 10; Tobisch and Paterson, 1988, 1990). Following Williams and Campagnoni (1983), it is referred to herein as S_T. Observations presented in this and the following sections further support this interpretation.

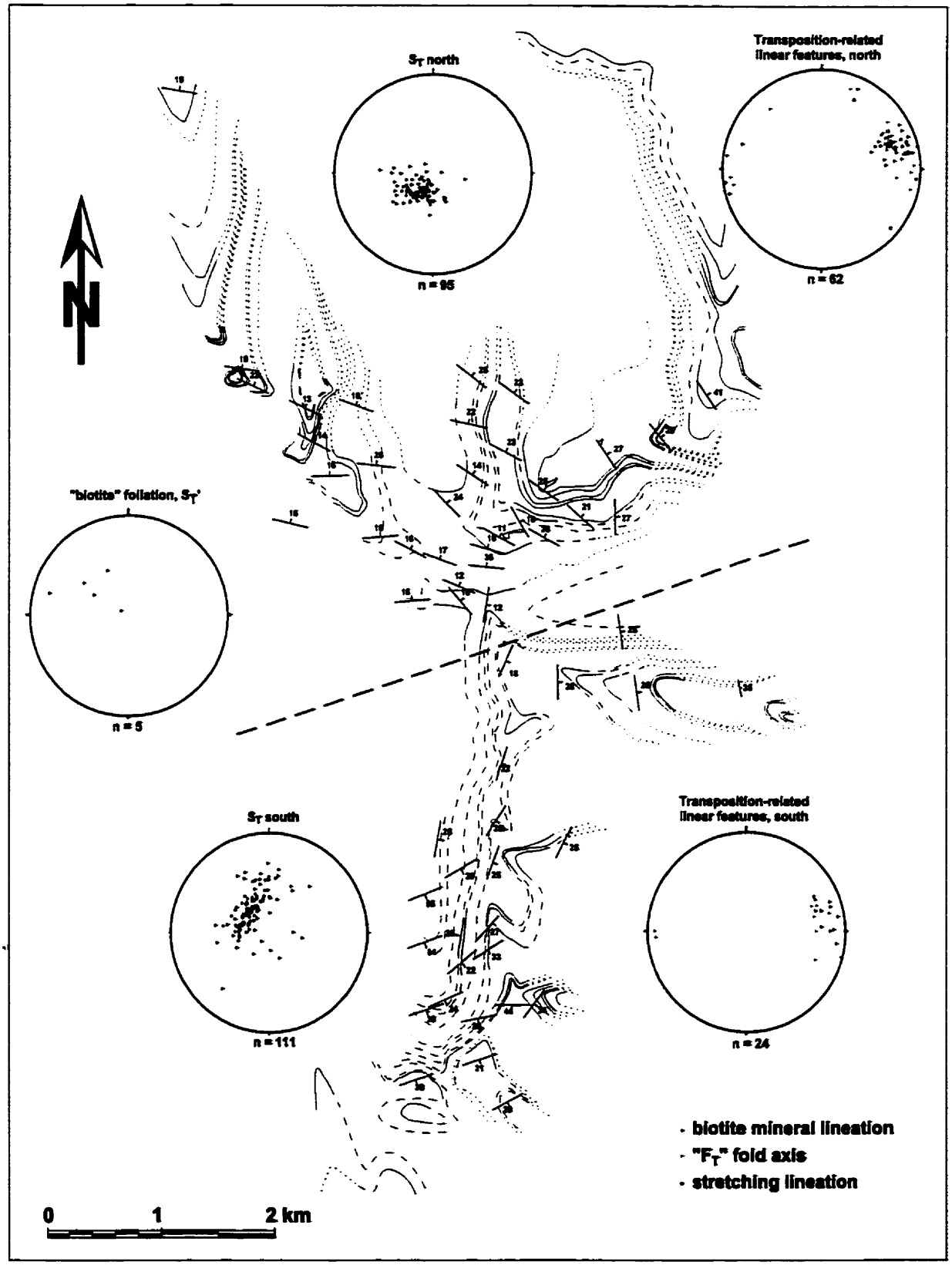

Figure 3.3A Attitudes of structural elements in the study area. Lithological contacts and distribution of ST attitudes are shown on map. Stereographic projection of transposition related structures: poles to ST and ST', FT, LT and stretching lineations.

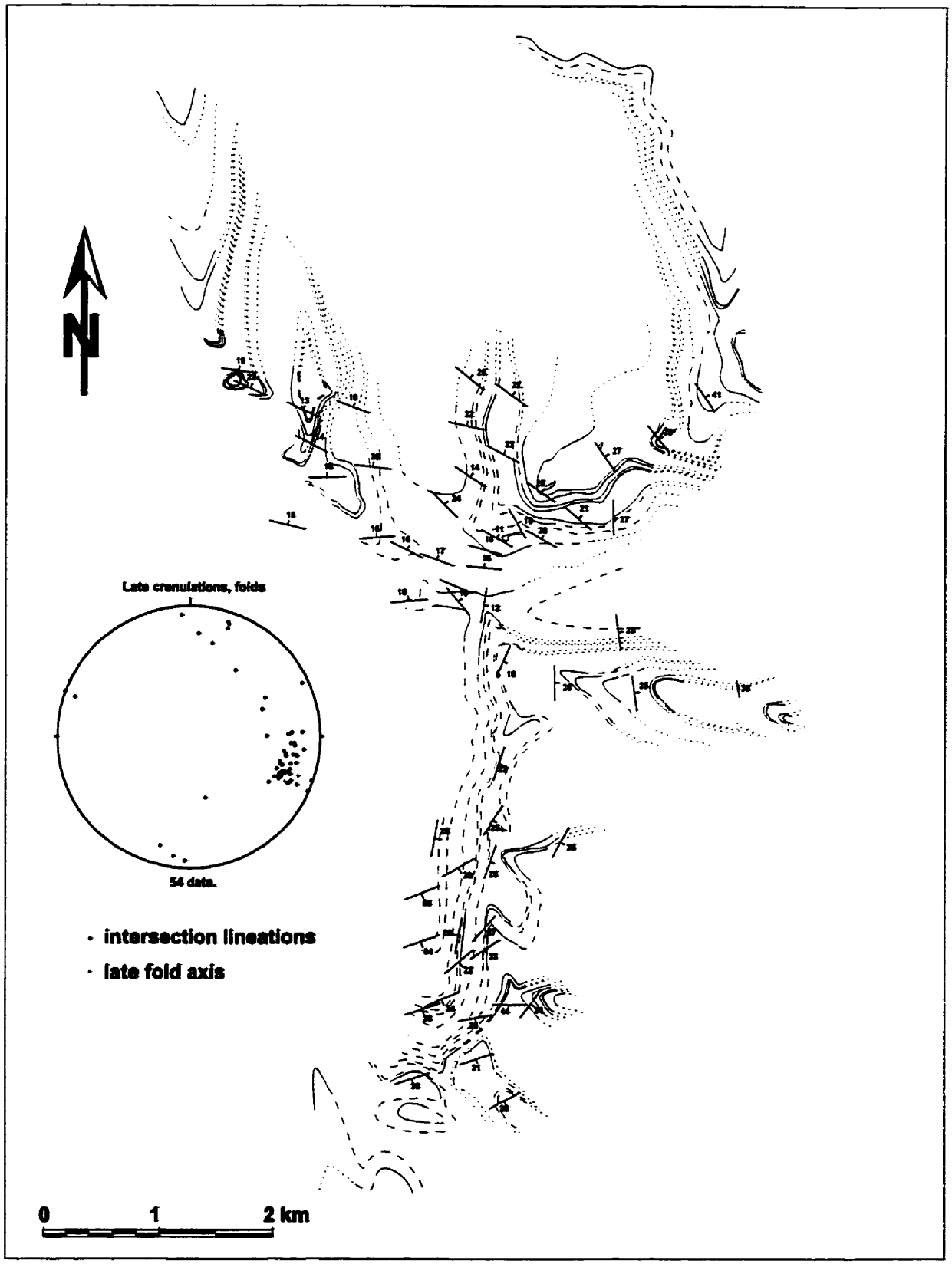

Figure 3.3B Attitudes of structural elements in the study area. Late structures: intersection lineations associated with late crenulations, and late fold axes.

Scammell (1993) reached similar conclusions regarding the nature of the dominant foliation in higher-metamorphic-grade rocks of the Monashee Mountains to the west (Fig. 3.1).

Measured attitudes of S_T are shown in Figure 3.3A. In general, the strike of S_T varies from northeasterly in the south to northwesterly in the north, and the dip is moderate to shallow (10-40°). This spatial variation defines a broad, markedly non-cylindrical, approximately upright antiform (Fig. 3.3A) which had been assigned to a regional third phase of folding by previous authors (e.g., Van der Leeden, 1976; Brown et al., 1977; Brown and Tippett, 1978). The antiformal trend is not regular: a relatively abrupt change in attitude of S_T is observed around the position of the M2 staurolite-in isograd (Figs. 3.2, 3.3A). North of this line, the attitude of S_T is much less variable than south of it.

As discussed below, S_T resulted from continued transposition of a variety of fabric elements as a result of protracted and intense general shear. These fabric elements, which comprise tight to isoclinal asymmetric shear folds and associated axial planar foliation (S_T', preferred alignment of platy minerals, crenulation, and crenulation cleavage), as well as extensional shear bands (or S-C'-type fabric), developed at different stages of superimposed cycles of transposition of S_T as illustrated schematically in Figure 3.4.

In thin section, the dominant foliation is typically highlighted by the preferred orientation of platy minerals, and compositional layering (Plates 10, 11C,D). It is commonly irregular to anastomosing, and forms an S-C'-type fabric where anastomosing segments show continuity across the main trend of the foliation, or where discrete shear bands are developed (Plates 9D, 11C,D, 12C). Often, a folded pre-existing foliation is preserved in microlithons bounded by laminae defining a later foliation (Plate 10). The degree of overprinting of the earlier foliation by the later foliation is variable, the later foliation varying in style from gentle crenulation (Plate 10A,B) to well-developed crenulation cleavage, to essentially completely transposed foliation (e.g., Plate 10C,D; c.f., Bell and Rubenach, 1983; Tobisch and Paterson, 1988, 1990). The co-planarity, at the scale of the outcrop and larger, of the dominant foliation in rocks which show different stages of the transposition cycles at the fine scale indicates that strain involved continued rotation of newly formed foliations towards a plane parallel to the dominant foliation (Tobisch and Paterson, 1988), which is interpreted to parallel the local shear plane (e.g., Williams 1983). These observations highlight the spatially heterogeneous nature of finite strain resulting from progressive deformation. Tobisch and Paterson (1988) found similar features to those described above in rocks from a ductile shear zone in the Lachlan Fold Belt and interpreted them to be the result of spatially heterogeneous development of overprinting transposition cycles during progressive deformation. These authors described the complex nature of such foliations in terms of consecutive cycles of evolving

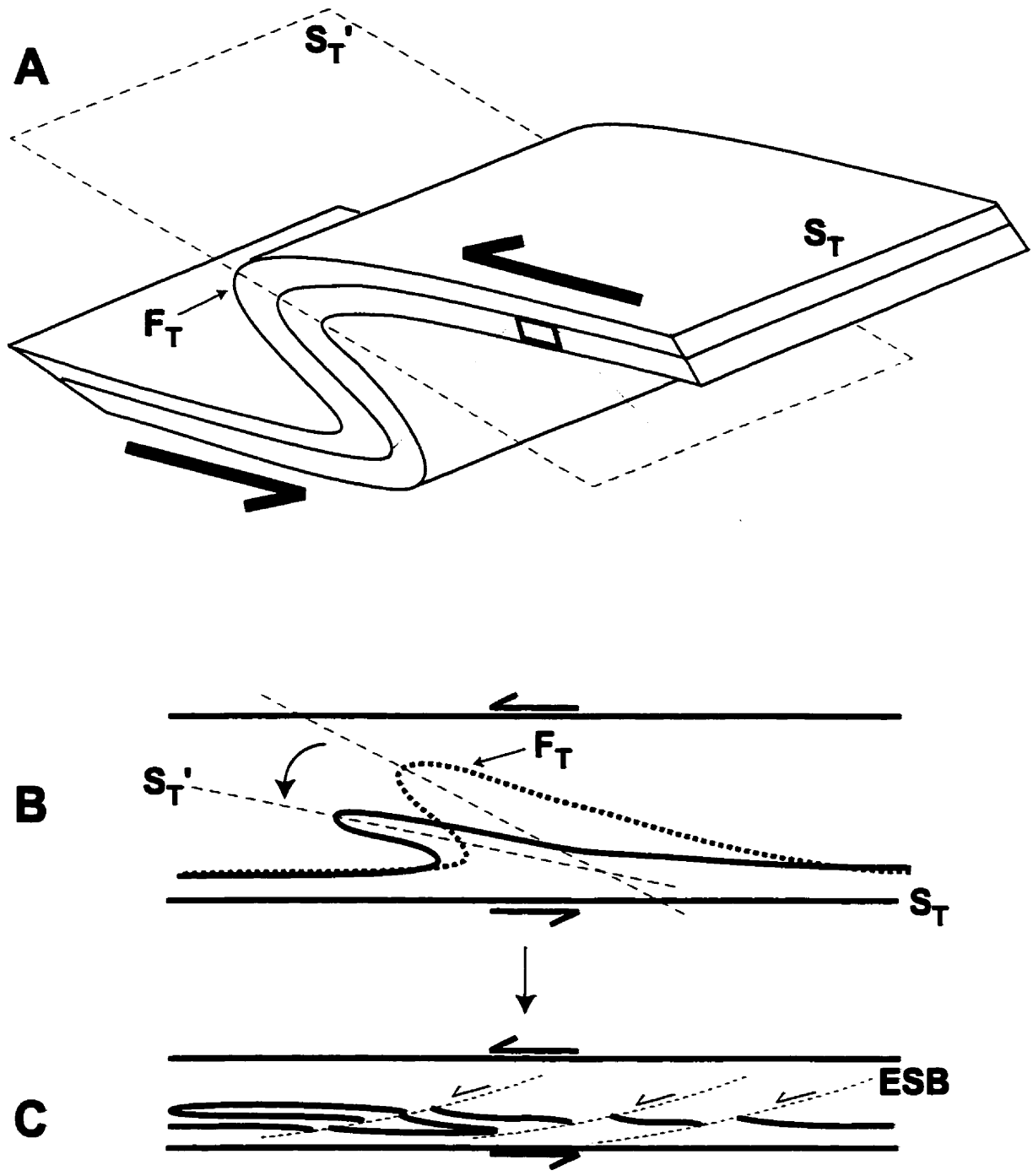

Figure 3.4 Schematic representation of cyclical transposition and interpreted relationship between S_T, S_T', FT_T, and extensional shear bands. A: General overview of geometry. The structural elements are developing in a macroscopic shear fold. B: Small F_T shear folds develop as a result of localized inhomogeneous shear at different scales. S_T' is axial planar foliation to F_T. With continued shear, F_T tightens and its axial plane, as recorded by S_T', rotates towards the "regional" foliation, S_T. C: With continued shear and rotation, S_T' approaches S_T and continued rotation is precluded. Continued shear is accommodated by development and motion along extensional shear bands (ESB), unless or until a new F_T forms and a new cycle of transposition is initiated.

foliation from an early continuous cleavage (S_c) to different degrees of crenulation of this cleavage to produce a later crenulation or crenulation cleavage (S_{cr}, S_{cc}). They also demonstrated the spatial heterogeneity of evolution through such cycles, as a result of strain partitioning over areas as small as a thin section. The above nomenclature is adopted here to describe components of the composite transposition foliation, S_T (Plates 9D, 10).

Inclusion trails in porphyroblasts (S_i) show variable angular relationship with respect to the external matrix foliation (S_e; Plates 9D, 12, 13A,B). S_i in biotite (e.g., Plate 12) is usually more strongly rotated with respect to S_e than is S_i in other porphyroblastic minerals (e.g., Plates 9C,D, 13A), although the extent of rotation of S_i in biotite is commonly irregular at the scale of a thin section (Plate 11C). Locally, S_i reflects different stages of the transposition cycle than those recorded by S_e (Plate 9D; also see Plate 1A,B). This indicates that the relative timing of development of the dominant foliation with respect to the growth of metamorphic minerals is spatially heterogeneous (see Section 3.4.2.1 and previous chapter). As the prograde growth of metamorphic minerals was probably more or less synchronous, this implies that deformation was diachronous and heterogeneous at the scale of the thin section. This diachroneity and spatial heterogeneity of the deformation are further evidence of transposition due to progressive deformation (Williams, 1967, 1985; Hobbs et al., 1976; Tobisch and Paterson, 1988; Mawer and Williams, 1991).

In the more intensely metamorphosed rocks in the northern part of the study area, compositional layering (which defines S_T in part) is commonly characterized by mm- to cm-thick biotite-rich laminae interlayered with quartz-rich laminae (e.g., Plates 9A, 14A). In particular, rocks which bear evidence of intense strain usually show extensive differentiation of biotite-rich and quartz-rich laminae (Plate 14A). These observations suggest that progressive deformation associated with the development of S_T involved dissolution and fluid-aided material remobilization (e.g., Williams, 1972).

3.3.2.2 "F_T", tight to isoclinal folds associated with S_T

As previously noted, S_T is axial planar to tight to isoclinal, intrafolial folds developed at different scales (Plates 8A, 9A, 15). Intrafolial isoclinal folds of concordant quartz veins are particularly abundant (Plate 15). These folds generally have strongly attenuated to discontinuous limbs (Plates 9A, 15C), and in places, are seen to be intrafolially refolded (Plate 9A). Given the progressive nature of the deformation associated with these folds and their axial planar foliation, S_T, it is likely that stylistically similar folds in these rocks did not all form at the same time (Park, 1969; Roberts, 1977; Williams and Zwart, 1977;

Williams and Campagnoni, 1983; Williams, 1985; Tobisch and Paterson, 1988, 1990; Mawer and Williams, 1991). For this reason, and because they are associated with S_T, these folds are referred to herein as "F_T". Generally, F_T folds plunge gently ENE to WSW, but some dispersion is observed (Fig. 3.3A).

Most F_T axes are sub-parallel to mineral and stretching lineations (Fig. 3.3A). Folds with axes parallel to stretching lineations are common in compressional orogenic settings (e.g., King and Rast, 1956; Bryant and Reed, 1969; Olesen and Sørensen, 1972; Borradaile, 1972; Hobbs et al., 1976; Williams and Zwart, 1977; Williams and Campagnoni, 1983; Holdsworth, 1989; Alsop and Holdsworth, 1993; Alsop et al., 1996, 1998). They are often interpreted as resulting from progressive rotation of folds initially at high angle to the stretching lineation by continued deformation (e.g., Bryant and Reed, 1969; Borradaile, 1972; Sanderson, 1973; Escher and Watterson, 1974; Williams and Campagnoni, 1983; Holdsworth, 1989). In this scheme, dispersion in fold axis orientation is either due to irregular initial orientations, or to continued fold generation during axis rotation (Borradaile, 1972; Sanderson, 1973; Escher and Watterson, 1974; Ramsay, 1979). However, other mechanisms have been proposed whereby folds may form with axes initially close to the main transport direction (or stretching lineation; e.g., Butler, 1982; Rattey and Sanderson, 1982; Coward and Potts, 1983; Northrup and Burchfield, 1996; Grujic and Mancktelow, 1995). Rattey and Sanderson (1982) and Coward and Potts (1983) suggested that orogen-transverse folds may form at the lateral tips of thrust sheets as a result of differential orogen-transverse movement, and Butler (1982) documents orogen-transverse folds in lateral ramps to structural horses formed as a result of impingement by a laterally adjacent, younger horse. On the other hand, Northrup and Burchfield (1996) interpret orogen-transverse folds to result from orogen-parallel flow due to vertical strain partitioning in a transpressional setting. In all of these cases, orogen-transverse folds would be expected to show a preferred sense of vergence (e.g., Rattey and Sanderson, 1982). In contrast, rotation of folds with axes initially perpendicular to the transport direction into transport-parallel orientation by passive rotation during continued shear should result in a more or less symmetric distribution of fold vergence (cf. Coward and Potts, 1983).

A few rare northwest-southeast trending (i.e., orogen-parallel), tight to isoclinal folds were encountered in the study area (Plate 8B), usually folding impure limestone layers. These folds are typically west-vergent (Plate 8B) and have been interpreted by previous workers to be related to early, west-vergent, regional recumbent folds on the western flank of the Selkirk Fan structure (e.g., Raeside and Simony, 1983; Brown and Lane, 1988; Colpron et al., 1998). No definite occurrence were encountered of non-cylindrical fold with sheath-like geometry, which would be expected if axis rotation

produced the transport-parallel fold axes and the observed dispersion in hinge orientations (Cobbold and Quinquis, 1980; Coward and Potts, 1983).

3.3.2.3 Mineral/intersection lineation, L_T and transient foliation, S_T'

In upper biotite- and higher grade rocks of the study area, cigar- (prolate) to elongate penny-shaped (oblate) biotite porphyroblasts are widespread. The long axis of these biotite grains typically have a preferred orientation which defines a distinct mineral lineation on S_T-parallel surfaces (Plate 9B). Where oblate biotite grains dominate, the lineation is defined by the intersection of those grains with S_T (Plate 11). Whereas in many cases the platy grains do not show a preferred orientation about the axis of elongation (Plate 11C), in a number of instances, a preferred orientation was observed, defining a distinct foliation (Plate 11B). This foliation is variably developed at the scale of the outcrop, and is generally discontinuous from layer to layer. A schematic representation of the observed attitudes of lineation-defining biotite is shown in Figure 3.5. Because the mineral/intersection lineation formed during progressive deformation associated with transposition (see below), it is referred to as L_T. Similarly, the foliation defined by aligned platy biotite porphyroblasts represents a transient stage of a transposition cycle involved in progressive S_T development (Tobisch and Paterson 1988, 1990), and is labeled S_T'.

Macroscopically, L_T lineations plunge gently ENE to WSW (Fig. 3.3A). As mentioned in the previous section, L_T and stretching lineations, as well as most F_T fold axes show sub-parallel orientations (Plates 9B, 15B). In the several instances where a well-defined S_T' was observed, it dipped consistently to the southeast (i.e., NW-vergence; Fig. 3.3A).

In thin section, biotite porphyroblasts are cigar- to fish-shaped, and typically asymmetric (Plates 10, 12). Inclusion trail foliation in biotite porphyroblasts (S_i) is typically continuous with, but inclined relative to S_e (e.g., Plates 10A,B, 12). The angle between S_i and S_e usually varies from grain to grain (Plates 10A,B, 11C, 12C,D; also see Plate 3D) suggesting that the extent of relative rotation of different biotite porphyroblasts with respect to S_e was heterogeneous. Some randomly oriented flakes have S_i parallel to S_e indicating that they did not rotate relative to S_e; these grains are generally blocky and do not show strong asymmetry (Plate 11C). In cuts normal to both S_T and the mineral lineation, there is generally a preferred sense of rotation of the porphyroblasts, as indicated by the angle between S_e and S_i and by the asymmetry of fish-shaped grains (e.g., Plates 10C,D, 11C; Lister and Snoke, 1984), although within the same section, some flakes may show opposing sense of rotation or vergence with respect to S_T (Plates 11C,D, 12A,B,D). In sections normal to S_T and parallel to L_T, long axes of porphyroblasts are

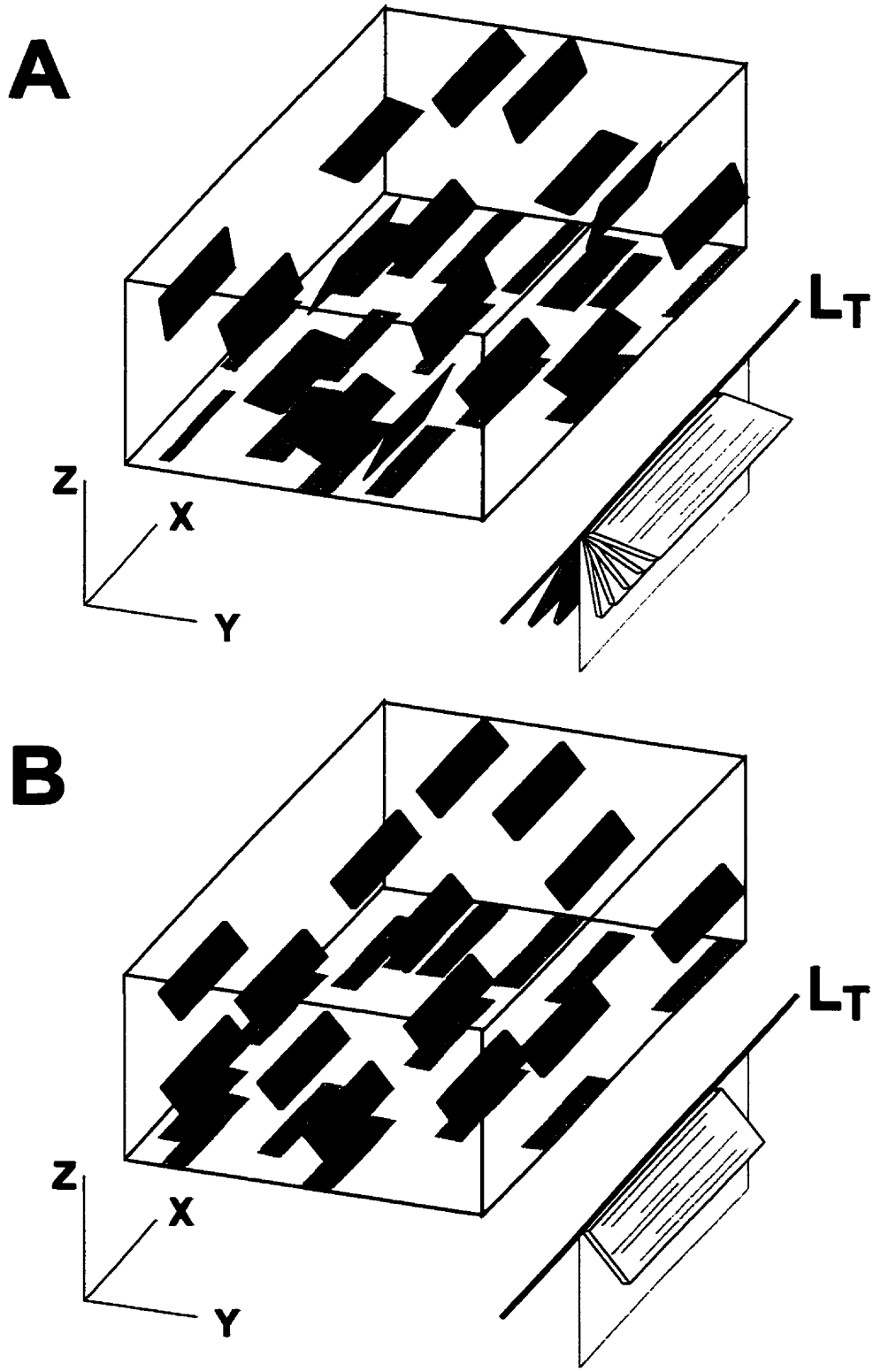

Figure 3.5 Schematic representation of the attitude of lineation-defining biotite porphyroblasts S_T is parallel to top surface of block. A: Biotite flakes are irregularly fanned about an axis parallel to L_T. Although there is a dominant sense of vergence with respect to S_T, both senses of vergence are encountered. B: Biotite flakes show co-planarity, defining a foliation, S_T'. The intersection of this foliation with S_T is L_T.

generally sub-parallel to S_T (Fig. 3.5A) although some asymmetry is also usually still preserved, and S_i, where observed, is at high angle to S_e, indicating significant rotation of the grains (Plates 10C, 11D). Where the sense of rotation can be determined, it is mostly consistent from grain to grain, although grains showing opposite sense of rotation are also encountered in L_T-parallel sections (Plate 12A).

These observations lend insight into the formation of the L_T lineation. Blocky biotite porphyroblasts which grew at high angle to S_T (e.g., Plate 11C) were progressively rotated towards parallelism with it. These grains were also affected by crystal plastic deformation: their common asymmetric fish-shape habit (e.g., Plates 10, 11C,D, 12; e.g., Lister and Snoke, 1984) may have resulted from slip along basal cleavage planes; in other cases, deformation bands are observed in biotite porphyroblasts (Plate 12B). Hence, development of the biotite lineation in rocks of the study area involved non-coaxial internal strain, and rigid-body rotation, as illustrated schematically in Figure 3.6. Where rotation was complete, the biotite grains lie sub-parallel to S_T. A mineral lineation (L_T) is visible on S_T surfaces because the grains have been strained and rotated until their long axes are parallel to the maximum stretching direction (Fig. 3.6C). In some cases, large biotite flakes have their long axis parallel to, and are bounded by a crenulation foliation developed during the early to intermediate stages of a transposition cycle (Plate 10A,B; Tobisch and Paterson, 1988), and this may explain the preferred sense of vergence of biotite flakes observed in some rocks: these biotite grains may have grown with a preferred orientation parallel to the transient crenulation cleaveage. In other cases, however, large biotite flakes appear to have grown in more or less random orientation with respect to S_T or associated foliations developed during transposition (e.g., Plate 11C). The fanning of biotite porphyroblasts, and of other matrix minerals with shape-preferred orientation, about an axis parallel to the direction of L_T (Plates 10A,B, 11, 12; Fig. 3.5) is interpreted to indicate continued growth and rotation of newly formed biotite grains during progressive deformation and this is supported by S_e-S_i relationships. The presence of late, undeformed and unrotated biotite co-existing with extensively rotated and deformed biotite (e.g., Plate 11C) suggests that locally at least, biotite growth outlasted progressive deformation associated with L_T development.

The fish-like morphology of biotite flakes and their rotation towards parallelism with S_T suggest that extensional strain was associated with the development of the biotite mineral lineation (e.g., Lister and Snoke, 1984). As discussed below, biotite "fish" are commonly associated with occurrences of extensional crenulation or shear bands (Platt and Vissers, 1980) in the study area (see Section 3.3.2.6 below), which reinforces this conclusion. The asymmetry and vergence of fish-shaped micas can be used to infer the sense of non-coaxial shear in these rocks during development of the mineral lineation (Lister

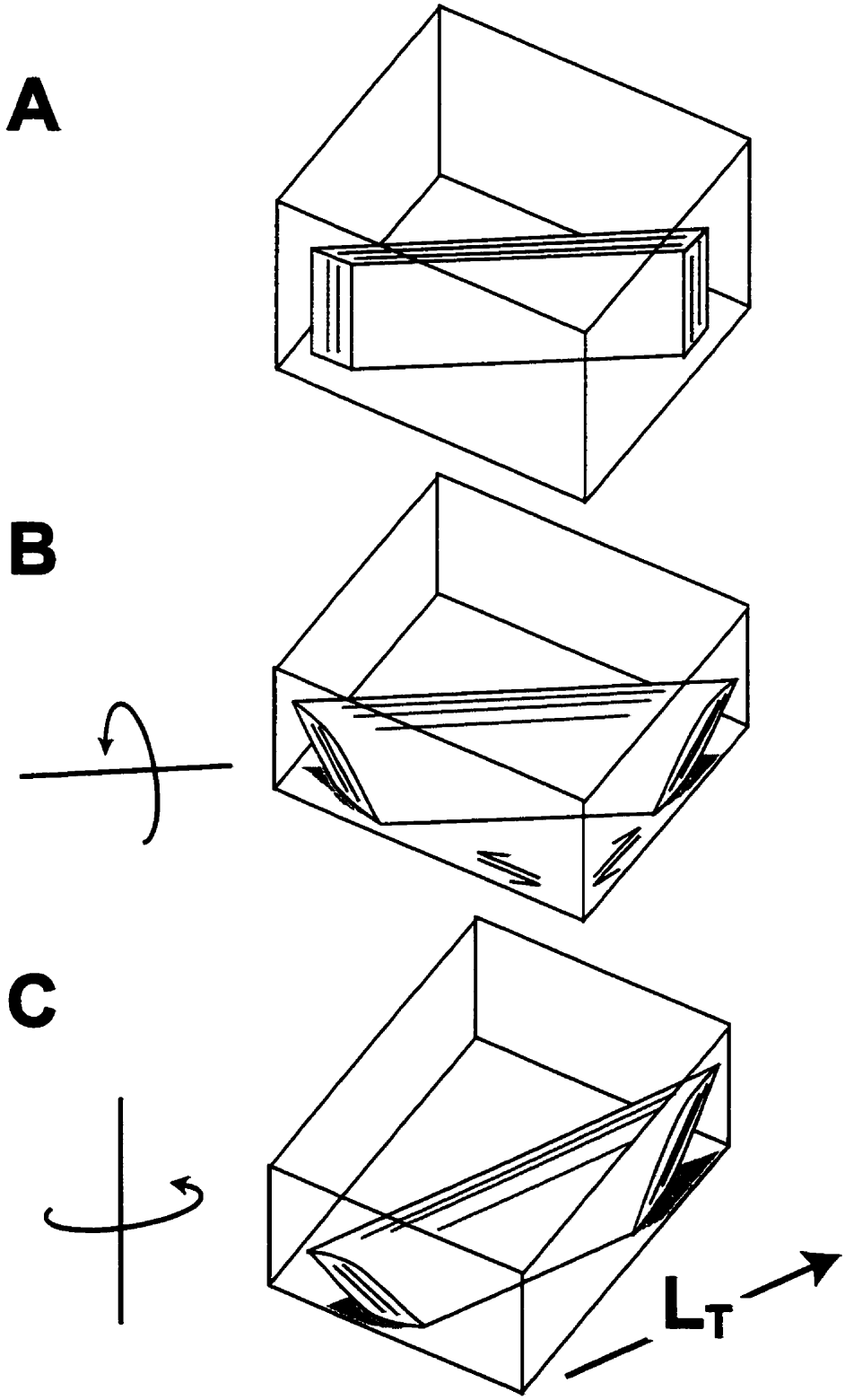

Figure 3.6 Schematic representation of deformation of lineation-defining biotite flakes; S_T plane is parallel to the top of the block diagram. A: Initially undeformed and randomly oriented flake. B: Rotation towards the S_T (flattening) plane and plastic deformation of the flake to produce fish shape. C: Rotation towards parallelism with L_T lineation and plastic deformation. The sequence does not represent a time series, as rotation towards S_T and L_T are probably in part at least synchronous.

and Snoke, 1984). On the other hand, the common occurrence of biotite flakes showing opposite senses of rotation within the same sample (Plates 12A,B,D) indicates that deformation related to the development of the biotite lineation involved a pure shear component normal to S_T (i.e., flattening; Platt and Vissers, 1980).

3.3.2.4 Stretching lineation in quartzo-feldspathic rocks

A stretching lineation is commonly developed in mica-poor quartzo-feldspathic rocks of biotite- and higher metamorphic grade in the study area, as recrystallized ribbon quartz and stretched feldspar clasts with high aspect ratios (Plate 16), which locally constitutes the dominant structural element of the rock. This stretching lineation generally plunges ENE to WSW and the majority of the stretching lineations measured show parallelism with F_T fold axes and L_T lineations (Fig. 3.3A).

In thin sections, strained psammite from the M2 staurolite zone is characterized by coarse quartz grains with local polygonal outline, and ribbons of large elongate quartz grains separated by high angle grain boundaries which are approximately orthogonal to S_T (Plate 16B). Generally, these grains do not show a preferred crystallographic orientation. These textures are interpreted to represent recrystallization of quartz under conditions of low strain rate (static) or high temperature, or both. Commonly, these grains have lobate and sutured outlines, and preserve evidence of crystal plastic strain (deformation lamellae, sub-grain boundaries) and strings of fine grains are developed at grain boundaries, indicating substantial subsequent dynamic recrystallization (Plate 16B). Feldspar porphyroclasts commonly have a high density of sub-grain boundaries and dynamically recrystallized grains at grain boundaries; fine, dynamically recrystallized grains form long, lineation-parallel strings (Plate 16). These textures indicate that strain involved crystal plastic deformation of both quartz and feldspar. Crystal plasticity in feldspar suggests deformation at temperatures characteristic of middle to upper amphibolite conditions (e.g., Tullis and Yund, 1987). This indicates that at least some of the deformation resulting in the stretching lineation was active at or near metamorphic peak conditions in the area. This, and the parallelism of the stretching lineation with the mineral/intersection lineation indicates that the stretching lineation is also the result of the progressive deformation which produced the transposition-related structures described in the previous sections. Locally, stretched feldspars are boudinaged into angular fragments with intervening gaps at high angle to the dominant foliations (Plates 13D, 14D), suggesting that extensional deformation of feldspar probably continued during cooling from metamorphic peak conditions.

3.3.2.5 Fractured porphyroblasts and porphyroclasts

Split or fractured porphyroblasts are commonly observed in rocks at or above garnet grade. Fractured garnet porphyroblasts are abundant, occurring in the majority of garnet-grade and higher garnet-bearing rocks (see Appendix II for occurrences of split garnet in hand samples and outcrops). Split and/or fractured garnet porphyroblasts are recognizable in the field (Plate 9A,B); split or fractured porphyroblasts of biotite (Plates 12C, 13A), staurolite (Plate 13B), kyanite, and andalusite (Plate 13C) were also identified in thin section. In general, gaps or fractures are at high angle to S_T (Plates 9, 13). In the field, the gaps generally trend N-S, and dip steeply, a trend approximately perpendicular to lineations and F_T fold axes (e.g., Plate 9B). Different co-existing minerals commonly show a similar orientation of gaps or fractures (e.g., Plate 13A) and, except for biotite (see previous section), have not been substantially rotated following splitting or fracturing (Plates 9A,B,C). This suggests that porphyroblast splitting primarily represents a coaxial process (i.e., splits are tensional fractures).

A retrograde aggregate consisting of chlorite + quartz + muscovite ± biotite ± plagioclase is commonly developed in gaps of split garnet porphyroblasts (see Plate 1B, previous chapter) and of muscovite ± chlorite ● biotite in gaps of split staurolite (Plate 13B) suggesting that hydration during retrogression may have facilitated splitting. In many cases, syn- or post-splitting relative displacement of grain fragments seems to have taken place (e.g., Plate 9C; also see Plate 1B). As discussed at length in the previous chapter, early (M1) garnet porphyroblasts were split prior to, or during a cooling and retrogression event which resulted in the growth of retrograde assemblages in the gaps between split fragments (Plate 1B). This retrogression event was followed by M2 prograde recrystallization, during which porphyroblasts developed which were subsequently split (e.g., M2 staurolite and kyanite, and andalusite, Plate 13B,C). This implies that the strain regime responsible for the development of fractures and splits at high angle to S_T was active, episodically at least, from prior to the high-pressure peak of M2 until after late-M2 decompression which resulted in crystallization of andalusite.

As discussed in the previous section, boudinaged feldspar porphyroclasts were also observed in strongly lineated psammitic rocks (Plates 13D, 14D).

3.3.2.6 Extensional crenulation and shear bands

Mesoscopic extensional shear bands and extensional crenulations (e.g., Berthé et al., 1979; Platt and Vissers, 1980; Lister and Snoke, 1984) are relatively common in rocks of the study area (Plate 14).

At the hand sample and microscopic scale, these surfaces are outlined by gentle, approximately symmetric to gently asymmetric microfolds of the dominant foliation with which they merge and anastomose, commonly producing an S-C' fabric (Platt and Vissers, 1980; Lister and Snoke, 1989; Twiss and Moores, 1992, p. 273; Plates 11C, 12C, 14B). Shear bands and extensional crenulation cleavages are commonly closely associated with lineation-defining biotite porphyroblasts (e.g., Plates 11C, 12C). In many cases, strain partitioning resulting from the presence of porphyroblasts (e.g., Lister and Williams, 1983; Bell, 1985) appears to have favored the development of extensional crenulations or shear bands (e.g., Plate 12C,D). As with biotite porphyroblasts, extensional crenulation cleavage or shear bands appear to have undergone variable extents of rotation towards parallelism with S_T (the shear plane; e.g., Tobisch and Paterson, 1988), and the angle between these surfaces and S_T is usually lower in L_T-parallel than in L_T-normal cuts (Plate 11C,D). Similar features were interpreted by Tobisch and Paterson (1988) as recording overprinting of different generations of foliations (e.g., layering, crenulation, crenulation cleavage, etc.) during progressive deformation. The fact that extensional shear bands and crenulation cleavage are visible in both L_T-parallel and L_T-normal cuts perpendicular to S_T (Plates 11C,D, 14C) indicates that deformation involved a component of coaxial shear during development of these structures (i.e., shortening perpendicular to S_T). Insufficient observations are available to determine whether extensional shear bands systematically show a preferred sense of vergence. However, some notable mesoscopic shear bands in strongly sheared rocks appear to record orogen-parallel, top-to-the northwest displacement in the later stages of ductile progressive deformation (Plate 14A).

3.3.2.7 Southeast-trending crenulation and related folds

Locally very intense crenulation of S_T and earlier foliations has resulted in the development of a WNW-striking foliation which dips steeply to the northeast and generally intersects S_T at high angle (Plate 8C). Intersection of this foliation with S_T produces a gently ESE-plunging lineation which is locally very strong (Plate 8D; Fig. 3.3B). This crenulation foliation is axial planar to upright, generally open mesoscopic folds of S_T (Plate 8C). The extent of overprint of S_T by this foliation is very uneven. Its development is much more advanced in mica-rich rocks, and in general, low-metamorphic grade rocks in the southern part of the study area appears to be more strongly affected than high-grade rocks in the north. This crenulation has been interpreted to be related to large-scale, late NW- to WNW-trending folds of which the broad antiform defined by S_T in the study area (Fig. 3.3) would be an example (Van der Leeden, 1976; Brown et al., 1977; Brown and Tippet, 1978). However, an alternative interpretation for the variable attitude of S_T at the scale of the study area is discussed in Section 3.4.1 below.

3.3.2.8 Northeast-trending crenulation

Locally, a crenulation intersection lineation is observed on S_T surfaces at high angle to the ESE-trending crenulation lineation (Fig. 3.3B; Plate 8D). No foliation related to this crenulation lineation was measured, nor were any related folds observed, but Van der Leeden (1976; his D_5 structures) observed the same lineations and associated steep, NNE-striking, west-dipping crenulation foliation, which is axial planar to NNE-trending folds. Relative timing of the two crenulation foliations is difficult to establish and appears to vary from instance to instance. Van der Leeden (1976) interpreted them to be contemporaneous and to constitute a conjugate set, akin and of similar orientations to conjugate foliations reported by Simony and Wind (1970) for the Dogtooth range, to the southeast (also see Murphy and Journeay, 1982).

3.4 Discussion

The bulk of the field and petrographic observations presented above suggests that rocks in the study area record intense, albeit spatially heterogeneous strain resulting from protracted progressive deformation attended by a complex history of metamorphic recrystallization. High-metamorphic-grade rocks in the northern part of the study area in particular, appear to be the locus of a zone of pervasively intense deformation and transposition, which arguably constitutes a regionally significant shear zone. As discussed below, strain was non-plane, at least episodically, comprising an important component of shortening perpendicular to the dominant, shallow-dipping regional foliation, S_T, accommodated at least in part by orogen-parallel extension. The latter part of this discussion presents a tectonic model in which the observed strain features are explained by mechanisms of syn-contraction gravitational spreading ("dynamic spreading"; e.g., Holdsworth and Grant, 1990) of a thrust package during Mesozoic convergence of western North America with accreted terranes to the west.

3.4.1 Intensity of deformation

The dominant structural feature of the study area is S_T, the transposition foliation. Development of S_T resulted from continued cyclical development and rotation of fabric elements (crenulation cleavage, cleavage-parallel mica flakes, extensional shear bands, etc.) towards the local shear plane (e.g., Fig. 3.4; Tobisch and Paterson, 1988, 1990; Mawer and Williams, 1991), which S_T is interpreted to parallel. Evidence for progressive rotation of fabric elements towards a regionally consistent S_T is pervasive, indicating that this also represents a regional shear plane (e.g., Escher and Watterson, 1974; Williams,

1983, Mawer and Williams, 1991). Hence, the progressive and cyclical nature of S_T-related transposition is interpreted to approximate a steady-state process (Means, 1981; Williams, 1983). Although this implies that estimating finite strain precisely is impossible, the achievement of a steady-state foliation itself requires that rocks in the study area were affected by intense strain comprising an important non-coaxial component (Means, 1981).

Other evidence for high strain in these rocks includes the widespread, albeit heterogeneous occurrence of a number of fabrics usually associated with intense deformation. Although mesoscopic evidence for high strain does include local occurrences of rocks characterized by a mylonitic foliation parallel, or at low angle to layering, and defined in part by regular, shear-induced compositional segregations (Plate 14A) and/or a strong stretching lineation (L-tectonite; Plate 16), most of the features indicative of high strain are more subdued, and suggest distributed, pervasively intense strain at different scales. Some of these features are mesoscopic: isoclinal, locally refolded intrafolial folds with attenuated to sheared-out limbs with axial plane parallel to the dominant foliation (Plates 8A, 9A; e.g., Williams, 1967; Williams and Zwart, 1977; Mawer and Williams, 1991); fold axes parallel to the stretching lineation (Plates 8A, 15B; e.g., Roberts and Sanderson, 1974; Escher and Watterson, 1974; Passchier, 1986; Mawer and Williams, 1991); cross- and anastomosing layering and related extensional shear bands (e.g., Plates 11C, 12, 14A,C; Hobbs, 1965).

In addition to evidence for cyclical development of S_T, and co-planarity of S_T with the regional plane of non-coaxial shear, a number of fabric elements supportive of intense strain are widespread at the hand-sample to microscopic scale. These include obliqueness of newly-crystallized micas with respect to the mesoscopic dominant foliation (e.g., Plates 11, 12; Passchier, 1986; Mawer and Williams, 1991); anastomosing foliation (Plates 10C,D, 11C,D, 12A,C; Platt and Vissers, 1980; Lister and Snoke, 1984; Passchier, 1986); extensional crenulations, or extensional shear bands, which in many cases produce an S-C' fabric (Plates 11C, 12C, 14B,C; e.g., Platt and Vissers, 1980; Lister and Snoke, 1984; Hanmer and Passchier, 1991); fish-shaped micas (Plates 10C,D, 11, 12; e.g., Lister and Snoke, 1984); fragmented rigid elements (Plates 9, 13, 14D; e.g., Ramsay and Sturt, 1970; Simpson and Schmid, 1983); pressure shadows around rigid grains (Plates 12C, 13A; e.g., Simpson and Schmid, 1983); delta- and/or sigma-type rigid porphyroclasts (Plate 14D). All these features seem to confirm the interpretation that the study area is a zone of intense distributed ductile strain at all scales.

Although the high-strain features just mentioned occur throughout the study area, the extent to which they are developed is spatially variable. The M2-staurolite isograd in the study area approximately

coincides with a relatively sharp gradient in the pervasiveness of the different fabric elements; north of the isogradic surface (Figs. 3.2, 3.3A), rocks show much more consistent co-planarity of fabrics at the hand-sample to microscopic scale than they do south of it. Although high strain features (see above) do occur south of this surface, they are less pervasively developed, suggesting that strain intensity was generally lower than in rocks to the north. The more irregular attitude of foliation elements in the south also indicates that S_T-normal shortening was less important than in the north. The macroscopic distribution of S_T attitudes is also consistent with this interpretation. Upgrade of the lower part of the garnet zone, S_T is much more regular than to the south (Fig. 3.3A), consistent with the interpretation that S_T more closely approaches a regional shear plane in the high-grade northern half of the study area, than in the lower-grade southern half. The greater competency of the low-grade rocks in the south may have precluded the development of a steady-state transposition foliation and complete rotation of structural elements towards the shear plane (i.e., the ductility of the rock was exceeded at lower strain than that required for establishment of a steady-state foliation; c.f. Means, 1981). This interpretation for the spatial variability of S_T attitudes differs from that of previous authors who attributed it to late (post-S_T development) folding (e.g., Van der Leeden, 1976; Brown et al., 1977). Rocks in the Big Fish Creek area therefore, are interpreted to be part of a zone of intense ductile strain, a ductile shear zone, here called the Big Fish Creek shear zone (BFSZ), characterized by spatial gradation in the nature and intensity of strain. As discussed in Chapter 2, development of S_T, and hence movement along the BFSZ, was at least in part contemporaneous with M2 metamorphism. The coincidence of the strain gradient with the M2 staurolite isograd suggests that metamorphic recrystallization may have served to facilitate ductile deformation in these rocks.

3.4.2 Nature of deformation

3.4.2.1 Orogen-transverse shear

Progressive deformation associated with the development of the transposition foliation in the study area involves an important component of orogen-transverse shear evidenced by the strong ENE-trending stretching lineation developed in quartzo-feldspathic rocks (Section 3.3.2.4; Plate 16). This stretching lineation corresponds to the orientation of maximum stretch (i.e., the X-axis of the finite strain ellipsoid) associated with constrictional strain during progressive deformation. The general orientation of gaps in split and micro-boudinaged garnet and other porphyroblasts at high angle to the stretching lineation (Section 3.3.2.5) is consistent with important constrictional strain. Many split porphyroblasts do not show substantial rotation synchronous with, or following splitting (Plates 9C, 13), which indicates

that orogen-transverse shear comprised a component of co-axial stretching. Orogen-transverse shear could also account for parallelism of fold axes, as well as the preferred orientation of the long axis of elongate biotite grains with the stretching lineation, as a result of rotation from an initial orientation at high angle to the maximum stretching direction (e.g., Sanderson, 1973; Escher and Watterson, 1974). However, an alternative explanation for this is discussed below which also accounts for the north-south-directed (i.e., orogen-parallel) shear also evident in rocks of the Big Fish Creek area.

3.4.2.2 Orogen-parallel shear

Some fabric elements suggest that deformation associated with progressive development of S_T involved a component of orogen-parallel stretching. The most direct evidence are mesoscopic north-dipping ductile extensional shear bands which intersect S_T at low-angle and disrupt it, locally producing an anastomosing pattern of foliation (an S-C' fabric; Platt and Vissers, 1980; Lister and Snoke, 1984; Plate 14A). Extensional shear bands and extensional cleavage (Platt and Vissers, 1980) are also observed at the microscopic scale, and are particularly well-expressed in sections cut normal to both S_T and the stretching lineation (Plates 12C, 14C), lending further support for substantial orogen-parallel extensional strain in rocks of the area. The preferred sense of vergence of these and other (see below) fabric elements suggests that non-coaxial, top-to-the-north shear was important, although the locally symmetric nature of shear bands encountered in S_T- and L_T-normal sections suggests a component of coaxial, orogen-parallel stretching (see below; Platt and Vissers, 1980).

The structures described above are the result of ductile strain, and therefore indicate that at least some of the orogen-parallel deformation occurred prior to substantial cooling of the host rocks following the peak of M2 metamorphism. Furthermore, rotation of these structures towards parallelism with S_T implies that orogen-parallel deformation was at least in part responsible for the progressive development of S_T itself. Several other ductile fabric elements encountered in the area may in part be explained by orogen-parallel shear. Figure 3.6 illustrates how S_T, S_T' and F_T are interpreted to be related to each other. As mentioned above, it is possible that S_T' and F_T fold axes were rotated into parallelism with the stretching lineation (e.g., Sanderson, 1973; Escher and Watterson, 1974). However, it is also allowable that S_T' and F_T resulted from orogen-parallel shear without substantial rotation, such as would be expected at the lateral tip of a spreading nappe (Fig. 3.7). This interpretation is consistent with other evidence for northwest-verging ductile deformation in the form of mesoscopic shear bands and other N-S-directed extensional features described above. This interpretation is also consistent with the observation of the preferred top-to-the-northwest sense of vergence indicated by S_T' and F_T and other structures (e.g., Plate

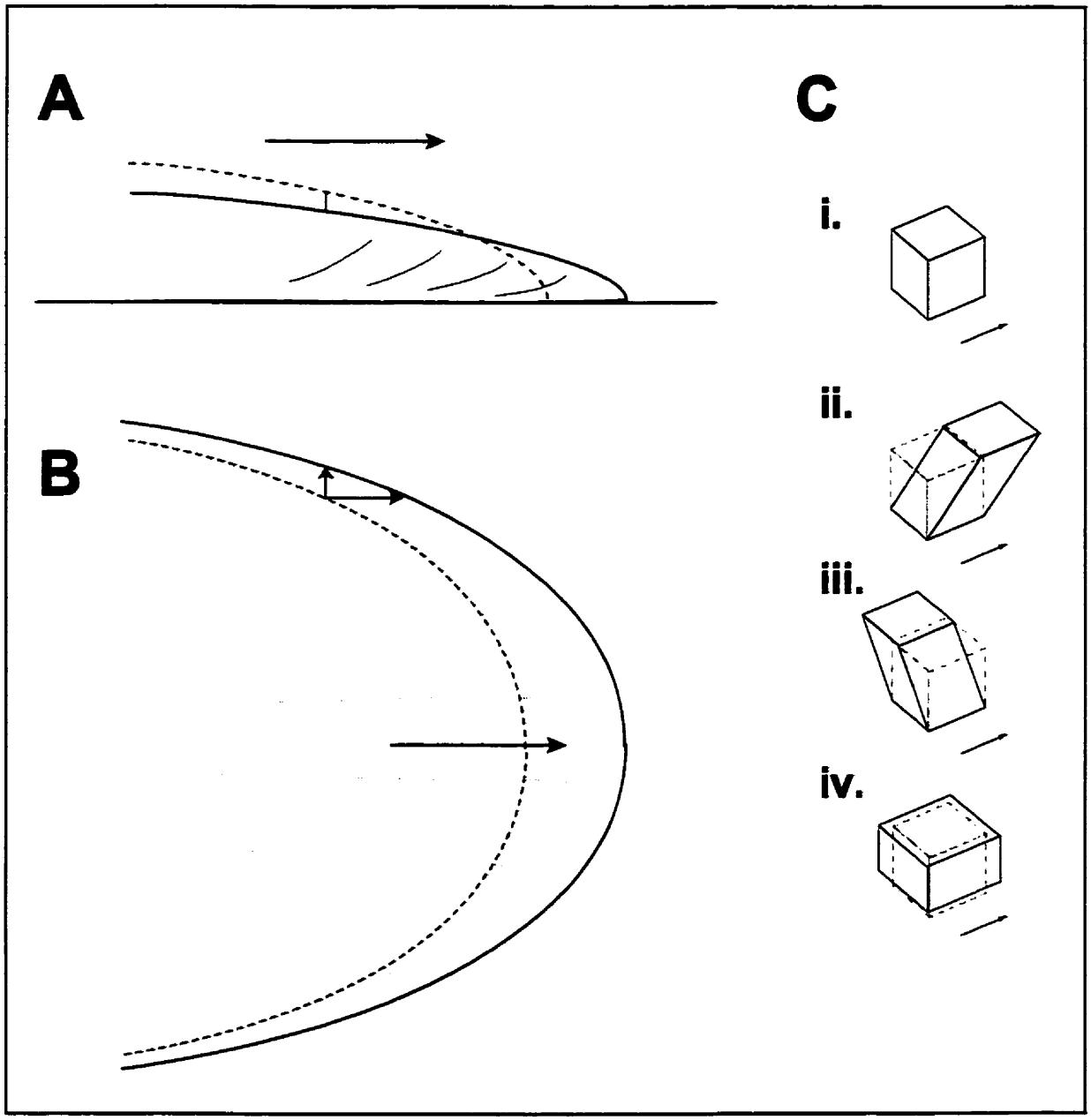

Figure 3. 7 Deformation at the frontal and lateral tips of a spreading nappe. Dashed outline is initial state. A: Cross-sectional view. B: Plan view. C: Different components of strain predicted; arrow points to direction of nappe movement: i. unstrained control volume; ii. transport-parallel (orogen-transverse) simple shear; iii. transport-normal (orogen-parallel) simple shear; iv. flattening parallel to regional shear plane (orogen-parallel and orogen-transverse coaxial extension).

14A). In contrast, rotation of these structures from initial orogen-parallel attitudes does not explain this asymmetry (i.e., produces sheath fold geometry; c.f. Coward and Potts, 1983).

3.4.2.3 S_T-normal shortening (sub-vertical "flattening")

In addition to orogen-parallel and orogen-transverse non-coaxial strain, a number of observations suggests that ductile progressive deformation involved a component of coaxial shortening perpendicular to S_T, or the regional shear plane (i.e., a component of flattening strain), especially in the high-grade, northern portion of the study area. Evidence includes split porphyroblasts with resulting gaps at high angle to S_T showing little evidence for rotation during or following splitting, and the locally symmetric rotation of planar structural elements such as biotite porphyroblasts and extensional crenulations and shear bands with respect to S_T. In particular, the fact that biotite porphyroblasts show symmetric rotation in sections normal to S_T and either normal or parallel to the stretching lineation indicates that extension was both orogen-parallel and orogen-normal (i.e., non-plane). Locally striking evidence of compositional segregation (Plates 9A, 14A) suggests that solution-aided mass transfer may have contributed to this component of co-axial deformation.

3.4.2.4 Transport direction

The foregoing discussion highlights the fact that ductile strain associated with S_T and related structural elements in the study area consisted of orogen-parallel and orogen-normal general non-coaxial strain. In addition, evidence has been presented which indicates that strain was both temporally and spatially heterogeneous. Hence, the present study area is interpreted as part of a long-lived zone of intense general non-coaxial shear of regional significance, the Big Fish Creek shear zone.

The preferred facing of transient biotite foliation and of extensional shear bands, and the vergence of folds with orogen-transverse axes indicate that orogen-parallel transport involved top-to-the-north-northwest displacement. Given the prevalence of orogen-transverse structures, and the extent of rotation of structural elements towards L_T, or towards S_T in L_T-parallel sections, it is clear that orogen-transverse shear was more important than orogen-parallel shear in the study area. The sense of displacement associated with the orogen-transverse component of shear is more difficult to ascertain, in large part because of loss of asymmetry in L_T-parallel sections, of kinematic indicators such as rotated biotite porphyroblasts, due to nearly complete rotation of these structural elements into parallelism with S_T (e.g., Plates 10C,D, 11D, 12A). In other areas of the southern Omineca Belt, orogen-transverse displacement

associated with similar structures (stretching and mineral lineations, orogen-transverse fold axes) is generally interpreted to reflect top-to-the-east transport (e.g., Read and Brown, 1981; Journeay and Brown, 1986; Journeay, 1986; Lane et al., 1989; Scammell, 1993; McNicholl and Brown, 1995; Johnston, 1996; Schaubs and Carr, 1998), and this may also apply to the present study area. In a limited number of instances, however, observed kinematic indicators appear to indicate top-to-the-west sense of shear (e.g., Plate 14D), which is in agreement with observations by Scammell (1993) and Johnston (1996), for rocks of the Monashee Mountains to the west, and of the Thor-Odin culmination, to the southwest, respectively, of the Big Fish Creek area (Fig. 3.1). The tectonic model proposed in Figure 3.8 implies an upper-plate-up-to-the-east sense of shear for the BFSZ (i.e., thrust motion), with an overlying (and/or partially superimposed), syn-thrusting, west-verging extensional shear zone (here correlated with the Norman Wood fault exposed to the east of the study area; Perkins, 1983; Scammell, 1993). An alternative interpretation would be an upper-plate-down-to-the-west shear zone associated with syn-orogenic extrusion of the underlying rocks, as proposed by Scammell (1993) and Johnston (1996) for other areas of the Selkirk Allochthon. The tectonic model presented in Figure 3.8 is further discussed in Section 3.4.3, below.

3.4.2 Timing of deformation

3.4.2.1 Relative timing of deformation and metamorphic recrystallization

Rocks of the study area record a complex and protracted history of prograde metamorphism (see Chapter 2). In pelitic rocks, metamorphic assemblages define a Barrovian sequence characterized by the presence of staurolite and kyanite in the higher grade rocks. Andalusite and pseudomorphs after andalusite (Plate 4B) are widespread in the central portion of the study area and their development post-dates the establishment of the Barrovian field gradient, as evidenced for instance by inclusions of early staurolite in andalusite porphyroblasts (Plate 4C,D). The above observations indicate that substantial decompression occurred between the onset of metamorphism in the area and the late stages of prograde metamorphism highlighted by the growth of andalusite.

Although the history of metamorphic recrystallization in the area is complex, the nature of the attending deformation was relatively constant. Extensively recrystallized pelitic rocks in the northern portion of the study area preserve the most complete record of metamorphism and hence, of its relationship to deformation. The features described in the following are characteristic of these rocks. Evidence for the earliest prograde metamorphism (M1) consists of anhedral cores of composite garnet

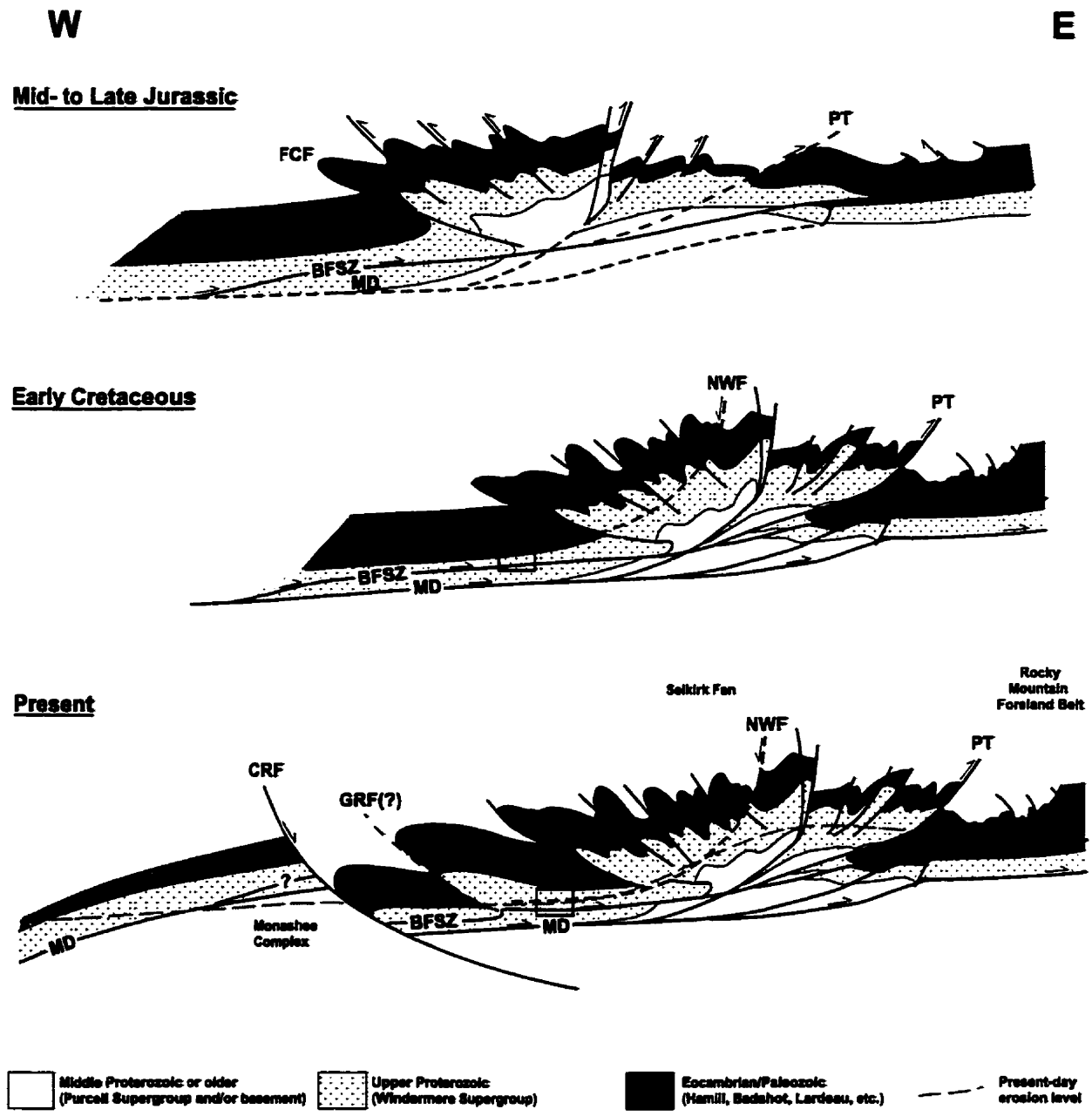

Figure 3.8 Simplified structural cross-section and tectonic model for the Selkirk Allochthon and Selkirk Fan at the latitude of the present study area. Big Fish Creek shear zone is a top-to-the-east contractional shear zone at mid-level in the Selkirk Allochthon, in the hangingwall of the Monashee Décollement. It is active at least as early as the Late Jurassic as east-directed wedging results in westward overthrusting, and thickening of the western flank of the Selkirk Fan. By middle to late Cretaceous time, eastward movement along the BFSZ may still be occurring. By that time, substantial thinning at mid-levels on the west flank of the Selkirk Fan has occurred, probably by a combination of lateral extrusion, and extensional movement along top-down-to-the-west ductile shear zone(s) such as the Norman Wood Creek fault. BFSZ: Big Fish Creek shear zone; CRF: Columbia River fault; FCF: French Creek Fault; MD: Monashee Décollement; NWF: Norman Wood Creek Fault; PT: Purcell Thrust. Modified after Colpron et al., 1998.

porphyroblasts which represent early porphyroblasts resorbed and dynamically split (or micro-boudinaged) prior to being overgrown by euhedral, M2 garnet rims (e.g., Plate 9A,B,C; Chapter 2). Development of M2 garnet overgrowth was followed by growth of M2 staurolite. Large andalusite porphyroblasts include, and therefore developed later than, this staurolite. Although M2 garnet tends to be inclusion-poor, abundant inclusions in M1 garnet cores typically define an internal foliation (S_i) which is typically straight and at low angle to the external foliation, S_e (= S_T; Plates 9C,D, 13A). In some cases, anhedral garnet cores preserve an internal foliation which appears to represent an earlier stage of S_T development (Plate 9D; also see Plate 1B). In the less common case where S_i is gently curved, it tends to line up with S_e near the margin of the core (Plate 13A). These observations indicate that M1 garnet growth was synchronous with, or post-dated the development of S_T, the dominant foliation.

M1 garnet porphyroblasts were split and resorbed prior to being overgrown by M2 euhedral rims. Typically, they are split into two sub-equant fragments with regular intervening gaps (e.g., Plate 2B). As previously described, the gaps generally lie perpendicular or at high angle to S_T, and to the direction of maximum finite stretching inferred from stretching lineations. This implies that progressive development of S_T and the stretching lineation was at least in part synchronous with garnet splitting.

Small euhedral M2 garnet porphyroblasts and M2 euhedral garnet overgrowths on resorbed M1 garnet cores are conspicuous. This textural discontinuity between core and overgrowth in composite garnet grains is associated with a sharp compositional discontinuity (Chapter 2, Plate 2). M2 garnet is typically inclusion-poor and spatially restricted to resorption rinds around early garnet, making the timing of its growth with respect to matrix foliation development difficult to establish. However, it is commonly associated with (and in some cases included in) inclusion-rich, euhedral M2 staurolite (Plate 9C) which is locally rotated with respect to, and deflects, foliation, suggesting that both M2 garnet and staurolite developed prior to the cessation of progressive deformation associated with development of S_T.

The final stage of prograde metamorphism observed in the area is the development of large (up to 15 cm-long; Plate 4B), elongate andalusite porphyroblasts (typically replaced by a muscovite-rich aggregate during subsequent retrogression) which locally include porphyroblasts of M2 garnet and/or staurolite (Plate 4C,D). A number of observations indicate that ductile deformation associated with development of S_T attended and/or post-dated growth of andalusite in the area. Andalusite crystals typically lie with their long-axis parallel to S_T, either as isolated grains, or as groups of needles defining conspicuous splays ("chickenfeet" texture; Plate 4B). Needles do not have a preferred orientation on S_T. Where fresh andalusite is found in thin section, it generally shows evidence of micro-boudinage, with

gaps at high angle to S_T (Plate 13C). Finally, muscovite in retrograde muscovite-rich aggregates after andalusite is typically aligned parallel to S_T (Plate 6D), indicating that S_T-related progressive deformation continued until after growth, and during or after retrogression of andalusite in the area.

Taken together, the foregoing textural observations indicate that S_T-related deformation in the study area, like metamorphic recrystallization, was protracted and attended by important temporal variations in ambient pressure and temperature conditions. Although few absolute time constraints on prograde metamorphism and deformation are available, these important fluctuations in metamorphic conditions suggests that prograde metamorphic recrystallization and the associated deformation, spanned a substantial temporal range. The absolute timing of deformation and metamorphism in the area is discussed below.

3.4.2.2 Absolute timing of deformation

Extensive deformation and metamorphism in the Selkirk Allochthon and adjacent areas of the southern Omineca Belt initiated in Early to mid-Jurassic time as a result of accretion of the Quesnellia island arc terrane to the western edge of North America (Monger et al., 1982; Brown et al., 1986, 1992a; Archibald et al., 1983; Colpron et al., 1996). Although direct supporting evidence is lacking, M1 metamorphism in the study area is interpreted to be of that age or younger.

The Bigmouth Creek pluton, a magmatic epidote-bearing alkali feldspar-phyric, hornblende granodiorite (Wheeler, 1965) intrudes supracrustal rocks exposed at the northern edge of the study area. Zircon and titanite U-Pb systematics were analyzed as part of this study and results are presented and discussed at length in Chapter 2. Salient points are briefly summarized here. Five discordant zircon separates yielded a lower intercept age of 157 ± 3.3 Ma, and an upper intercept age of 1.75 ± 0.02 Ga. Two titanite fractions were also analyzed which yielded concordant, but not overlapping, ages of 140.5 ± 0.8 Ma and 137.4 ± 1.4 Ma, respectively.

As discussed in the previous chapter, these results are interpreted to reflect emplacement and final crystallization of the Bigmouth Creek stock in late Middle Jurassic time, as implied by the zircon lower intercept age. M1 metamorphism is interpreted to be broadly synchronous with emplacement of the stock in the Middle Jurassic, based on the fact that mid-Jurassic metamorphism is common in other parts of the Selkirk Allochthon (e.g., Archibald et al., 1983; Brown et al., 1992a; Colpron et al., 1996). U-Pb resetting of titanite in Early Cretaceous time is interpreted to have resulted from a thermal pulse at that

time which also produced the M2 metamorphic overprint. The presence of magmatic epidote in the Bigmouth Creek granodiorite indicates minimum final emplacement pressure probably well in excess of 6 kbar (i.e., >20 km depth; Zen and Hammarstrom, 1984; Zen, 1985) in late Middle Jurassic time. The occurrence of M2 kyanite-bearing assemblages indicates that rocks in the northern part of the study area were still deeply buried and that the thickness of that part of the Selkirk Allochthon orogenic wedge was still considerable in Early Cretaceous time. This is in contrast to rocks of the Illecillewaet Synclinorium to the south, in the vicinity of the Fang granodiorite stock where, Colpron et al. (1996) have argued, Barrovian (moderate to high-P) regional metamorphism, and subsequent rapid exhumation and decompression to ca. 3 kbar were mostly over by 168 Ma (mid-Jurassic). In the present study area, the persistence of high pressures to Early Cretaceous time implies that the late M2 decompression associated with development of andalusite, and the associated deformation must be younger (i.e., Early Cretaceous or younger).

Thus, ductile deformation in the study area began in the Middle Jurassic, following accretion of the Quesnellia island arc terrane, and continued, episodically at least, until the Early Cretaceous or later. Late Cretaceous (ca. 76 Ma) muscovite and biotite Ar-Ar cooling ages obtained for rocks in the southern part of the study area (Colpron, personal communication, 1996) suggest that final exhumation and cooling did not occur until 50 m.y. later, at least.

3.4.3 Tectonic implications

The structural style which resulted from ductile deformation in the Big Fish Creek area is similar to that observed in structurally deeper rocks near the base of the Selkirk Allochthon, throughout the southern Omineca Belt. Features encountered in the Big Fish Creek area which are also widespread in other areas include evidence for long-lived transposition of structures towards a shallow-dipping regional shear plane, a strong ENE to WSW-trending mineral/stretching lineation, orogen-transverse, stretching lineation-parallel fold axes, and evidence for substantial syn-compressional extension parallel to the stretching lineation (e.g., Journeay, 1986; Journeay and Brown, 1986; Lane and Brown, 1988; Scammell; 1993; McNicoll and Brown, 1995; Johnston, 1996; Schaubs and Carr, 1998).

Both Scammell (1993) and Johnston (1996) have interpreted extensional strain at the base of the Selkirk Allochthon as resulting from large-scale syn-compressional extension associated with extrusion (e.g., Burchfield and Royden, 1985; Thompson et al., 1997) of a mid-crustal wedge as a result of gravitational collapse. According to these authors, extension took place prior to cessation of eastward

displacement of this wedge in the Early Tertiary (Carr, 1992), as recorded by the continued development of the regional ENE-WSW-trending orogen-transverse lineation. Eastward displacement of rocks exposed in the Big Fish Creek area is also evidenced by the widespread occurrence of an ENE-WSW-trending orogen-transverse lineation, illustrating the distributed nature of deformation associated with east-directed transport in the lower part of the Selkirk Allochthon from Late Jurassic to Early Tertiary time. This and the preferred vergence of structures associated with orogen-parallel shear support the interpretation that these rocks were located near the base, and at the lateral edge of a mid-level, east-directed thrust nappe within the Selkirk Allochthon (c.f., Butler, 1982; Coward and Potts, 1983; Fig. 3.7) during mid-Jurassic to Early Cretaceous time at least. Evidence for S_T-normal shortening and transport-parallel extension prior to Late Cretaceous cooling, and contemporaneous with apparently rapid decompression (as recorded by the late- M2 development of andalusite) is consistent with an evolution involving extension and crustal thinning (e.g., Jamieson and Beaumont, 1988; Hodges et al., 1993; Thompson et al., 1997) during continued eastward displacement of the Selkirk Allochthon.

Syn-compressional extension affected rocks in higher structural levels of the Selkirk Fan as early as the Middle Jurassic (Colpron et al., 1996) as the Selkirk Fan structure was developing into a thickened, doubly-vergent orogenic wedge (Malavieille, 1984; Willett et al., 1993; Brown et al., 1993) as a result of eastward underthrusting of a westerly-derived crustal slab below the western edge of the wedge (Figs. 3.8A, 3.9A; Brown et al., 1986, 1993; Price, 1986; Colpron et al., 1998) and east-vergent overthursting of the eastern part of the wedge over the North American continental margin. The lack of evidence for significant post-mid-Jurassic penetrative deformation and metamorphism in rocks of the Illecillewaet Synclinorium (Colpron et al., 1996) suggests that from the Late Jurassic on, rocks at high structural levels in the Selkirk Fan underwent mostly passive eastward translation as a result of movement along shear zones at deeper structural levels (Fig. 3.8).

In contrast, Scammell (1993) has argued that rocks near the base of the Selkirk Allochthon to the west of the Big Fish Creek area record deformation associated with eastward displacement of the Allochthon from as early as 135 Ma to as at least as late as 100 Ma. As in the Big Fish Creek area at intermediate structural level, and in the Illecillewaet Synclinorium at high structural level, evidence for syn-compressional extension also exists at the base of the Selkirk Allochthon (Scammell, 1993; Johnston, 1996). Scammell (1993) has suggested the Norman Wood Creek fault, whose trace is exposed several kilometers east of the study area (Perkins, 1983), as a possible candidate for an upper-plate-down-to-the-west, syn-compressional extensional fault in the hangingwall of the Monashee Décollement, and this is

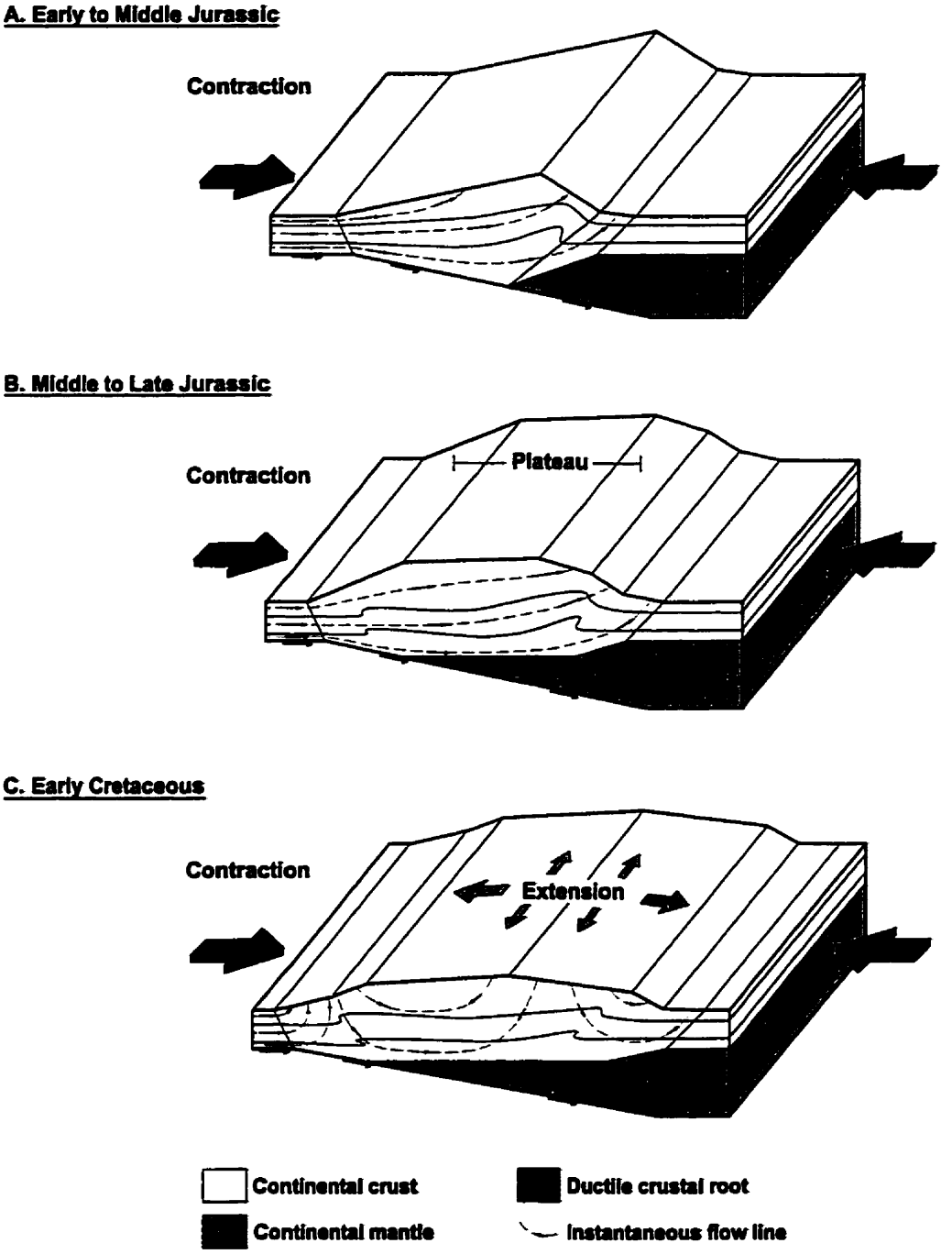

Figure 3.9 Proposed dynamic wedge tectonic model for the Selkirk Allochthon to account for inferred metamorphic and structural evolution. Modified after Willett et al., 1993. A: Early accretion of westerly-derived terrane to the western edge of North America and associated contraction leads to crustal thickening, thermal relaxation of thickened wedge, and results in M1 metamorphic event. B: A stable wedge geometry is established which is maintained by the balance of far-field contractional stresses and expansion of ductile crustal root due to continued thermal relaxation. Parts of the orogenic wedge undergo burial while others are uplifted, accounting for limited retrogression between M1 and M2 metamorphic event. Continued growth of the wedge and associated thermal relaxation locally (at least) produce heating and result in M2 metamorphism. C: Relaxation of far-field contractional stresses and/or expansion of the ductile crustal root leads to substantial gravitational collapse of the dynamic wedge, during the late stages of M2 metamorphism. Resulting extension produces denudation and decompression as recorded by development of late-M2 andalusite.

tentatively integrated in the model presented in Figure 3.8, to accommodate evidence for ductile, west-vergent deformation encountered in the Big Fish Creek area.

Thus it appears that the eastern part of the Selkirk Allochthon, in particular the Selkirk Fan and adjacent areas, represents a long-lived, doubly-vergent dynamic orogenic wedge (Malavieille, 1984; Willett et al., 1993) resulting from far-field compressional stresses induced by continued convergence of accreted terranes to the western margin of North America, and from internal deformation involving both compressional and extensional components, acting to maintain a critically tapered topography (Figs. 3.8, 3.9; e.g., Davis et al., 1983; Dahlen et al., 1984; Willett et al., 1993). A possible model for the evolution of the Selkirk Allochthon and Selkirk Fan which integrates the results of the present study is illustrated in Figure 3.9. Development of a doubly-vergent wedge began in Early to mid-Jurassic time (ca. 173 Ma; Colpron et al., 1996; 1998), but initially may have been limited in size as suggested by the lack of substantial sediment input to the foreland basin until Late Jurassic time (Price and Mountjoy, 1970). By mid- to Late Jurassic time (ca. 160-155 Ma), the eastern part of the wedge had overridden the basement ramp which defined the landward boundary of the thick Proterozoic to Early Paleozoic continental margin sequence (Fig. 3.8A; Colpron et al., 1998), and the resulting gravitational potential in the eastern part of the orogenic wedge was apparently balanced by a substantially thickened western part of the wedge, as evidenced by emplacement of the magmatic epidote-bearing Bigmouth Creek pluton in supra-crustal rocks at depths well in excess of 20 km. Thickening of the western part of the orogenic wedge was the result of underplating of the wedge by westerly-derived material along west-verging thrust faults such as the French Creek Fault (Fig. 3.8), synchronous with eastward displacement along deeper-level, ductile shear zones such as the Big Fish Creek shear zone. Dynamic maintenance, and possibly continued growth of the thickened wedge until the Early Cretaceous (Fig. 3.8B) is evidenced by kyanite-bearing M2 metamorphic assemblages. Eventually, thermal relaxation of the thickened wedge produced an increase in temperature in the mid- to lower levels of the wedge, leading to enhanced ductility, which in turn facilitated continued shear and progressive deformation along such a ductile shear zone, as well as gravitationally-driven ductile extension (Figs. 3.8B, 3.9C), thinning and resulting decompression at these structural levels, in response to the increased overlying load (i.e., "dynamic spreading" and extrusion; e.g., Holdsworth and Grant, 1990).

3.5 Conclusions

Rocks in the Big Fish Creek area appear to have preserved a more complete record of deformation and metamorphism in the Selkirk Allochthon than rocks at higher structural levels (due to

their "passive" behavior after the Middle Jurassic) and at lower structural levels (due to the continued high-grade metamorphic overprint until the Late Cretaceous, which obliterated the record of earlier evolution). Some key features of this record had previously gone unrecognized. These include: 1) the polycyclic nature of prograde metamorphic recrystallization implying two episodes of heating to amphibolite facies conditions and an intervening episode of cooling; 2) the widespread occurrence, in higher grade rocks of the Big Fish Creek area, of late andalusite which indicates decompression late in the metamorphic recrystallization history; 3) evidence for very intense strain consistent with deformation in a zone of high distributed, general shear; 4) evidence for substantial shortening normal to the dominant shallow-dipping foliation (i.e., flattening) in the area; and 5) a Middle Jurassic emplacement age for the Bigmouth Creek Stock with evidence for themal reworking to Late Jurassic-Early Cretaceous time. These new lines of information suggests a metamorphic and associated tectonic evolution distinct from that proposed in earlier models involving simple, foreland-, and downward-propagation of metamorphic and deformation fronts within the southern Omineca Belt (e.g., Parrish et al., 1995), or cessation of tectonic and metamorphic activity by mid-Jurassic time in the Northern Selkirk Mountains (e.g., Colpron et al., 1996).

Hence, the Big Fish Creek area provides information crucial to the unraveling of the tectonic evolution of the southern Omineca Belt in Mesozoic time. Based on the structural and metamorphic features observed in the Big Fish Creek area, the following major conclusions may be synthesized:

1. Rocks in this area record intense, non-coaxial strain which resulted from long-lived ductile progressive deformation, and involved important components of orogen-transverse and orogen-parallel extension (i.e., sub-vertical shortening normal to the dominant transposition foliation S_T, which approaches the regional shear plane).

2. These rocks are therefore interpreted to be part of a ductile shear zone of regional significance, herein named the Big Fish Creek shear zone. The presence of this shear zone at intermediate levels in the Selkirk Allochthon illustrates the distributed nature of strain associated with east-directed displacement of the Selkirk Allochthon during Mesozoic to Early Cenozoic time, rather than its being restricted to movement along the sole thrust of the Allochthon, the Monashee Décollement.

3. Structural and metamorphic evidence for diachronous syn-compressional extensional strain and crustal thinning in the Big Fish Creek area, combined with similar interpretations at both higher, and lower structural levels by other workers, suggests that the Selkirk Allochthon, at least in the area of the Selkirk

Fan structure, constituted a dynamic orogenic wedge from as early as the Middle Jurassic, to at least as late as the Late Cretaceous. The dynamic behavior of this wedge was controlled by far-field forces associated with convergence of accreted terranes and the North American continental margin, by gravitational forces, and by rheological modification and internal deformation of the wedge in response to these different controls.

4. Based on U-Pb age dating of the Bigmouth Creek granodiorite, the high-pressure, early stage of regional metamorphism recorded in rocks of the area can be assigned to mid-Jurassic time. This implies that syn-metamorphic progressive deformation began at least as early as the Middle Jurassic. Thermal resetting, in the Early Cretaceous, of Bigmouth Creek stock titanite U-Pb systematics constrains the timing of M2 metamorphism to Early Cretaceous time. Late-M2 decompression was therefore Early Cretaceous or younger, and predates the end of ductile deformation associated with the transposition foliation in the area. This also puts an Early Cretaceous upper boundary on syn-compressional extension and gravitationally-driven thinning of the Selkirk Allochthon orogenic wedge.

Chapter 4

IRREGULAR ISOGRADS, REACTION INSTABILITIES, AND THE EVOLUTION OF PERMEABILITY DURING METAMORPHISM

4.1 Introduction

Rocks in the Big Fish Creek area show evidence of fluid flow attending recrystallization. Retrogression of peak mineral assemblages after both prograde metamorphic events recorded in these rocks was attended by fluid infiltration, as indicated by the hydrous nature of the retrograde minerals (e.g., chlorite and biotite after M1 garnet, muscovite-rich aggregates after M2 staurolite and andalusite). However, the fact that the same prograde minerals show variable degrees of replacement by hydrous phases indicates that fluid-flow-driven retrogression was heterogeneous (e.g., M1 garnet, compare Plate 1B and 1C; M2 staurolite, compare Plate 5C,D and Plate 6B; late-M2 andalusite, compare Plate 6C and 6D). When attempting to understand the rates and patterns of fluid flow in mid-crustal environments such as the Big Fish Creek area, the nature of permeability is critically important. However, it remains poorly constrained at best. Metamorphic mineral reactions can alter porosity leading to modification of permeability and fluid flow distribution. Reactions that increase porosity will tend to enhance permeability and focus fluid flow (e.g., Rumble et al., 1982). If fluid flow drives mineral reaction, a positive feedback may develop between infiltration and reaction which will result in runaway flow-focusing (e.g., Ortoleva et al., 1987). Fluid flow will become increasingly heterogeneous. Alternatively, reactions that decrease porosity may reduce permeability and divert flow away from the reaction site (e.g., Cook et al., 1997). Either way, mineral reactions alter fluid flow patterns and the resulting distribution of chemical alteration and mineral assemblages.

Recently, the heterogeneity of stable isotopic alteration has been used to constrain the spatial variability of permeability during metamorphism of carbonate rocks (Bowman et al., 1994; Cartwright, 1994; Gerdes et al., 1995). However, the mineralogical record of fluid flow has not been similarly evaluated. Because infiltration drives decarbonation reactions in these rocks (e.g., Ferry, 1994b), the distribution of metamorphic mineral assemblages is also a record of permeability distribution. Moreover, if metamorphic modification of permeability was an important control on fluid flow distribution, then this must be reflected in the distribution of mineral assemblages.

Here we model reactive transport through heterogeneous permeability to quantify the spatial variability of fluid flow required to produce observed distributions of mineral assemblages in contact metamorphosed siliceous dolomites. We compare these results to fluid flow heterogeneity predicted from the distribution of stable isotopic alteration, and show that in a number of contact aureoles the mineralogic and isotopic records of fluid flow are extremely heterogeneous. We propose that this heterogeneity is the result of permeability enhancement by mineral reaction.

4.2 The record of fluid flow

Contact metamorphosed siliceous dolomites of the Alta (Utah) and Ubehebe (California) aureoles show similar distributions of mineral assemblages. At Alta, the minerals talc, tremolite, forsterite, and periclase (inferred from secondary brucite) define metamorphic isograds with increasing proximity to the Alta stock (Fig. 4.1A; Moore and Kerrick, 1976). At Ubehebe, the progressive sequence of isograds is defined by tremolite, forsterite, and periclase (Roselle, 1997). Applying one-dimensional (1D) models of reactive transport of H_2O-CO_2 fluid in siliceous dolomite, Ferry (1994b) showed that these mineral assemblage distributions, in particular the presence of periclase and absence of diopside, require pervasive, grain-scale infiltration of aqueous fluid in the direction of decreasing temperature (e.g., Fig. 4.2B). He estimated a time-integrated fluid flux for Alta in excess of 1000 mol fluid/cm^2 of rock.

Whole-rock carbonate ^{18}O is variably depleted in the inner portions of both the Alta and Ubehebe aureoles (Fig. 4.1B; Bowman et al., 1994; Roselle, 1997). The magnitude of ^{18}O depletion matches that predicted to result from infiltration of H_2O-rich, isotopically light magmatic volatiles. Bowman et al. (1994) estimated a time-integrated fluid flux for Alta of approximately 4000 mol/cm^2. They attributed the spatial variability of ^{18}O depletion to hydrodynamic dispersion resulting from heterogeneous fluid flow. In their 1D reactive transport models, hydrodynamic dispersion results in a broadening of the isotopic alteration front, but does not account for the scatter of values about that front (Fig. 4.1B). Gerdes et al. (1995) used two-dimensional (2D) stochastic models to show that heterogeneous fluid flow could produce this isotopic scatter.

Because the distribution of mineral assemblages depends on the amount of fluid flow (Fig. 4.2B), the heterogeneity of flow implied by the stable isotopic scatter must also influence the geometry of mineral isograds if the two processes are coupled. At Alta, periclase-bearing and periclase-absent marbles are interlayered on a meter scale (Cook et al., 1997), and forsterite- and periclase-grade rocks

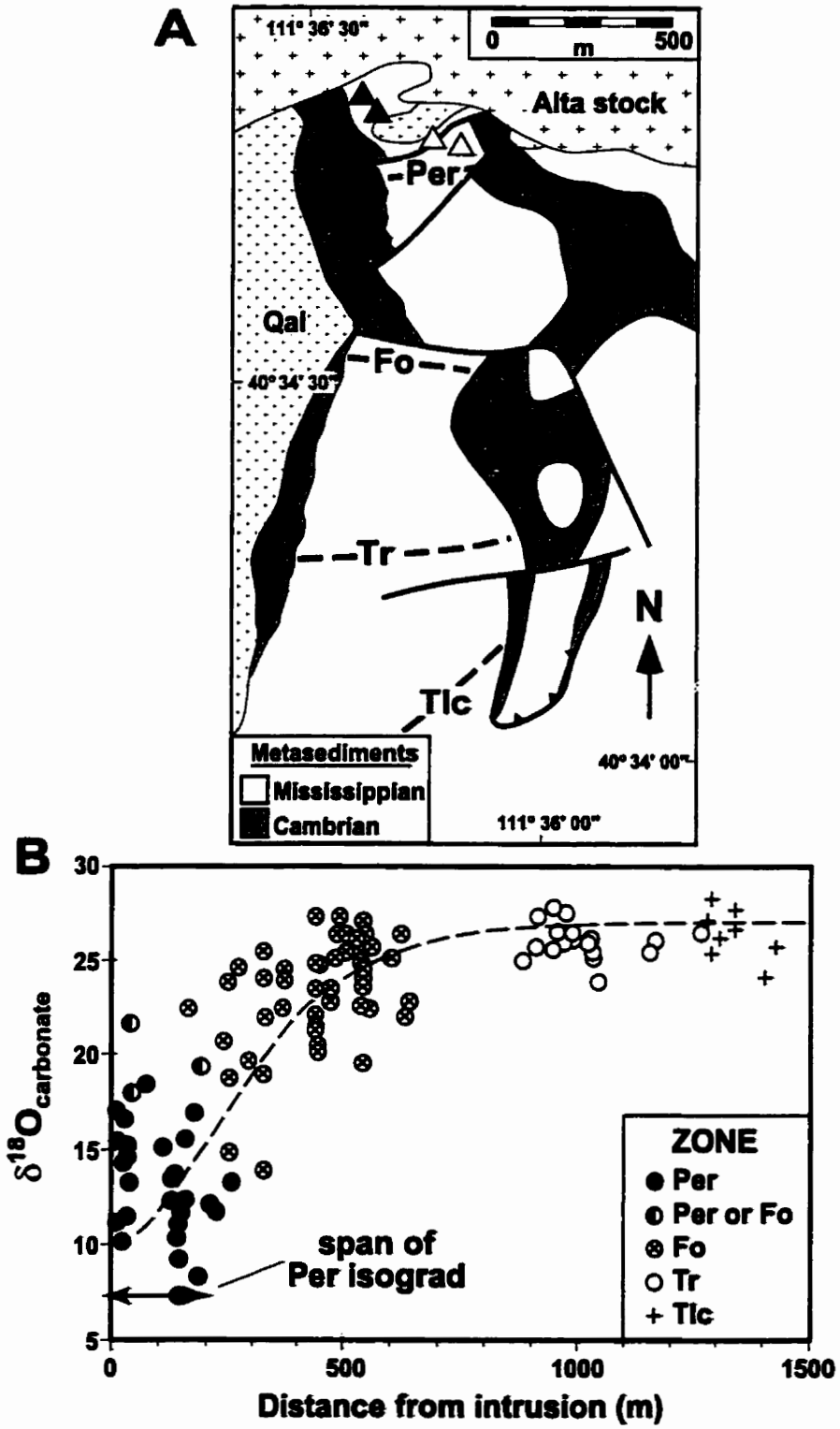

Figure 4.1 A: Map of southern portion of Alta, Utah contact aureole (adapted from Cook, 1992). Talc (Tlc), tremolite (Tr), forsterite (Fo), and periclase (Per) isograds mark first appearance of these minerals as pluton is approached. However, low-grade assemblages persist into higher-grade zones: forsterite-grade rocks occur within periclase zone to 50 m from contact, as reported by Smith (1972; filled triangles) and Cook (1992; open triangles). B: Whole-rock carbonate $\delta^{18}O$ (standard mean ocean water) of siliceous dolomites vs. distance from contact (modified after Cook, 1992). Span of periclase isograd is zone over which periclase- and forsterite-grade rocks overlap. Dashed curve denotes alteration predicted by model of Bowman et al. (1994). Mineral abbrevations as in A.

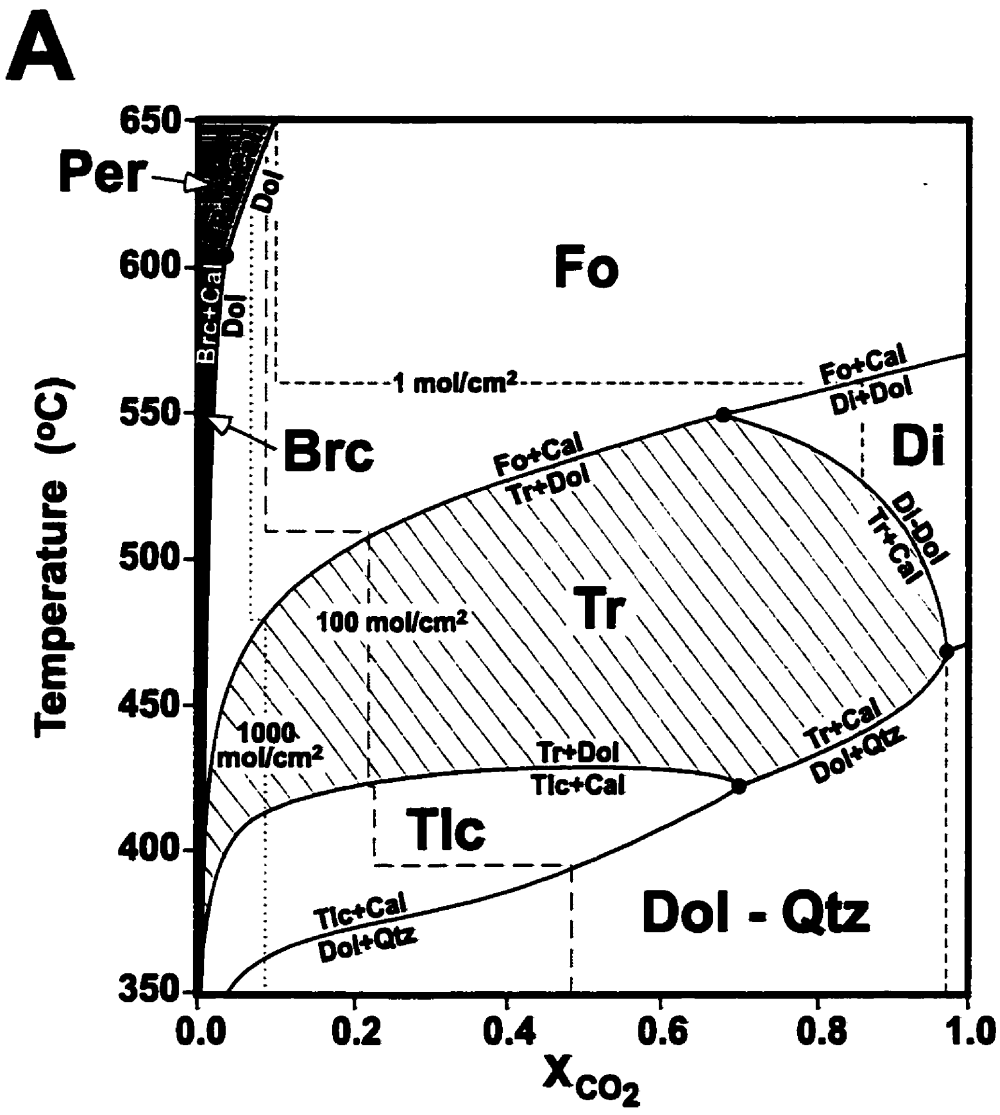

Figure 4.2 A: Isobaric (1 kbar) phase diagram for model siliceous dolomite showing mineral assemblage stability as function of temperature and mole fraction of CO_2 in H_2O-CO_2 fluid. Dashed lines show mineral assemblage sequences and equilibrium fluid compositions for three different time-integrated fluid fluxes, during down-T flow of H_2O from the intrusive contact. Thermodynamic data from Berman (1988). Dol: dolomite; Qtz: quartz; Cal: calcite; Di: diopside; Brc: brucite; all others as in Figure 4.1.

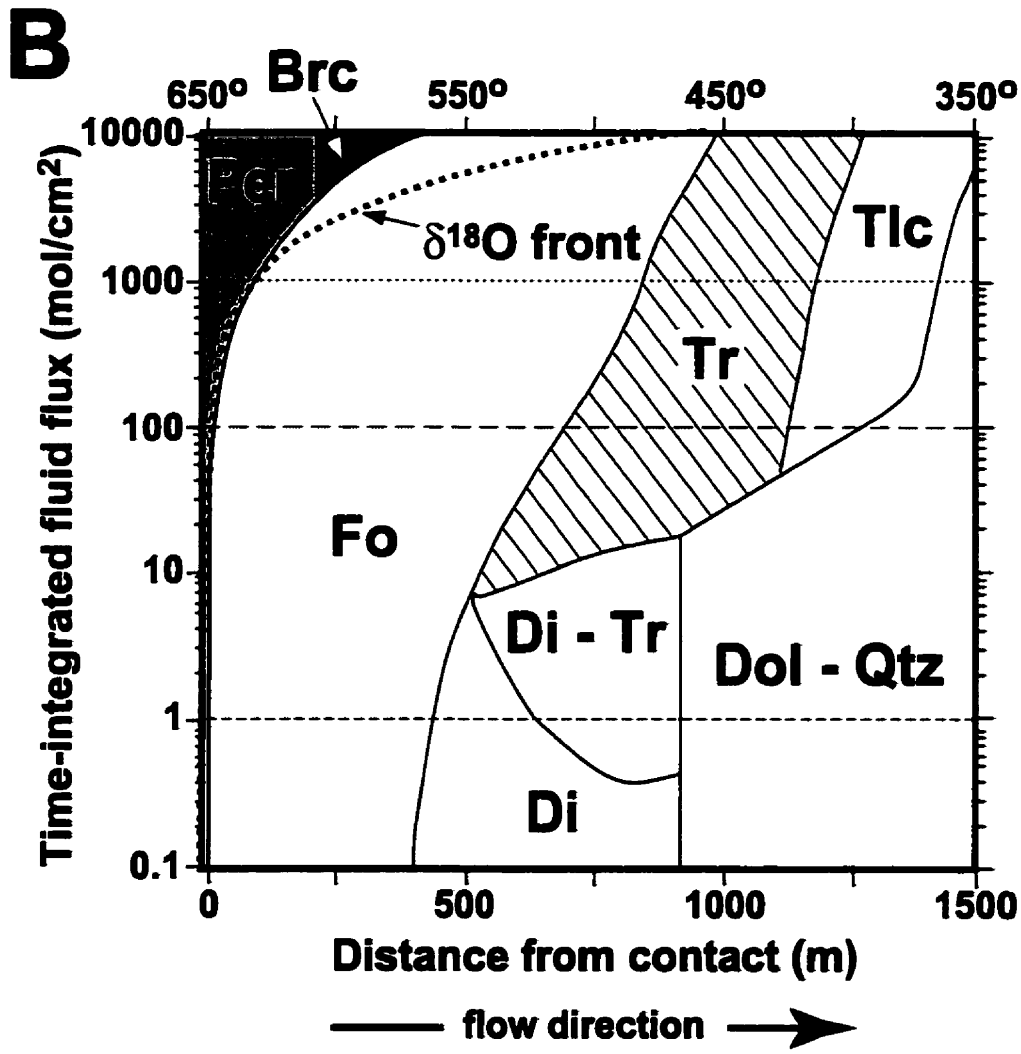

Figure 4.2 B: Mineral assemblage stability as function of distance from intrusive contact and time-integrated fluid flux. Thin dashed lines denote assemblage sequences for same fluxes as in A. Displacement of ^{18}O alteration front is shown as heavy dashed line. Assemblage fields are: Dol-Qtz: dolomite + quartz protolith; Tlc: Tlc+Dol+Cal; Tr: Tr+Dol+Cal; Di: Di+Dol; Fo: Fo+Dol+Cal; Brc: Brc+Cal; Per: Per+Cal; Di-Tr: Di+Tr+Dol+Cal.

overlap over ≈250 m (Fig. 4.1B; metamorphic grades are defined in Fig. 4.2). Roselle (1997) observed a similar overlap in the Ubehebe aureole, and Ferry and Rumble (1997) documented a heterogeneous distribution of periclase in siliceous dolomites of the Silver Star and Beinn an Dubhaich aureoles. Thus, mineral assemblages in contact-metamorphosed carbonate rocks also appear to record heterogeneous fluid flow.

4.3 Models

We used finite-difference methods to model 2D heterogeneous fluid flow through siliceous dolomite initially composed of 90% dolomite and 10% quartz by volume, a composition representative of massive siliceous dolomites at Alta (e.g., Moore and Kerrick, 1976). The stability of mineral assemblages in this system varies with temperature and fluid composition (Fig. 4.2A). Each rock in the model aureole was heated and equilibrated to peak metamorphic temperature prior to infiltration. Further mineral reaction was driven by infiltration of magmatic H_2O down the steady-state peak thermal gradient (down-T flow, Figs. 4.2B and 4.3). We did not account for heat flow because doing so adds considerable numerical complexity but does not appreciably affect the sequence or general displacement of mineral isograds with infiltration (Dipple and Ferry, 1996). However, without accounting for heat flow, primary and secondary brucite cannot be distinguished. The presence of either brucite or periclase is used to define the periclase zone at Alta (Moore and Kerrick, 1976) and in our analysis. Stable isotopic alteration is driven by down-T flow of pure magmatic H_2O with a $\delta^{18}O$ of 7‰. Fluid-rock exchange is approximated by the calcite-H_2O system (e.g., Bowman et al., 1994; Gerdes et al., 1995); initial $\delta^{18}O$ of calcite is 25‰.

Steady-state heterogeneous permeability was represented by stochastic distributions generated with geostatistical software (Deutsch and Journel, 1992), by fixing the mean, variance, and spatial correlation of the natural logarithm of permeability (ln[k]). The permeability maps had a geometric mean of 10^{-15} m^2. We changed the spatial variance (σ^2) of ln(k) between simulations (e.g., Gerdes et al., 1995) to assess how heterogeneous permeability affects mineral assemblage and $\delta^{18}O$ distributions. Spatial correlation was anisotropic, with characteristic correlation distances (i.e., the variogram ranges; de Marsily, 1986) of 300 m longitudinal and 30 m transverse to flow (Gelhar, 1993; Gerdes et al., 1995). Steady-state distributions of flow velocities were obtained by imposing high fluid pressure at the inflow boundary (intrusive contact), low fluid pressure at the outflow boundary (unmetamorphosed country rock) and impermeable flow-parallel boundaries. Fluid flow, although heterogeneous, was generally away from the intrusive contact. Fluid production by metamorphic mineral reactions was neglected.

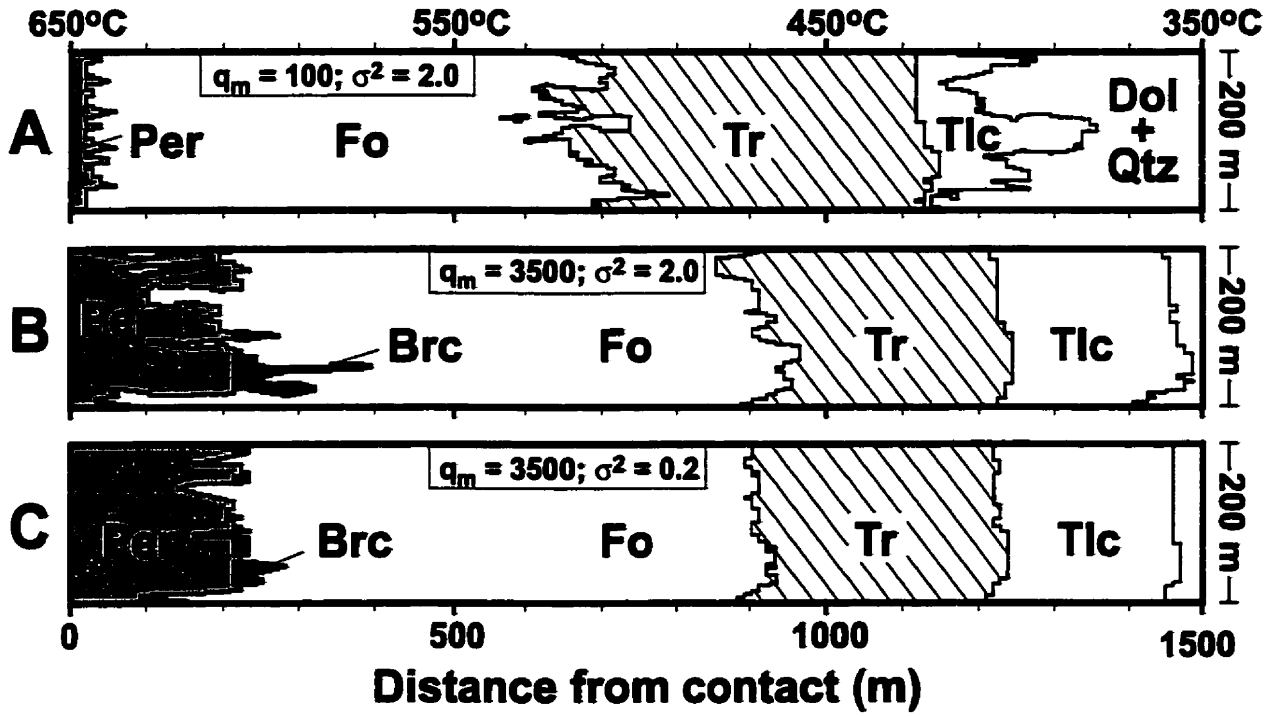

Figure 4.3 Mineral assemblage maps for down-T flow of initially pure H_2O fluid into siliceous dolomites for different spatially averaged time-integrated fluid fluxes (q_m) and variances of ln(k). Mineral fields are as defined in Figure 4.2. Note that irregularity of mineral isograds is more pronounced where permeability is very heterogeneous.

At each timestep, fluid infiltrated the rock and reaction proceeded until chemical equilibrium was reached. This was done for each of 30 000 nodes until the prescribed final time-integrated fluid flux (q_m) was attained. Results are presented as mineral assemblage maps and $\delta^{18}O$ distributions for different values of q_m and $\sigma^2(\ln k)$ (Figs. 4.3 and 4.4). Unless otherwise mentioned, results are for a q_m of 3500 mol/cm^2, which yields a good fit to observed isograd and ^{18}O front displacements at Alta.

4.4 Results

Figure 4.3 illustrates the effect of heterogeneous permeability on the geometry of mineral zones and isograds. For a given q_m, the sequence of mineral assemblages and displacement of mineral isograds predicted for 2D heterogeneous flow are similar to the 1D solution (cf., Figs. 4.2B and 4.3). However, heterogeneous fluid flow produces irregular isograds; in more permeable zones, isograds are displaced towards lower temperature (Fig. 4.3). Our results indicate that even moderately heterogeneous permeability fields yield irregular mineral isograds, as illustrated in Figure 4.3C for a permeability field with $\sigma^2(\ln k) = 0.2$, a value typical of relatively homogeneous near-surface aquifers (e.g., Gelhar, 1993). However, the preservation of forsterite-grade assemblages in the inner 50 m of the Alta (Fig. 4.1) and Ubehebe (Roselle, 1997) aureoles requires a more heterogeneous distribution of periclase such as that in Figure 4.3B, which records flow through a highly heterogeneous permeability field ($\sigma^2(\ln k) = 2.0$).

The pattern of ^{18}O depletion in the inner aureole at Alta also requires highly heterogeneous permeability ($\sigma^2(\ln k) = 2.0$; Fig. 4.4). In general agreement with Gerdes et al. (1995), our results show that flow through a more homogeneous permeability field would not reproduce the observed $\delta^{18}O$ distribution (Fig. 4.4). The observed distribution of mineral assemblages and ^{18}O alteration at Alta is consistent with down-T flow of 3500 mol/cm^2 through a very heterogeneous permeability field.

4.5 Discussion

Our results highlight two important features of reactive transport during contact metamorphism at Alta: (1) the geometry of the periclase isograd and the scatter in $\delta^{18}O$ values record similar fluid-flow heterogeneity; (2) this heterogeneity was extreme. Similar isotopic and mineral assemblage distributions in other aureoles (e.g., Ubehebe, Silver Star, Beinn an Dubhaich) indicate that highly heterogeneous fluid flow may be a common feature of contact metamorphism.

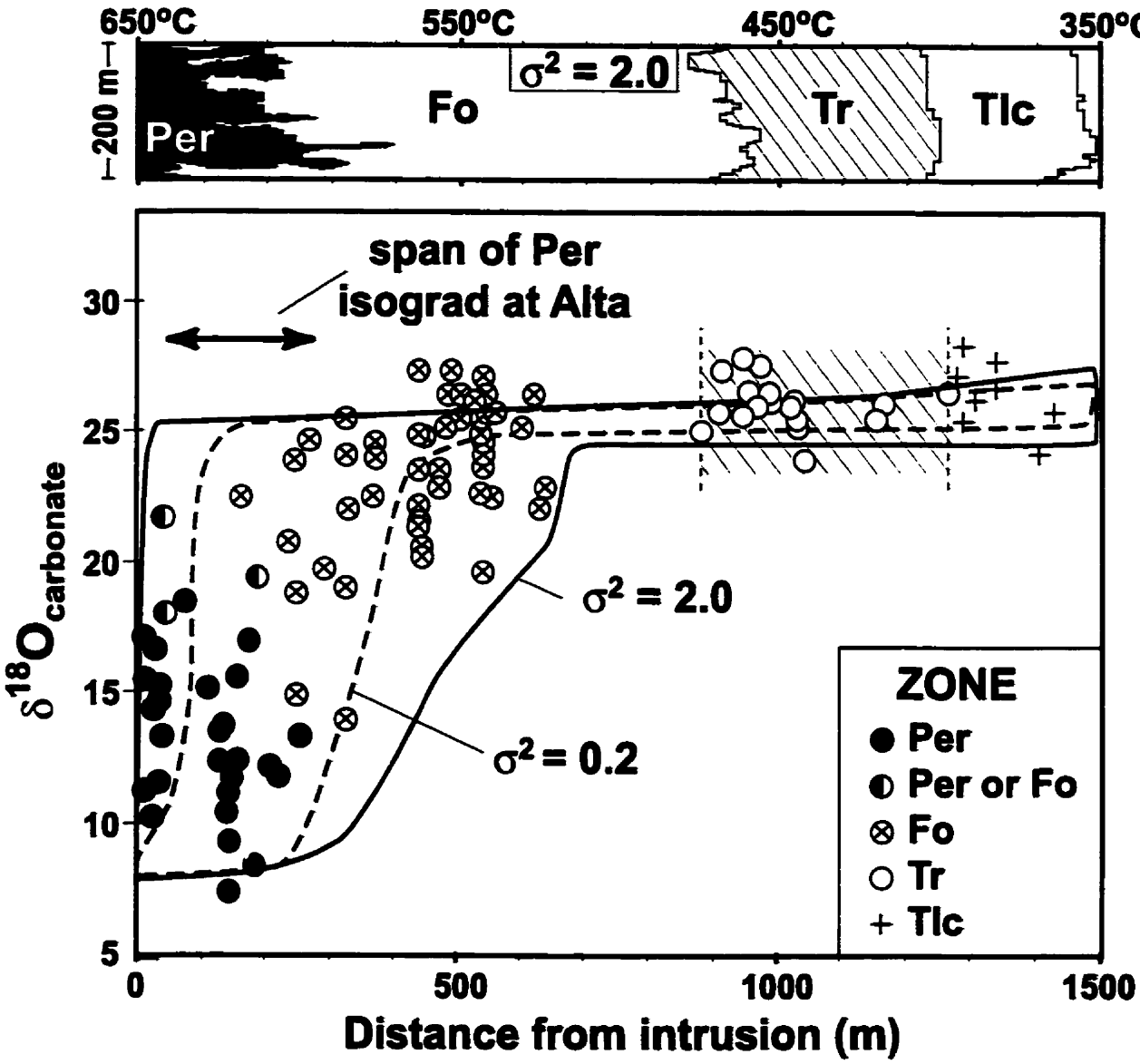

Figure 4.4 Comparison of model results with Alta observations. Top frame is as in Figure 3B, with Per and Brc fields combined. Bottom frame shows model $\delta^{18}O$ distribution for qm = 3500 mol/cm^2 through permeability fields with $\sigma^2(\ln k) = 0.2$ (dashed) and $\sigma^2(\ln k) = 2.0$ (solid). Note agreement between model $\delta^{18}O$ distribution for $\sigma^2(\ln k) = 2.0$ and $\delta^{18}O$ distribution at Alta. Also shown are span of periclase isograd (arrow) and tremolite zone (oblique rule) at Alta.

Periclase and $\delta^{18}O$ distributions at Alta are both consistent with highly heterogeneous permeability ($\sigma^2(\ln k) \approx 2.0$; Fig. 4.4). Only the most heterogeneous near-surface aquifers show such high variability (e.g., Gelhar, 1993). In fact, the range of permeability (nearly 5 orders of magnitude) suggested by comparing Alta data with model results exceeds by nearly two orders of magnitude that estimated by Ferry (1994a) for 266 samples of diverse metamorphic rock types from across northern New England. Given the limited geographic extent of the Alta aureole (Fig. 4.1A), fluid flow was very heterogeneous there, and perhaps also at Ubehebe, where periclase isograd geometry and $\delta^{18}O$ scatter are similar to those at Alta (Roselle, 1997).

We interpret the extreme heterogeneity of fluid flow in the Alta aureole to be the result of flow-focusing during metamorphism rather than a direct reflection of extreme heterogeneity in the protolith. Flow-focusing is an expected consequence of infiltration-driven reaction involving a decrease in solid volume (i.e., porosity enhancement) due to the development of positive feedback between flow, reaction and permeability enhancement (e.g., Ortoleva et al., 1987). Because prograde isograd reactions in siliceous dolomites involve a significant decrease in solid volume (e.g., 25% for the periclase isograd reaction), reaction enhancement of permeability is a likely cause of the high heterogeneity of fluid flow. Thus, although the synmetamorphic permeability structure might mimic protolith heterogeneity, the heterogeneity in recorded time-integrated fluid flux in Alta dolomites was probably amplified by metamorphic reaction.

Attainment of flow focusing depends on the relative rates of fluid flow, mineral reaction, and compaction. Sluggish reaction kinetics will tend to homogenize the chemical record of fluid flow and permeability because areas of fast fluid flow will be furthest from fluid-rock equilibrium. Also, slow reaction rates will lead to kinetic dispersion which will tend to inhibit flow-focusing (Steefel and Lasaga, 1990). We therefore suggest that the highly heterogeneous distribution of periclase-grade rocks at Alta reflects a close approach to equilibrium for the periclase-forming reaction. Because $\delta^{18}O$ scatter and periclase isograd geometry record a similar flow heterogeneity, oxygen exchange probably also closely approached equilibrium, as argued by Bowman et al. (1994).

Flow focusing will be inhibited if compaction is more efficient at destroying porosity than flow and reaction are at creating it. The highly heterogeneous fluid flow recorded at Alta and Ubehebe suggests that metamorphic fluid flow was fast compared to compaction. The observation that regionally metamorphosed rocks record smaller spatial variations in permeability (e.g., Ferry, 1994a) may reflect

fundamental differences in the relative rates of fluid flow and compaction in contact and regional metamorphic environments.

Chapter 5

CONCLUSIONS

This thesis presents the results of two separate studies: a field-based study of the tectono-thermal evolution of the Selkirk Allochthon, a metamorphosed and deformed welt of supracrustal rocks in the southern Omineca crystalline belt of British Columbia, Canada (Chapters 2 and 3); and a study of the nature of multi-dimensional reactive fluid flow during metamorphism of carbonate rocks, using a comparison of numerically simulated distributions, and natural distributions of mineral assemblages resulting from metamorphic fluid flow (Chapter 4). The salient conclusions of these two studies are summarized here.

Detailed characterization of the distribution of metamorphic mineral assemblages, of the metamorphic reaction history, and of the nature of structural elements related with broadly syn-metamorphic ductile deformation in the Big Fish Creek area of the Selkirk Allochthon leads to the following conclusions:

1. Two distinct metamorphic events affected rocks in study area:

- M1, the earlier event, is recorded by relict porphyroblastic minerals which were subjected to cooling and retrogression prior to development of M2 prograde mineral assemblages. M1 was probably regional in extent.

- M2 is characterized by a Barrovian sequence of metamorphic zones in the study area. From south to north, this field gradient includes the following metamorphic zones in rocks of pelitic composition: chlorite, biotite, garnet + chlorite, staurolite + biotite, kyanite + staurolite. Late-M2 andalusite is widespread in rocks of the garnet + chlorite, and staurolite + biotite zones, suggesting substantial late-M2 decompression.

2. The Bigmouth Creek stock was emplaced in late Middle Jurassic as indicated by magmatic zircon U-Pb ages (157 ● 3.3 Ma). Magmatic epidote in Bigmouth Creek granodiorite suggests that emplacement depth was substantially greater than 20 km. Earliest Cretaceous U-Pb ages (140.7 ± 0.8 Ma, and 137.4 ± 1.4 Ma) from titanite from the granodiorite are interpreted to be due to thermal resetting at that time.

3. Based on evidence for widespread mid-Jurassic metamorphism in other areas of the Selkirk Allochthon, and for deep emplacement of the Bigmouth Creek pluton at that time, M1 metamorphism is interpreted to be of mid-Jurassic age. M2 is interpreted to be the result of the thermal pulse which reset U-Pb systematics of titanite from the Bigmouth Creek pluton in Early Cretaceous time Thus, the timing of M2 metamorphism is Early Cretaceous.

4. Rocks in the area record intense, non-coaxial strain which resulted from long-lived ductile progressive deformation, and involved important components of orogen-transverse and orogen-parallel extension (i.e., shortening normal to the shallow-dipping dominant transposition foliation S_T, which approaches the regional shear plane). These rocks are therefore interpreted to be part of a ductile shear zone of regional significance, herein named the Big Fish Creek shear zone. The presence of this shear zone at intermediate levels in the Selkirk Allochthon illustrates the distributed nature of ductile strain in the Selkirk Allochthon in Mesozoic time.

5. A mid-Jurassic age for M1 metamorphism implies that pre- to syn-metamorphic progressive ductile deformation began at least as early as the Middle Jurassic. Late-M2 decompression at least as late as the Early Cretaceous predates the end of ductile deformation in the area. This puts an Early Cretaceous upper boundary on syn-compressional extension and gravitationally-driven thinning of the Selkirk Allochthon orogenic wedge.

6. Structural and metamorphic evidence for protracted compressional strain, and synchronous, episodically at least, extension and thinning in the present study area, combined with similar interpretations at both higher, and lower structural levels by other workers, suggests that the Selkirk Allochthon constituted a dynamic orogenic wedge from as early as the Middle Jurassic, to at least as late as the Late Cretaceous. The dynamic behavior of this wedge was controlled by far-field forces associated with convergence of accreted terranes and the North American continental margin, by gravitational forces, and by rheological modification and internal deformation of the wedge in response to these different external controls.

Chapter 4 deals with the nature of permeability during metamorphism at mid-crustal levels. A good example of the impact of heterogeneous, and probably temporally evolving fluid flow and permeability in a metamorphic system is offered by the spatially variable extent of retrogression of prograde mineral phases to hydrous assemblages in rocks of the Big Fish Creek area. Work presented in Chapter 4 addresses the question of the spatial variability and the temporal evolution of fluid flow and

permeability in metamorphic terranes and leads to conclusions which may have applicability to the nature of retrogression in the Big Fish Creek area. Major conclusions of the study presented in Chapter 4, of two-dimensional reactive flow in siliceous dolomites are as follows:

1. Numerical models of two-dimensional reactive fluid flow can reproduce the patterns of mineral assemblage distributions observed in natural metamorphic terranes.

2. The spatial heterogeneity of fluid flow predicted from comparison of numerical simulations with natural distributions of mineral assemblages is consistent with that predicted from comparison of natural distributions and numerical simulations of stable isotopic alteration, using the same permeability distribution. This lends support to the applicability of the numerical simulations.

3. Comparison of natural and numerically simulated distributions of mineral assemblages and stable isotopic alteration suggests that the heterogeneity of permeability during metamorphic infiltration of siliceous dolomites in the Alta, Utah contact aureole, was several orders of magnitude larger than the inferred heterogeneity of permeability of the protolith. This suggests that the heterogeneity of hydraulic properties is amplified by fluid flow and reaction during metamorphism.

4. It is proposed that prograde reaction progress, which for most reactions involved in metamorphism of carbonate-rich rocks results in increased porosity, enhances permeability. This, in turn results in increased fluid flow and reaction. Thus, a positive feedback mechanism between infiltration, reaction and permeability enhancement is established which results in progressive focussing of fluid flow into more reactive zones. This has the effect of increasing the spatial heterogeneity of fluid flow inferred from comparison of natural and simulated distributions.

BIBLIOGRAPHY

Alsop, G. I., and R. E. Holdsworth. 1993. The distribution, geometry and kinematic significance of Caledonian buckle folds in the western Moine Nappe, northwestern Scotland. *Geological Magazine* 130: 353-362.

Alsop, G. I., R. E. Holdsworth, and R. A. Strachan. 1996. Transport-parallel cross folds within a mid-crustal Caledonian thrust stack, northern Scotland. *Journal of Structural Geology* 18: 783-790.

Alsop, G. I., R. Bryson, and D. H. W. Hutton. 1998. Ductile transpression and localization of deformation along tectonic boundaries in the Caledonides of northwestern Ireland. *Geological Magazine* 135: 699-718.

Archibald, D.A., J.K. Glover, R.A. Price, E. Farrar, and D.M. Carmichael. 1983. Geochronology and tectonic implications of magmatism and metamorphism, southern Kootenay Arc and neighboring regions, southeastern British Columbia. Part 1: Jurassic to mid-Cretaceous. *Canadian Journal of Earth Sciences* 20: 1891-1913.

Bell, T. H., and M. J. Rubenach. 1983. Sequential porphyroblast growth and crenulation cleavage development during progressive deformation. *Tectonophysics* 92: 171-194.

Bell, T. H. 1985. Deformation partitioning and prophyroblast rotation in metamorphic rocks: a radical reinterpretation. *Journal of Metamorphic Geology* 3: 109-118.

Berman, R. G. 1988. Internally-consistent thermodynamic data for minerals in the system Na_2O - K_2O - CaO - MgO - FeO – Fe_2O_3 - Al_2O_3 - SiO_2 - TiO_2 - H_2O - CO_2. 29: 445-522.

Borradaile, G.J. 1972. Variably oriented co-planar primary folds. *Geological Magazine* 109: 89-98.

Bowman, J.R., S.D. Willett, and S.J. Cook. 1994. Oxygen isotope transport and exchange during fluid flow: one-dimensionsl models and applications. *Americal Journal of Science* 294: 1 - 55.

Brown, R. L., M. J. Perkins, and C. R. Tippett. 1977. Structure and stratigraphy of the Big Bend area, British Columbia. *Report of Activities, Part A*, Geological Survey of Canada Paper 77-1A: 273-275.

Brown, R. L., C. R. Tippett, and L. S. Lane. 1978. Stratigraphy, facies changes, and correlations in the northern Selkirk Mountains, southern Canadian Cordillera. *Canadian Journal of Earth Sciences* 15: 1129-1140.

Brown, R. L., and C. R. Tippett. 1978. The Selkirk fan structure of the southeastern Canadian Cordillera. *Geological Society of America Bulletin* 89: 548-558.

Brown, R. L., and P.B. Read. 1983. Shuswap terrane of British Columbia: A Mesozoic "core complex". *Geology* 11: 164-168.

Brown, R. L., J. M. Journeay, L. S. Lane, D. C. Murphy, and C. J. Rees. 1986. Obduction, backfolding and piggyback-thrusting in the metamorphic hinterland of the southeastern Canadian Cordillera. *Journal of Structural Geology* 8: 255-268.

Brown, R. L., and J. M. Journeay. 1987. Tectonic denudation of the Shuswap metamorphic terrane of southeastern British Columbia. *Geology* 15: 142-146.

Brown, R.L., and L.S. Lane. 1988. Tectonic interpretation of west-verging folds in the Selkirk Allochthon of the southern Canadian Cordillera. *Canadian Journal of Earth Sciences* 25: 292-300.

Brown, R.L., V.J. McNicoll, R.R. Parrish, and R.J. Scammell. 1992a. Middle Jurassic plutonism in the Kootenay Terrane, northern Selkirk Mountains, British Columbia. *Radiogenic Age and Isotopic Studies,* Geological Survey of Canada Paper 91-2: 135-141.

Brown, R.L., S.D. Carr, B.J. Johnson, V.J. Coleman, F.A. Cook, and J.L Varsek. 1992b. The Monashee decollement of the southern Canadian Cordillera: a crustal-scale shear zone linking the Rocky Mountain Foreland belt to the lower crust beneath accreted terranes. In *Thrust Tectonics*. Edited by K. R. McClay. 357-364. Chapman&Hall.

Brown, R.L., C. Beaumont, and S.D. Willett. 1993. Comparison of the sSelkirk Fan structure with mechanical models - implications for interpretation of the southern Canadian Cordillera. *Geology* 21: 1015-1018.

Bryant, B., and J. Reed. 1969. Significance of lineation and minor folds near major thrust faults in the southern Appalachians and the British and Norwegian Caledonides. *Geological Magazine* 106: 412-429.

Burchfield, B. C., and L. H. Royden. 1985. North-south extension within the convergent Himalayan region. *Geology* 13: 679-682.

Butler, R. H. 1982. Hangingwall strain: a function of duplex shape and footwall topography. *Tectonophysics* 88: 235-246.

Carmichael, D.M. 1970. Intersecting isograds in the Whetstone Lake area, Ontario. *Journal of Petrology* 11: 147-181.

Carr, S.D. 1991. Three crustal zones in the Thor Odin Pinnacles area, southern Omineca Belt, British-Columbia. *Canadian Journal Of Earth Sciences* 28: 2003-2023.

Carr, S.D. 1992. Tectonic setting and U-Pb geochronology of the Early Tertiary Ladybird leucogranite suite, Thor-Odin - Pinnacles area, southern Omineca Belt, British-Columbia. *Tectonics* 11: 258-278.

Cartwright, I. 1994. The two-dimensional pattern of metamorphic fluid flow at Mary Kathleen, Australia: Fluid focusing, transverse dispersion, and implications for modeling fluid flow. *American Mineralogist* 79: 526-535.

Cobbold, P. R., and H. Quinquis. 1980. Development of sheath folds in shear regimes. *Journal of Structural Geology* 2: 119-126.

Colpron, M., R.A. Price, D.A. Archibald, and D.M. Carmichael. 1996. Middle Jurassic exhumation along the western flank of the Selkirk Fan structure - thermobarometric and thermochronometric constraints from the Illecillewaet Synclinorium, southeastern British Columbia. *Geological Society Of America Bulletin* 108: 1372-1392.

Colpron, M., M. J. Warren, and R. A. Price. 1998. Selkirk fan structure, southeastern Canadian Cordillera: Tectonic wedging against an inherited basement ramp. *Geological Society of America Bulletin* 110: 1060-1074.

Cook, F.A., J.L. Varsek, R.M. Clowes, E.R. Kanasewich, C.S. Spencer, R.R. Parrish, R.L. Brown, S.D. Carr, B.J. Johnson, and R.A. Price. 1992. Lithoprobe crustal reflection cross section of the southern Canadian Cordillera .1. Foreland thrust and fold belt to Fraser River fault. *Tectonics* 11: 12-35.

Cook, S.J. 1992. Contact metamorphism surrounding the Alta Stock, Little Cottonwood Canyon, Utah. Ph.D., University of Utah.

Cook, S. J., J. R. Bowman, and C. B. Forster. 1997. Contact metamorphism surrounding the Alta stock: Finite element model simulation of heat- and $^{18}O/^{16}O$ mass transport during prograde metamorphism. *American Journal of Science* 297: 1-55.

Coward, M. P., and G. J. Potts. 1983. Complex strain patterns developed at the frontal and lateral tips to shear zones and thrust zones. *Journal of Structural Geology* 5: 383-399.

Craig, J., W.R. Fitches, and A.J. Maltman. 1982. Chlorite-mica stacks in low-strain rocks from Central Wales. *Geological Magazine* 119: 243-256.

Crowley, J.L., E.D. Ghent, S.D. Carr, and P.S. Simony. 1998. U-Pb geochronological evidence for Late Jurassic and Late Cretaceous thermal events in the northern Monashee and Selkirk Mountains, Mica Creek area, B.C. In *Proceedings of the Slave-Northern Cordilleran Lithospheric Evolution (SNORCLE) Transect and Cordilleran Tectonics Workshop Meeting*. Edited by F. Cook and P. Erdmer. 243-244. Vancouver, Canada.

Crowley, J.L., E.D. Ghent, S.D. Carr, M.A. Hamilton,, and P.S. Simony, 1999. U-Th-Pb geochronologic constraints on diachronous metamorphism and deformation in the Mica Creek area, southeastern Canadian Cordillera. In *Proceedings of the Slave-Northern Cordilleran Lithospheric Evolution (SNORCLE) Transect and Cordilleran Tectonics Workshop Meeting*. Edited by F. Cook and P. Erdmer. 192. Calgary, Canada.

Currie, L.D. 1988. Geology of the Allen Creek area, Cariboo Mountains, British Columbia. M.Sc., University of Calgary.

Dahlen, F. A., J. Suppe, and D. Davis. 1984. Mechanics of fold-and-thrust belts and accretionary wedges: cohesive Coulomb theory. *Journal of Geophysical Research* 89: 10087-10101.

Dahlen, F. A. 1984. Non-cohesive critical Coulomb wedges: an exact solution. *Journal of Geophysical Research* 89: 10125-10133.

Davis, D., J. Suppe, and F. A. Dahlen. 1983. Mechanics of fold-and-thrust belts and accretionary wedges. *Journal of Geophysical Research* 88: 1153-1172.

de Marsily, G. 1986. *Quantitative hydrogeology: Groundwater hydrology for engineers*. Orlando, Florida: Academic Press.

Dechesne, R. G., and P. S. Simony. 1984. Structural evolution and metamorphism of the southern Cariboo Mountains near Blue River, British Columbia. *Current Research, Part A*, Geological

Survey of Canada Paper 84-1A: 91-94.

Deutsch, C. V., and A. G. Journel. 1992. *GSLIB: Geostatistical software library and user's guide.* New York: Oxford University Press.

Diez Balda, M. A., J. R. Martinez Catalan, and P. Ayarza Arribas. 1995. Syn-collisional extensional collapse parallel to the orogenic trend in a domain of steep tectonics: the Salamanca Detachment Zone (Central Iberian Zone, Spain). *Journal of Structural Geology* 17: 163-182.

Digel, S.G., E.D. Ghent, and P.S Simony. 1989. Metamorphism and structure of the Mount Cheadle area, Monashee Mountains, British Columbia. *Current Research, Part E,* Geological Survey of Canada Paper 89-1E: 95-100.

Digel, S.G, E.D. Ghent, S.D. Carr, and P.S. Simony. 1998. Early Cretaceous kyanite-sillimanite metamorphism and Paleocene sillimanite overprint near Mt. Cheadle, southeastern British Columbia: geometry, geochronology, and metamorphic implications. *Canadian Journal of Earth Sciences* 35: 1070-1087.

Dipple, G.M., and J.M. Ferry. 1996. The effect of thermal history on the development of mineral assemblages during infiltration-driven contact metamorphism. *Contributions to Mineralogy and Petrology* 124: 334-345.

Doucet, P., E.D. Ghent, and P.S. Simony. 1985. Metamorphism in the Monashee Mountains east of Blue River, British Columbia. *Current Research, Part A,* Geological Survey of Canada Paper 85-1A: 69-71.

England, P.C., and A. B. Thompson. 1984. Pressure - temperature - time paths of regional metamorphism, Part I: Heat transfer during the evolution of regions of thickened continental crust. *Journal of Petrology* 25: 894-928.

Escher, A., and J. Watterson. 1974. Stretching fabrics, folds and crustal shortening. *Tectonophysics* 22: 223-231.

Ferry, J. M. 1984. A biotite isograd in south-central Maine, U. S. A.: mineral reactions, fluid transfer, and heat transfer. *Journal of Petrology* 25: 871-893.

Ferry, J.M. 1994. Overview of the petrologic record of fluid flow during regional metamorphism in northern New England. *American Journal of Science* 294: 905-988.

Ferry, J.M. 1994. Role of fluid flow in the contact metamorphism of siliceous dolomitic limestones. *American Mineralogist* 79: 719-736.

Franzen, J.P. 1974. Structural analysis in the Selkirk fan axis near Argonaut Mountain, Southeastern British Columbia. M.Sc., Carleton University.

Gal, L.P., and E.D. Ghent. 1990. Metamorphism in the Solitude Range, southwestern Rocky Mountains, British Columbia: comparison with adjacent Omineca Belt rocks and tectonometamorphic implications for the Purcell Thrust. *Canadian Journal of Earth Sciences* 27: 1511-1520.

Gelhar, L.W. 1986. Stochastic subsurface hydrology from theory to applications. *Water Resources Research* 22: 135s - 145s.

Gerdes, M.L., L.P. Baumgartner, and M. Person. 1995. Stochastic permeability models of fluid flow during contact metamorphism. *Geology* 23: 945-948.

Ghent, E.D., P.S. Simony, W. Mitchell, J. Perry, D. Robbins, and J. Wagner. 1977. Structure and metamorphism in southeast Canoe River area, British Columbia. *Report of Activity, Part C,* Geological Survey of Canada 77-1C:

Ghent, E. D., D. B. Robbins, and M. Z. Stout. 1979. Geothermometry, geobarometry and fluid compositions of metamorphosed calc-silicates and pelites, Mica Creek, British Columbia. *American Mineralogist* 64: 874-885.

Ghent, E.D., P.S. Simony, and C.C. Knitter. 1980. Geometry and pressure-temperature significance of kyanite-sillimanite isograd in the Mica Creek area, British Columbia. *Contributions to Mineralogy and Petrology* 74: 67-73.

Ghent, E.D., C.C. Knitter, R.P. Raeside, and M.Z. Stout. 1982. Geothermometry and geobarometry of pelitic rocks, upper kyanite and sillimanite zones, Mica Creek area, British Columbia. *Canadian Mineralogist* 20: 295-305.

Ghent, E.D., M.Z. Stout, and R.P. Raeside. 1983. Plagioclase-clinopyroxene-garnet-quartz equilibria and the geobarometry and geothermometry of garnet amphibolites from Mica Creek, British Columbia. *Canadian Journal of Earth Sciences* 20: 699-706.

Ghent, E.D., J. Nicholls, P.S. Simony, J.H. Sevigny, and M.Z. Stout, 1991. Hornblende geobarometry of the Nelson batholoth, southeastern British Columbia: Tectonic implications. *Canadian Journal of Earth Sciences* 28: 1982-1991.

Gibson, G., and T. Höy. 1985. Rift, a zinc-lead massive sulphide deposit in southeastern British Columbia *Geological Fieldwork 1984,* British Columbia Ministry of Energy, Mines and Petroleum Resources Paper 1985-1: 105-119.

Grujic, D., and N.S. Mancktelow. 1995. Folds with axes parallel to the extension direction: an experimental study. *Journal of structural geology* 17: 279-291.

Hanmer, S., and C. W. Passchier. 1991. *Shear sense indicators: A review.* Geological Survey of Canada. NTIS, Paper 90-117.

Hobbs, B. E. 1965. Structural analysis of the rocks between the Wyangala batholith and the Copperhannia thrust, New South Wales. *Journal of the Geological Society of Australia* 12: 1-24.

Hobbs, B. E., W. D. Means, and P. F. Williams. 1976. *An outline of structural geology.* John Wiley& Sons.

Hodges, K. V., and J. D. Walker. 1992. Extension in the Cretaceous Sevier orogen, North American Cordillera. *Geological Society of America Bulletin* 104: 560-569.

Hodges, K. V., B. C. Burchfield, L. H. Royden, Z. Chen, and Y. Liu. 1993. The metamorphic signature of contemporaneous extension and shortening in the central Himalayan orogen: data from the Nyalam transect, southern Tibet. *Journal of Metamorphic Geology* 11: 721-737.

Holdsworth, R.E. 1989. The geology and the structural evolution of a Caledonian fold and ductile thrust

zone, Kyle of Tongue region, Sutherland, northern Scotland. *Journal of the Geological Society* 146: 809-823.

Holdsworth, R. E., and C. J. Grant. 1990. *Convergence-related 'dynamic spreading' in a mid-crustal ductile thrust zone: a possible orogenic wedge model.* In *Deformation mechanisms: rheology and teconics.* Edited by R. J. Knipe and E. H. Rutter. 491-500.

Jamieson, R. A., and C. Beaumont. 1988. Orogeny and metamorphism: a model for deformation and pressure-temperature-time paths with applications to the central and southern Appalachians. *Tectonics* 7: 417-445.

Johnston, D. H. 1996. Structural and thermal evolution of northwest Thor-Odin dome, Monashee Complex, southeast British Columbia. Ph.D., University of New Brunswick.

Journeay, M., and R. L. Brown. 1986. Major tectonic boundaries of the Omineca Belt in southern British Columbia. *Current Research, Part A, Geological Survey of Canada* Paper 86-1A: 81-88.

Journeay, J. M. 1986. Stratigraphy, internal strain and thermo-tectonic evolution of northern Frenchman Cap dome: An exhumed duplex structure. Ph.D., Queen's University.

Kerrick, D.M. 1987. Fibrolite in contact aureoles of Donegal, Ireland. *American Mineralogist* 72: 240-254.

King, B. C., and N. Rast. 1956. The small-scale structures of south-eastern Cowal, Argyllshire. *Geological Magazine* 93: 185-195.

Lane, L. S., E. D. Ghent, M. Z. Stout, and R. L. Brown. 1989. P-T history and kinematics of the Monashee Décollement near Revelstoke, British Columbia. *Canadian Journal of Earth Sciences* 26: 231-243.

Leatherbarrow, R.W. 1981. Metamorphism of pelitic rocks from the northern Selkirk Mountains, southeastern British Columbia. Ph.D., Carleton University.

Lister, G. S., and P. F. Williams. 1983. The partitioning of deformation in flowing rock masses. *Tectonophysics* 92: 1-33.

Lister, G. S., and A. W. Snoke. 1984. S-C mylonites. *Journal of Structural Geology* 6: 617-638.

Logan, J. M., and M. Colpron. 1995. Northern Selkirk project- geology of the Goldstream River map area (82M/9 and parts of 82M/10). *Geological Fieldwork 1994,* British Columbia Ministry of Energy, Mines and Petroleum Resources Paper 1995-1: 215-241.

Malavieille, J. 1984. Modélisation expérimentale des chevauchements imbriqués: application aux chaînes de montagnes. *Bulletin de la Société Géologique de France* 26: 129-138.

Marchildon, N., and G. M. Dipple. 1998. Irregular isograds, reaction instabilities, and the evolution of permeability during metamorphism. *Geology* 26: 15-18.

Mawer, C. K., and P. F. Williams. 1991. Progressive folding and foliation development in a sheared, coticule-bearing phyllite. *Journal of Structural Geology* 13: 539-555.

McNicoll, V.J., and R.L. Brown. 1995. The Monashee Décollement At Cariboo Alp, Southern Flank Of The Monashee Complex, Southern British Columbia, Canada. *Journal Of Structural Geology* 17: 17-30.

Means, W. D. 1981. The concept of steady-state foliation. *Tectonophysics* 78: 179-199.

Monger, J. W. H., R. A. Price, and D. J. Templeman-Kluit. 1982. Tectonic accretion and the origin of two major metamorphic and plutonic welts in the Canadian Cordillera. *Geology* 10: 70-75.

Moore, J.N., and D.M. Kerrick. 1976. Equilibria in siliceous dolomites of the Alta aureole, Utah. *American Journal of Science* 276: 502-524.

Murphy, D. C., and J. M. Journeay. 1982. Structural style in the Premier Range, Cariboo Mountains, southern British Columbia: Preliminary results. *Current Research, Part A*, Geological Survey of Canada Paper 82-1A: 289-292.

Northrup, C. J., and B. C. Burchfield. 1996. Orogen-parallel transport and vertical partitionning of strain during oblique collision, Efjorden, north Norway. *Journal of Structural Geology* 18: 1231-1244.

Olesen, N., and K. Sorensen. 1972. Caledonian fold- and fabric-elements: a model. In *Proceedings of the International Geological Congress*. p. 93-94. Montreal:

Ortoleva, P., J. Chadam, E. Merino, and A. Sen. 1987. Geochemical self-organization II: The reactive-infiltration instability. *American Journal of Science* 287: 1008-1040.

Park, R.G. 1969. Structural correlation in metamorphic belts. *Tectonophysics* 7: 323-338.

Parrish, R. R., S. D. Carr, and D. L. Parkinson. 1988. Eocene extensional tectonics and geochronology of the southern Omineca Belt, British Columbia and Washington. *Tectonics* 7: 181-212.

Parrish, R.R. 1995. Thermal evolution of the southeastern Canadian Cordillera. *Canadian Journal of Earth Sciences* 32: 1618-1642.

Passchier, C. W. 1986. Mylonites in the continental crust and their role as seismic reflectors. *Geologie en Mijnbouw* 65: 167-176.

Perkins, M.J. 1983. Structural geology and stratigraphy, Big Bend of the Columbia River, Selkirk Mountains, B.C. Ph.D., Carleton University.

Platt, J. P., and . R. L. M. Vissers. 1980. Extensional structures in anisotropic rocks. *Journal of Structural Geology* 2: 397-410.

Price, R. A., and E. W. Mountjoy. 1970. Geologic structure of the Canadian Rocky Mountains between Bow and Athabasca rivers - a progress report. In *Structure of the southern Canadian Cordillera*. Edited by J. O. Wheeler. 7-25. Geological Association of Canada.

Price, R. A. 1986. The southeastern Canadian Cordillera: Thrust faulting, tectonic wedging, and delamination of the lithosphere. *Journal of Structural Geology* 8: 239-354.

Raeside, R. P., and P. S. Simony. 1983. Stratigraphy and deformational history of the Scrip Nappe, Monashee Mountains, British Columbia. *Canadian Journal of Earth Sciences* 20: 639-650.

Ramsay, D. M., and B. A. Sturt. 1970. Polyphase deformation of a polymict Silurian conglomerate from Magerōy, Norway. *Journal of Geology* 78: 264-280.

Ramsay, D. M. 1979. Analysis of rotation of folds during progressive deformation. *Geological Society of America Bulletin* 90: 732-738.

Rattey, P. R., and D. J. Sanderson. 1982. Patterns of folding within nappes and thrust sheets: examples from the Variscan of southwest England. *Tectonophysics* 88: 247-267.

Read, P. B., and R. L. Brown. 1979. Inverted stratigraphy and structures, Downie Creek, southern British Columbia. *Current Research, Part A,* Geological Survey of Canada Paper 79-1A: 33-34.

Read, P. B., and R. L. Brown. 1981. Columbia River fault zone: southeaster margin of the Shuswap and Monashee complexes, southern British Columbia. *Canadian Journal of Earth Sciences* 18: 1127-1145.

Reesor, J.E., 1973. *Geology of the Lardeau map-area, east half, British Columbia.* Geological Survey of Canada memoir 369.

Rice, H.M.A, 1941. *Nelson map-area, east half, British Columbia.* Geological Survey of Canada memoir 228.

Roberts, J. L., and D. J. Sanderson. 1974. Oblique fold axes in the Dalradian rocks of the southwest Highlands. *Scottish Journal of Geology* 9: 281-296.

Roberts, J. L. 1977. The structural analysis of metamorphic rocks in orogenic belts. In *Energetics of geological processes*. Edited by S. K. Saxena and S. Bhattacharji. 151-168. New York: Spring-Verlag.

Roselle, G. T. 1997. Integrated petrologic, stable isotopic, and statistical study of fluid flow in carbonates of the Ubehebe Peak contact aureole, Death Valley National Park, California. Ph.D., University of Wisconsin, Madison.

Rumble, D., III, J.M. Ferry, T.C. Hoering, and A.J. Boucot. 1982. Fluid flow during metamorphism at the Beaver Brook fossil locality, New Hampshire. *American Journal of Science* 282: 886-919.

Sanderson, D. 1973. The development of folds axes oblique to the regional trend. *Tectonophysics* 16: 55-70.

Scammell, R.J. 1993. Mid-Cretaceous to Tertiary thermotectonic history of former mid-crustal rocks, southern Omineca belt, Canadian Cordillera. Ph.D., Queen's University.

Schaubs, P. M., and S. D. Carr. 1998. Geology of metasedimentary rocks and Late Cretaceous deformation history in the northern Valhalla complex, British Columbia. *Canadian Journal of Earth Sciences* 35: 1018-1036.

Sevigny, J.H., and E.D. Ghent. 1986. Metamorphism in the northern Adams River area, northeastern Shuswap Complex, Monashee Mountains, British Columbia. *Current Research, Part B,* Geological Survey of Canada Paper 86-1B: 693-698.

Sevigny, J. H., and P. S. Simony. 1989. Geometric relationship between the Scrip Nappe and

metamorphic isograds in the northern Adams River area, Monashee Mountains, British Columbia. *Canadian Journal of Earth Sciences* 26: 606-610.

Sevigny, J.H., R.R. Parrish, and E.D. Ghent. 1989. Petrogenesis of peraluminous granites, Monashee Mountains, southeastern Canadian Cordillera. *Journal of Petrology* 30: 557-581.

Sevigny, J.H., and E.D. Ghent. 1989. Pressure, temperature and fluid composition during amphibolite facies metamorphism of graphitic metapelites, Howard Ridge, British-Columbia. *Journal Of Metamorphic Geology* 7: 497-505.

Sevigny, J.H., R.R. Parrish, R.A. Donelick, and E.D. Ghent. 1990. Northern Monashee Mountains, Omineca Crystalline Belt, British-Columbia - timing of metamorphism, anatexis, and tectonic denudation. *Geology* 18: 103-106.

Simony, P. S., and G. Wind. 1970. Structure of the Dogtooth Range and adjacent portions of the Rocky Mountain Trench. In *Structure of the southern Canadian Cordillera*. Edited by J. O. Wheeler. 41-51. Geological Association of Canada.

Simony, P.S., E.D. Ghent, D. Craw, W. Mitchell, and D.B. Robbins. 1980. Structural and metamorphic evolution of the northeast flank of Shuswap complex, southern Canoe River area, British Columbia. In *Structure of the southern Canadian Cordillera*. 445-461. Geological Society of America.

Simpson, C. , and S. M. Schmid. 1983. An evaluation of criteria to determine the sense of movement in sheared rocks. *Geological Society of America Bulletin* 94: 1281-1288.

Smith, R.K. 1972. The mineralogy and petrology of the contact metamorphic aureole around the Alta stock, Utah. Ph.D., University of Iowa.

Spear, F. S. , and J. T. Cheney. 1989. A petrogenetic grid for pelitic schists in the system SiO_2 – Al_2O_3 - FeO - MgO - K_2O - H_2O. 101: 149-164.

Spear, F.S. 1993. *Metamorphic phase equilibria and pressure-temperature-time paths*. Mineralogical Society of America Monograph. Washington: Mineralogical Society of America.

Steefel, C.I., and A.C. Lasaga. 1990. Evolution of dissolution patterns: Permeability change due to coupled flow and reaction. In *Chemical Modeling of Aqueous Systems*. Edited by D. C. Melchior and R. L. Bassett. 212-225. Washington, D.C.: American Chemical Society.

Stockmal, G.S., C. Beaumont, and R. Boutilier. 1986. Geodynamic models of convergent margin tectonics: consequences for foreland basin development. *American Association of Petroleum Geologists Bulletin* 70: 181-190.

Symmes, G.H., and J.M. Ferry. 1991. Evidence from mineral assemblages for infiltration of pelitic schists by aqueous fluids during metamorphism. *Contributions to Mineralogy and Petrology* 108: 419-438.

Thompson, J. B., Jr. 1957. The graphical analysis of mineral assemblages in pelitic schists. *American Mineralogist* 42: 842-858.

Thompson, A. B., K. Schulmann, and J. Jezek. 1997. Extrusion tectonic and elevation of lower crustal

metamorphic rocks in convergent orogens. *Geology* 25: 491-494.

Tippett, C. R. 1976. A structural and stratigraphic cross-section through the Selkirk Fan Axis, Selkirk Mountains, southeastern British Columbia. M.Sc., Carleton University.

Tobisch, O. T., and S. R. Paterson. 1988. Analysis and interpretation of composite foliations in areas of progressive deformation. *Journal of Structural Geology* 10: 745-754.

Tobisch, O. T., and S. R. Paterson. 1990. The Yarra Granite; an intradeformational pluton associated with ductile thrusting, Lachlan fold belt, southeastern Australia. *Geological Society of America Bulletin* 101: 693-703.

Tullis, J., and R. A. Yund. 1987. Transition from cataclastic flow to dislocation creep of feldspar: Mechanisms and microstructures. *Geology* 15: 606-609.

Twiss, R. J., and E. M. Moores. 1992. *Structural Geology*. New York: Freeman.

Van der Leeden, J. 1976. Stratigraphy, structure and metamorphism in the northern Selkirk Mountains southwest of Argonaut Mountain, southeastern British Columbia. M.Sc., Carleton University.

Veblen, D.R., and J.M. Ferry. 1983. A TEM study of the biotite-chlorite reaction and comparison with petrologic observations. *American Mineralogist* 68: 1160-1168.

Wang, P., and F.S. Spear. 1991. A field and theoretical analysis of garnet + chlorite + chloritoid + biotite assemblages from the tri-state (MA, CT, NY) area, USA. *Contributions to Mineralogy and Petrology* 106: 217-235.

Wheeler, J. O. 1963. *Rogers Pass map-area, British Columbia and Alberta*. Geological Survey of Canada, Paper 62-32.

Wheeler, J.O. 1965. *Big Bend map area, British Columbia (82M East half)*, Geological Survey of Canada, 64-32.

Wheeler, J. O., and P. McFeely. 1991. *Tectonic assemblage map of the Canadian Cordillera and adjacent parts of the United States of America*. Geological Survey of Canada, Map 1712A, 1:2 000 000.

Whitney, D.L., and E.D. Ghent. 1993. Prograde reactions and garnet zoning reversals in staurolite schist, British Columbia - significance for thermobarometric interpretations. *Journal Of Metamorphic Geology* 11: 779-788.

Willett, S., C. Beaumont, and P. Fullsack. 1993. Mechanical model for the tectonics of doubly vergent compressional orogens. *Geology* 21: 371-374.

Williams, P. F. 1967. Structural analysis of the Little Broken Hill area, New South Wales. *Journal of the Geological Society of Australia* 14: 317-331.

Williams, P. F. 1972. Development of metamorphic layering and cleavage in low grade metamorphic rocks at Bermagui, Australia. *American Journal of Science* 272: 1-47.

Williams, P.F., and H.J. Zwart. 1977. A model for the development of the Seve-Koli Caledonian nappe complex. In *Energetics of geological processes*. Edited by S. K. Saxena and S. Bhattacharji. 169-

187. New York: Springer-Verlag.

Williams, P. F. 1983. Large scale transposition by folding in Northern Norway. *Geologische Rundschau* 72: 589-604.

Williams, P.F., and R. Campagnoni. 1983. Deformation and metamorphism in the Bard area of the Sesia Lanzo zone, Western Alps, during subduction and uplift. *Journal of Metamorphic Geology* 1: 117-140.

Williams, P. F. 1985. Multiply deformed terrains - problems of correlation. *Journal of Structural Geology* 7: 269-280.

Williams, P. F., and D. Jiang. 1999. The Omineca Belt: a crustal scale shear zone or a zone of thrusting? In *Proceedings of the Slave-Northern Cordilleran Lithospheric Evolution (SNORCLE) Transect and Cordilleran Tectonics Workshop Meeting*. Edited by F. Cook and P. Erdmer. Calgary, Canada:

Zen, E., and J. M. Hammarstrom. 1984. Magmatic epidote and its petrologic significance. *Geology* 12: 515-518.

Zen, E. 1985. Implications of magmatic epidote-bearing plutons on crustal evolution in the accreted terranes of northwestern North America. *Geology* 13: 266-269.

Appendix I: Photographic Plates

Plate 1 Garnet morphology and evidence for two prograde garnet growth episodes separated by retrogression. **A.** Sample 94-NM-75B, M2 staurolite + biotite zone. Garnet porphyroblast showing a dominant, anhedral inclusion-rich core, and thin, euhedral rim. Note rind of more or less randomly oriented biotite flakes around bottom part of grain, which is overgrown by inclusion-poor garnet. Plane polarized light; width of field is 6 mm. **B.** Sample 94-NM-111B, M2 staurolite + biotite zone. The two garnet grains are within the same strain shadow and probably represent two clasts from an original grain. The core portions of these grains are anhedral and relatively inclusion-rich whereas the rims are inclusion-poor and euhedral to subhedral. Euhedral rims overgrow biotite + chlorite + quartz + plagioclase mass developed as a result of retrogression of early inclusion-rich garnet represented by the anhedral cores. Also note that where small staurolite porphyroblasts are developed around the garnet, the inclusion-poor garnet rim is less euhedral. Elemental composition maps and a quantitative compositional profile of the left grain are presented in Plate 2A, and Figure 2.3, respectively. Plane polarized light; width of field is 1 cm. **C.** Sample 94-NM-85C, M2 garnet zone. Partially chloritized inclusion-rich garnet porphyroblast. The chlorite ± quartz ± plagioclase ● biotite rind around the porphyroblast outlines its original shape. Note that biotite seems to be developed preferentially outboard of the chlorite-rich rind. Some of this biotite may have grown during M2 and be prograde. No euhedral rim is present on garnet. Also note that matrix foliation deflects around the original garnet outline, and that inclusion trails in the porphyroblast are inclined with respect to this foliation. Plane polarized light; width of field is 6 mm. **D.** Sample 94-NM-71A, M2 garnet zone. Garnet porphyroblast completely pseudomorphed by chlorite + biotite + quartz ± plagioclase aggregate. Some of the biotite may have grown during M2 and be prograde. Outline of original porphyroblast is still visible and matrix foliation gently deflects around it. Plane polarized light; width of field are 6 mm. Note: anomalous colours are an artifact of printing.

Plate 1

Plate 2 Elemental composition maps of composite garnet. **A.** Sample 94-NM-111B, M2 staurolite + biotite zone. This is the left grain shown on Plate 1B, and a quantitative compositional profile is shown in Figure 2.3. **B.** Sample 94-NM-71B, M2 staurolite + biotite zone. Scale bars are 50 μm. Note: anomalous colours are an artifact of printing.

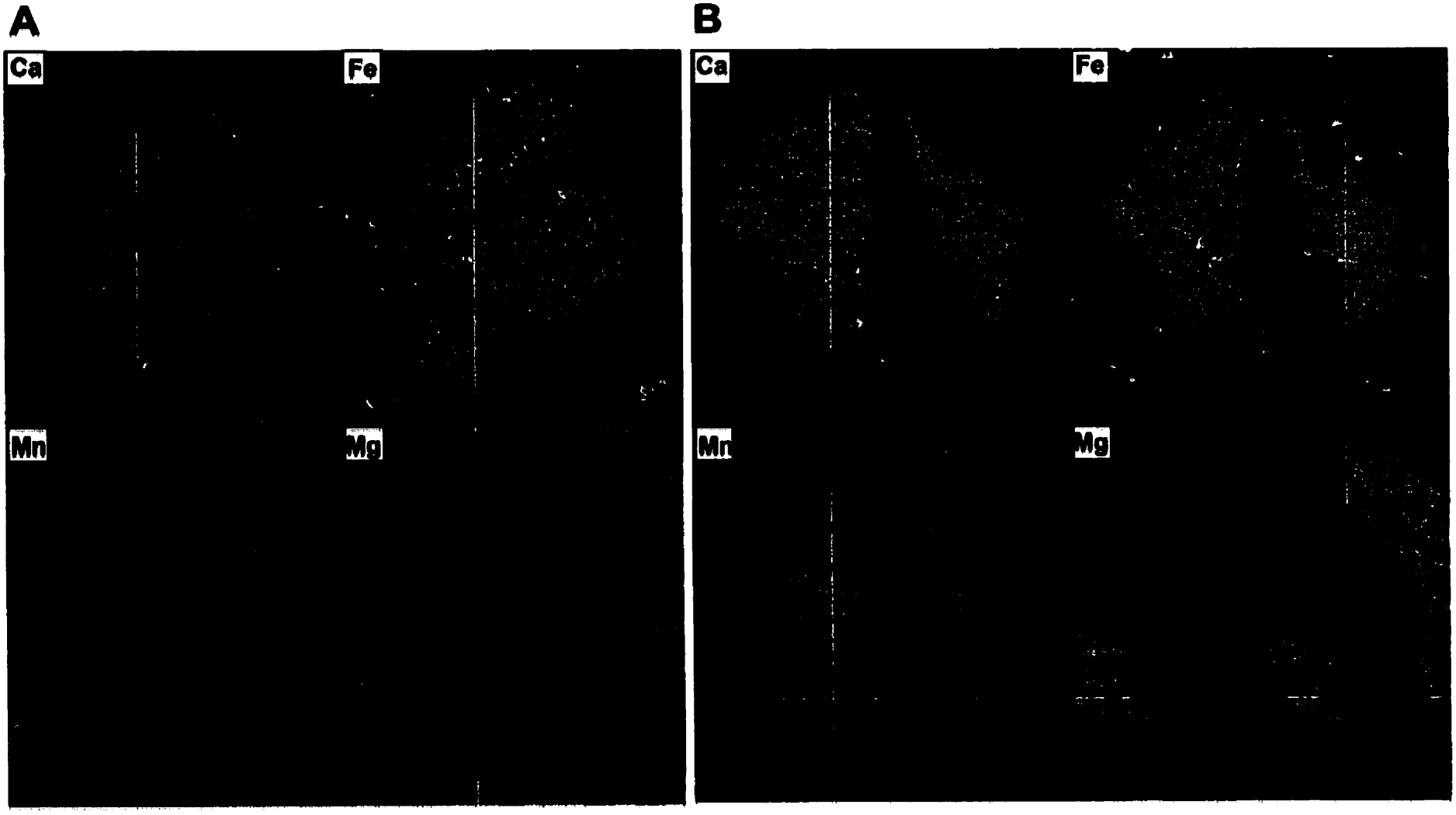

Plate 2

Plate 3 Chlorite-zone, and biotite-zone textures. **A.** Sample 94-NM-45B, chlorite zone. Dominant foliation is defined by chlorite + muscovite-rich laminae and quartzose microlithons. Note waviness resulting from gentle crenulation of dominant foliation. Width of field is 3 mm. **B.** Sample 94-NM-2ME, chlorite zone. Syn-crenulation chlorite porphyroblast. Inclusion trails in the porphyroblasts define a foliation, S_i, which is more gently crenulated than the dominant matrix foliation, S_e (dominant foliation is sub-horizontal, and the crenulation dips to the left). Width of field is 6 mm. **C.** Sample 94-NM-48G, low-grade portion of M2 biotite zone. Three foliations are present: a dominant crenulation cleavage (S_{cc}); an earlier, extensively transposed continuous cleavage (S_c) preserved as recrystallized, folded muscovite in microlithons; and a late crenulation (S_{cr}) which is well developed only in some laminae. Biotite occurs primarily as fine-grained flakes within chlorite + biotite clots (arrow). Width of field is 6 mm. **D.** Sample 94-NM-118B, high-grade portion of M2 biotite zone. Large, irregularly oriented biotite flakes. Note that the foliation, S_i, defined by inclusion trails in these porphyroblasts is not regular from grain to grain, and does not parallel either of two external foliations, a continuous cleavage (S_c), and a crenulation (S_{cr}). These spatial relationships are explored in detail in Chapter 3. Width of field is 6 mm. Note: anomalous colours are an artifact of printing. Note: anomalous colours are an artifact of printing.

Plate 3

Plate 4 M2 mineral textures, staurolite + biotite zone. **A.** Outcrop 96-NM-226. Fresh staurolite locally forming crosses, occurring in staurolite + biotite intergrowth over garnet porphyroblasts. Also present are discrete staurolite porphyroblasts in groundmass away from staurolite + biotite clots after garnet. Coin is 2.3 cm in diameter. **B.** Outcrop 94-NM-101. Muscovite ● chlorite pseudomorphs after coarse andalusite porphyroblasts defining a "chickenfeet" texture. Lens cap is 6 cm in diameter. **C, D.** Sample 96-NM-214K. Euhedral staurolite porphyroblast partially included in poikiloblastic andalusite; C. plane-polarized light; D. cross-polarized light. Width of field is 6 mm. Note: anomalous colours are an artifact of printing.

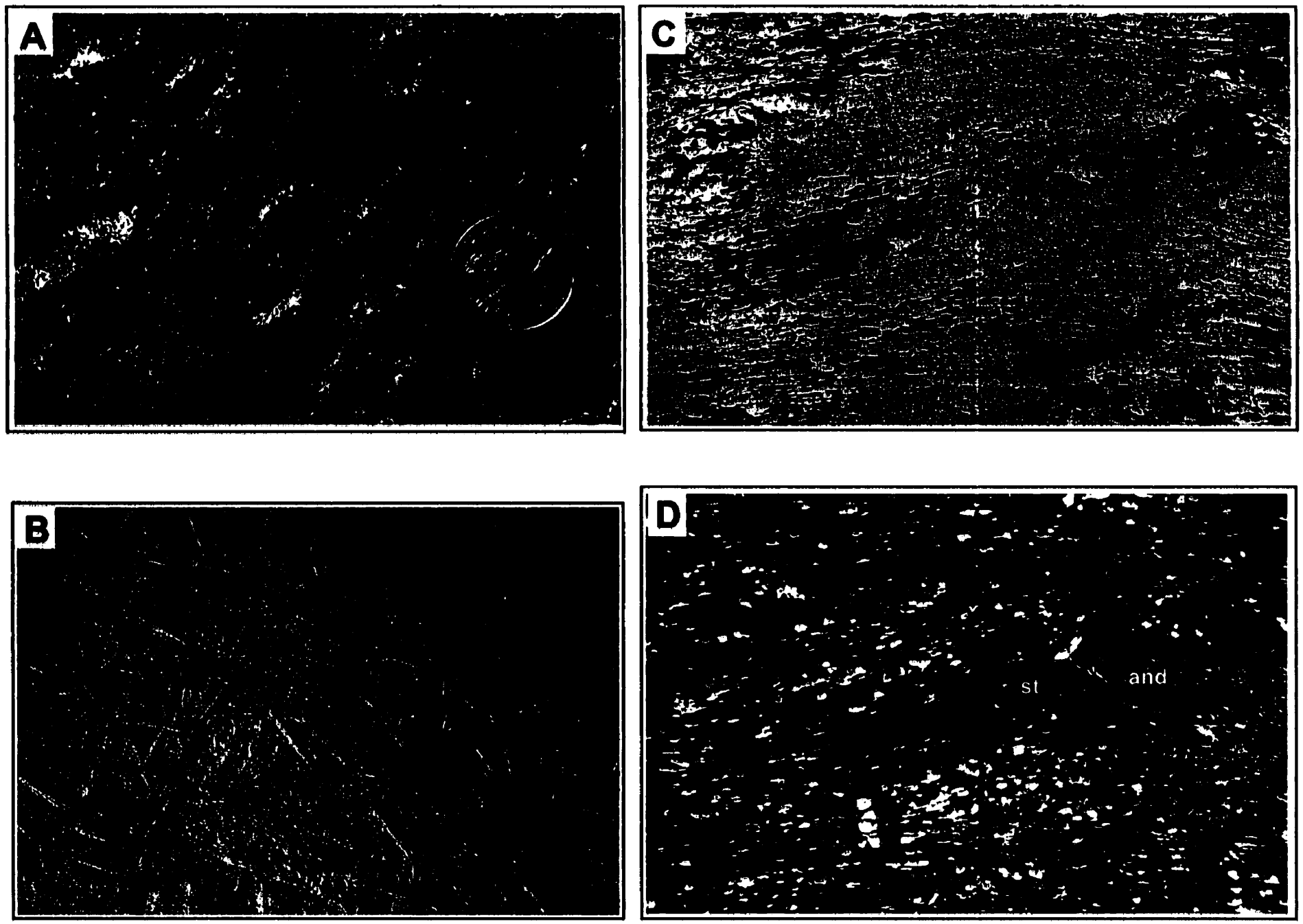

III

Plate 4

Plate 5 M2 mineral textures, staurolite + biotite zone and kyanite + staurolite zone. **A.** Sample 94-NM-119D, staurolite + biotite zone. M1 garnet porphyroblast partially retrogressed to a chlorite + biotite + quartz + plagioclase mass which define its original shape. Inclusion-rich relict core of M1 garnet is rimmed by euhedral, inclusion-poor M2 overgrowth. Small, euhedral M2 garnet porphyroblasts are present, some of which overgrow matrix foliation (e.g., small grain in upper right corner). M2 staurolite is developed around composite garnet and includes small M2 garnet grains. Width of field is 6 mm. **B.** Sample 94-NM-135D, kyanite + staurolite zone. Close spatial association of kyanite, staurolite and garnet. Only relict garnet remains. Note sets of parallel fractures in staurolite and kyanite porphyroblasts, at high angle to matrix foliation. Width of field is 6 mm. **C.** Sample 94-NM-129E, high-grade portion of the staurolite + biotite zone. Large staurolite porphyroblast clearly deflects matrix foliation, and S_i is strongly inclined to S_e. Note the close association of garnet porphyroblast partially visible on right hand side of photo, and staurolite. Width of field is 6 mm. **D.** Sample 94-NM-129C, from same outcrop as C. Staurolite porphyroblasts do not noticeably deflect matrix foliation and show S_i parallel to S_e. Width of field is 6 mm. Note: anomalous colours are an artifact of printing.

Plate 5

Plate 6 Retrogression and deformation of prograde M2 minerals. **A.** Sample 95-NM-171B, staurolite + biotite zone. Partially to completely retrogressed staurolite porphyroblasts. Composite M1-M2 garnet porphyroblast surrounded by muscovite-rich aggregates which are pseudomorphs after large staurolite porphyroblasts. On the right hand side of the garnet, a small relict staurolite grain is preserved in the core of a pseudomorph. Note that pseudomorph outlines deflect matrix foliation. Also note post-M1 fracture in garnet filled by inclusion-poor M2 garnet, and inclusion-poor subhedral rim. Width of field is 6 mm. **B.** Sample 95-NM-175A, staurolite + biotite zone. Completely retrogressed staurolite (?) porphyroblast. Muscovite ± chlorite pseudomorph (ps) after staurolite closely associated with partially chloritized and fractured garnet porphyroblast. Note that shape of original staurolite is still discernable, and that it gently deflects matrix foliation. Width of field is 6 mm. **C.** Sample 96-NM-214J, staurolite + biotite (+ and) zone. Fractured and boudinaged andalusite porphyroblast. Biotite is seen to have developed in a boudin neck in andalusite, just to right of center. Width of field is 6 mm. **D.** Sample 94-NM-103D, staurolite + biotite (+ and) zone. Muscovite ● chlorite pseudomorph after andalusite, with relict andalusite preserved in core. Note alignment of muscovite and chlorite flakes after andalusite with dominant matrix foliation. Width of field is 3 mm. Note: anomalous colours are an artifact of printing.

Plate 6

Plate 7 Sillimanite-bearing rocks from western reaches of the study area (see Fig. 2.6). **A.** Sample 95-NM-156, sillimanite + staurolite zone. Fibrolitic sillimanite + biotite intergrowth developed on what is interpreted to have been a chlorite-rich pseudomorph after garnet, in close association with staurolite. Note local presence of undeformed chlorite which may be a product of early garnet retrogression. Width of field is 6 mm. **B.** Sample 95-NM-158C, sillimanite + garnet + biotite zone. Late, euhedral garnet developed over fibrolitic sillimanite + biotite intergrowth on early garnet pseudomorph. Early garnet may have been split, as suggested by the bilobate outline of the pseudomorph, and is interpreted top be of M1 timing. Width of field is 6 mm. **C.** Sample 95-NM-158C, sillimanite + garnet + biotite zone. Late, euhedral overgrowth on partially resorbed, inclusion-rich garnet core. Garnet core is interpreted to be of M1 timing, and garnet overgrowth was the result of staurolite-breakdown reaction during M2 (see text). Width of field is 6 mm. **D.** Sample 95-Big-9, sillimanite + garnet + biotite zone. Matrix sillimanite is fibrolitic to finely crystalline, aligned in the dominant foliation, and folded along with other matrix minerals. Width of field is 6 mm. Note: anomalous colours are an artifact of printing.

Plate 7

Plate 8 Macroscopic structural elements. **A**: Folded and transposed S_T. View looking east (outcrop 94-NM-54) at tight fold in psammitic sequence. Note thickened hinge, and attenuated to pinched-out upper limb of most prominent fold in the lower half of the outcrop. **B**: N-S trending folds, outcrop 95-NM-150, looking north. Isoclinal intrafolial fold (arrow) in semi-pelitic sequence. **C**: View looking east at semi-pelite outcrop on main N-S ridge in the central portion of the study area (outcrop 94-NM-30). S_T is defined by the layering and schistosity, and dips moderately to the ESE. Undulations are the result of late, steep, SE-trending crenulation. Note pinched-out layers in the left half of the outcrop (arrow). **D**: Two intersection (crenulation) lineations, outcrop 94-NM-11, southern part of the study area. The lineation running from upper left to lower right is the more conspicuous of the two, and is the result of the intersection of steeply-dipping, ESE-striking crenulation cleavage with the dominant foliation S_T. A less well developed lineation is visible which is at high angle to it. This is the NNE-trending lineation. Crenulation cleavage associated with this lineation is very poorly developed. Note: anomalous colours are an artifact of printing.

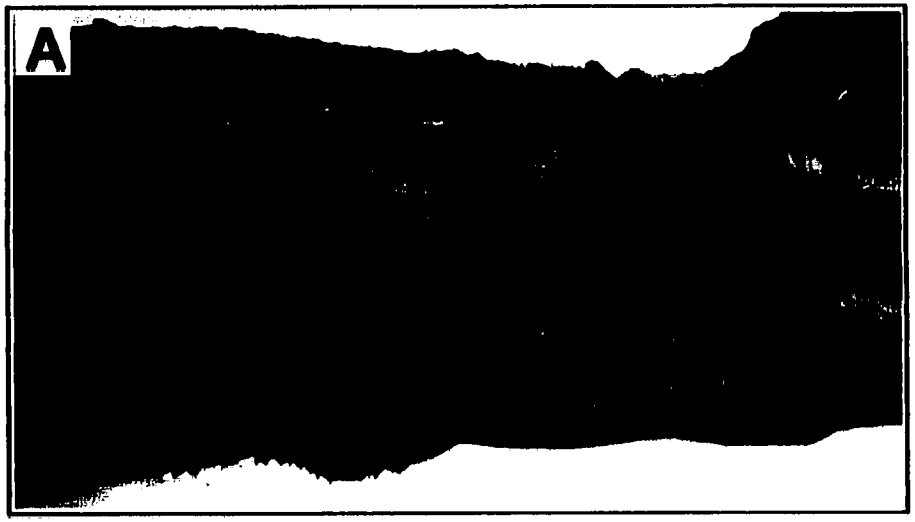
A


C

Plate 9 Split or fractured garnet porphyroblasts. **A**: Hand sample from outcrop 94-NM-119, staurolite + biotite zone, cut parallel to L_T lineation. Note asymmetric fold of concordant quartz vein in lower part of sample, and intrafolially refolded leucocractic layer near the center (large arrow). Split garnet porphyroblasts (small arrows) show gaps at high angle to S_T, the dominant foliation highlighted by compositional layering consisting of biotite-rich, and quartz-rich laminae. **B**: Mineral/intersection lineation, L_T, defined by alignment of elongate biotite flakes on S_T surface, outcrop 94-NM-111. Note split garnet porphyroblasts with split at high angle to L_T. **C**: Sample 96-NM-165C, S_T-normal, L_T-parallel cut. Split garnet with gap at high angle to S_T. S_i in garnet fragments is approximately parallel to the external foliation S_T, indicating that no post-splitting rotation took place. Note that many fractures in staurolite porphyroblasts are sub-parallel to garnet split. Also note local, thin, inclusion-poor overgrowth on split garnet fragments. Width of field is 10 mm. **D**: Sample 94-NM-75B, composite S_T. Differing extents of transposition in matrix and in garnet porphyroblast. Dominant foliation in large garnet is a crenulation cleavage (S_{cr}) which overprints earlier continuous cleavage preserved in microlithons (S_c). In matrix, a later-cycle continuous cleavage (S_c) is parallel to S_{cr} in garnet. No clear trace of earlier foliation is found. Late shear bands (S_{sb}) overprint dominant foliation in both garnet and matrix. Width of field is 6 mm. Note: anomalous colours are an artifact of printing.

Plate 9

Plate 10 Different stages of progressive transposition of the dominant foliation in the same outcrop, staurolite + biotite zone. **A, B**: Sample 94-NM-215A, showing S_{cr}, crenulation of an earlier foliation (S_c) defined by the preferred orientation of muscovite flakes. The orientation of the crenulation foliation (S_{cr}) is irregular and some later shear bands (S_{sb}) appear to cross-cut crenulations (e.g., in lower left quadrant of picture, see B). Note that many large biotite flakes lie parallel to S_{cr}, but have S_i approximately parallel to S_c. Some biotite flakes appear to be randomly oriented. This sample shows a less advanced stage of a transposition cycle than sample in C,D. **C, D**: Sample 94-NM-215B, showing strong crenulation cleavage (S_{cc}) parallel to layering, marked by muscovite-rich laminae. Note irregular, anastomosing nature of this strong crenulation cleavage, and compositional layering/segregation associated with it. Earlier foliation S_c is extensively transposed, but preserved in quartz-rich microlithons as recrystallized, isoclinally folded thin muscovite-rich laminae. Note large, foliation-parallel fish-shaped biotite flakes lying approximately parallel, and locally showing S_i at high angle, to S_{cc} (arrow). Width of field is 6 mm for all photomicrographs. A and C are in plane polarized light; B and D are in cross-polarized light. Note: anomalous colours are an artifact of printing.

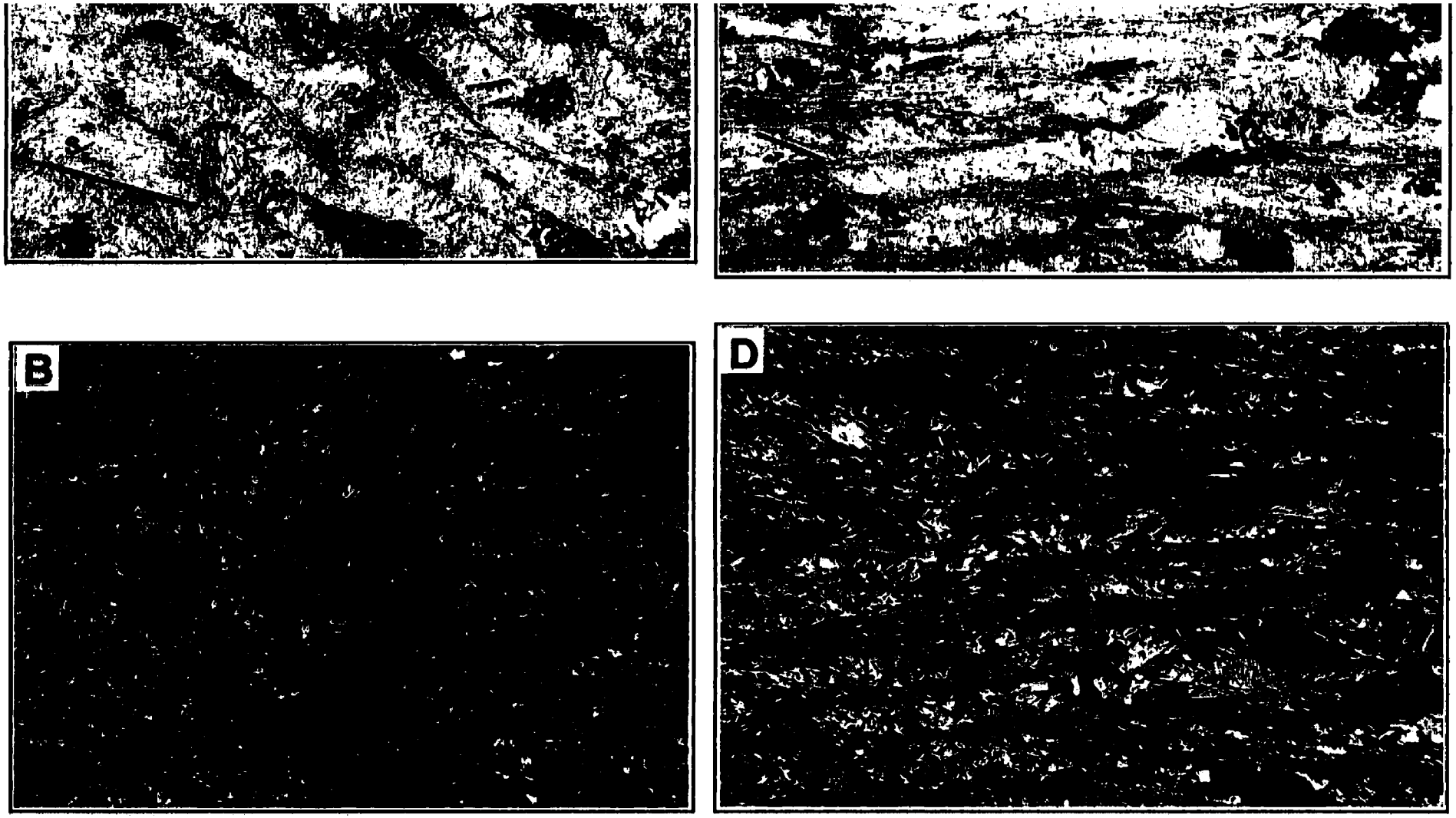

Plate 10

Plate 11 Lineation-defining biotite porphyroblasts in L_T-normal and L_T-parallel sections. **A, B**: Sample 94-NM-166B, staurolite + biotite zone. A shows L_T-parallel cut in which most biotite flakes lie parallel to S_T. B shows L_T-normal cut in which biotite flakes lie at shallow to moderate angle to S_T, and show a preferred vergence with respect to it, defining a foliation, S_T'. Coin is approximately 17 mm in diameter. **C, D**: Sample 96-NM-205B, staurolite + biotite zone. C shows L_T-normal cut. An S-C-type fabric is defined by two shallow-dipping (in this view), discontinuous, cross-cutting foliations (thick lines), forming eye-shaped domains (dashed). A left-dipping foliation is defined by the preferred orientation of most matrix muscovite flakes, and is at shallow angle to earlier compositional layering highlighted by a quartz-rich band running from lower left to center right (large arrow). Some medium-sized biotite flakes parallel this foliation. A right-dipping foliation is highlighted by the preferred orientation of thin, medium-sized biotite flakes. Note that some biotite flakes lie sub-horizontal in the figure, at angle to both left-dipping and right dipping foliations. These flakes tend to be fish-shaped, and elongate inclusions (S_i) are at high angle to both foliations. Also note other biotite flakes which are blocky to rectangular, do not lie parallel to a foliation, have S_i parallel to local external foliation, and appear to overgrow both left- and right-dipping foliations (e.g., 2-3 flakes lumped together in the upper right corner of the figure, small arrow). D shows L_T-parallel cut. One strong preferred orientation of platy minerals (sub-horizontal) is visible, and foliation is much more regular in this cut than in the L_T-normal cut. Most biotite flakes are elongate to fish-shaped. The majority of flakes lies sub-parallel to the foliation, but a few flakes lie at a shallow angle to it (arrows). Width of field for C, D is 6 mm. Note: anomalous colours are an artifact of printing.

Plate 12 Rotated and deformed biotite porphyroblasts. **A**: Sample 96-NM-201B, staurolite + biotite zone. S_T-normal, L_T-parallel cut showing large biotite fish with opposite senses of asymmetry (two flakes left and right of center, inferred local sense of shear shown by arrows). Note S_i in flake on the right is rotated relative to S_T. Also note pinch-and-swell aspect of lamination in quartz vein at bottom. **B**: Sample 96-NM-208A, staurolite + biotite zone. S_T-normal, L_T-parallel cut showing large twinned biotite flakes. Also note that different porphyroblasts appear to show different sense of rotation. **C**: Sample 96-NM-214K, staurolite + biotite zone. S_T-normal, L_T-normal cut. Extensional crenulation (S_{cc}, lower left to upper right) and earlier, dominant foliation (S_c, sub-horizontal) anastomose to form an S-C' fabric. Note close association of crenulation with large, rotated and locally split biotite porphyroblasts **D**: Sample 96-NM-225F, staurolite + biotite zone. Two large biotite flakes in the center have opposite shape asymmetry, and opposite apparent sense of rotation of S_i relative to S_e. Width of field is 6 mm for all photomicrographs. Note: anomalous colours are an artifact of printing.

Plate 13 Split or fractured porphyroblasts. **A**: Sample 96-NM-201A, staurolite + biotite zone, S_T-normal, L_T-parallel cut. Fractures in garnet (lower right) and gap in biotite (upper left) have similar orientation approximately perpendicular to dominant foliation S_T. Width of field is 6 mm. **B**: Sample 95-NM-166B, staurolite + biotite zone, S_T-normal, L_T-parallel cut. Post-kinematic staurolite porphyroblast is split, but relative displacement of resulting fragments is difficult to estimate. Width of field is 6 mm. **C**: Sample 96-NM-214J, boudinaged andalusite porphyroblast, showing split at high angle to S_T, and development of biotite in boudin neck just right of center. Width of field is 6 mm. **D**: Photomicrograph of sample 94-NM-109, staurolite + biotite zone, showing boudinaged, elongate feldspar grain. S_T is approximately horizontal and splits are at high angle to it. Width of field is 10 mm. Note: anomalous colours are an artifact of printing.

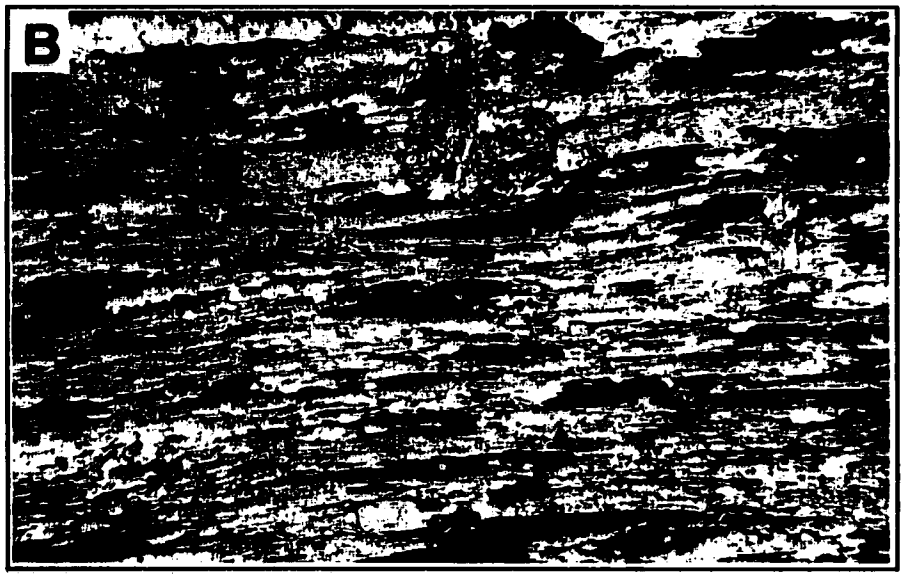

Plate 13

Plate 14 Extensional structural elements. **A**: Biotite-rich high-strain zone in semi-pelitic sequence, outcrop 96-NM-235, staurolite + biotite zone, looking west, L_T-normal cut. Note pinched-out psammite layers and quartz veins. An outcrop-scale shear band is highlighted by passages of dense biotite-rich layers which cut through S_T layering at shallow angle, from top left to bottom right of picture. Inferred sense of shear is top-down-to-the-north. **B**: Hand sample 94-NM-71A, staurolite + biotite zone, showing extensional crenulation cleavage/shear bands (S_{sb}) at moderate angle to dominant foliation (S_c), producing an S-C'-type fabric. Width of field is 8 cm. **C**: Sample 96-NM-200B, staurolite + biotite zone, S_T-normal, L_T-parallel cut. Large extensional shear band runs from upper left to lower right. Note counterclockwise apparent rotation of large chlorite flakes and matrix white micas immediately to right of shear band. Width of field is 6 mm. **D**: Hand sample 96-NM-223A, staurolite + biotite zone, S_T-normal, stretching lineation-parallel cut. View is to south. A feldspar grain on the lower left corner is boudinaged, and the resulting split surfaces are at a $<90^o$ angle to S_T. Several winged and sigmoidal feldspar porphyroclasts indicate a top-to-the-west sense of motion, consistent with boudinaged clasts of feldspar. Coin is 17 mm in diameter. Note: anomalous colours are an artifact of printing.

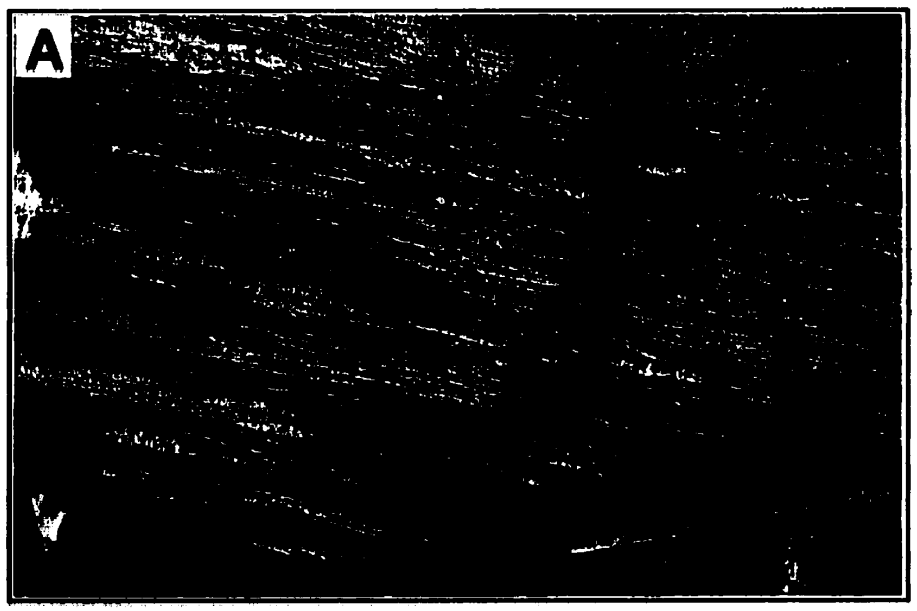

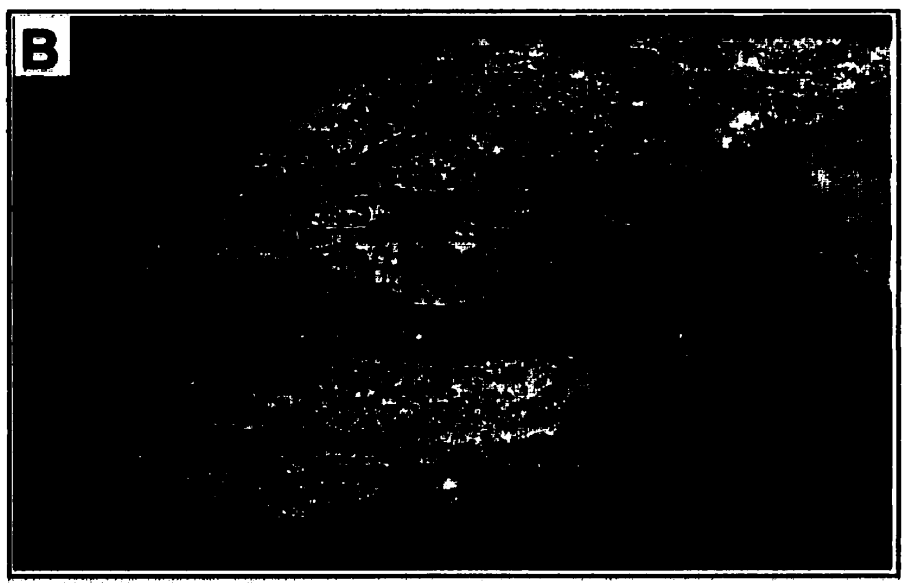

Plate 14

Plate 15 Folds with L_T-parallel axes. **A**: Folded quartz veins, outcrop 94-NM-82, garnet zone. Dismembered hinges of folded quartz veins form ridges on the dominant foliation surface (which mostly parallels the outcrop surface). Compass points north. **B**: Outcrop 94-NM-113, staurolite + biotite zone. Dismembered hinges of folded quartz veins on S_T surface approximately parallel L_T, highlighted by elongate biotite grains (both trend from lower left to upper right on figure). Coin is 24 mm in diameter. **C**: Same outcrop as B, looking approximately normal to L_T and fold axes, and showing asymmetric, tight fold of thin, sub-concordant quartz vein. Note thin biotite segregation highlighting compositional layering-parallel dominant foliation. Coin is approximately 1.5 mm thick. Note: anomalous colours are an artifact of printing.

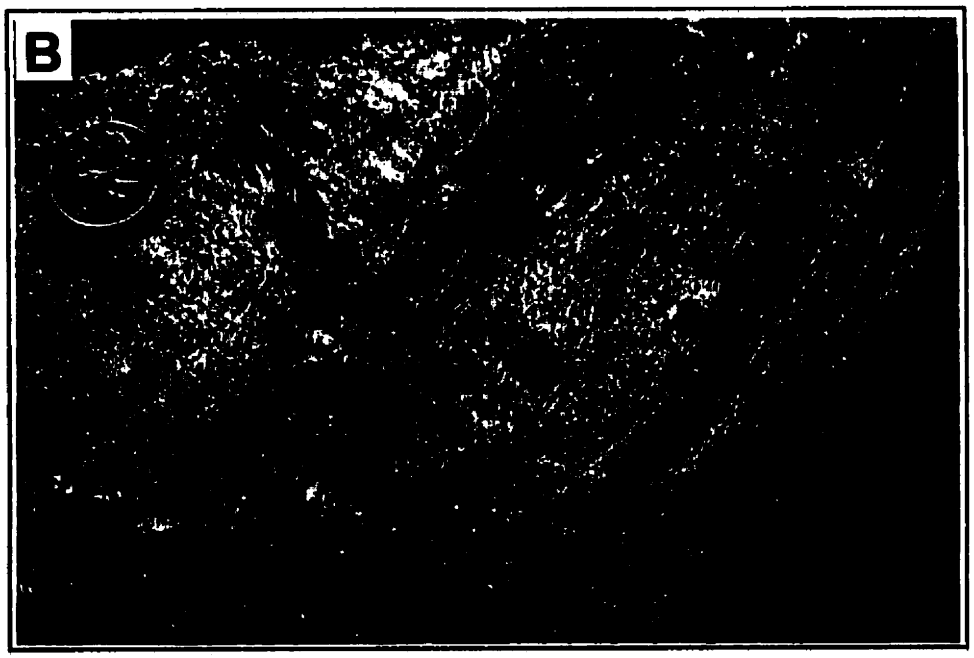

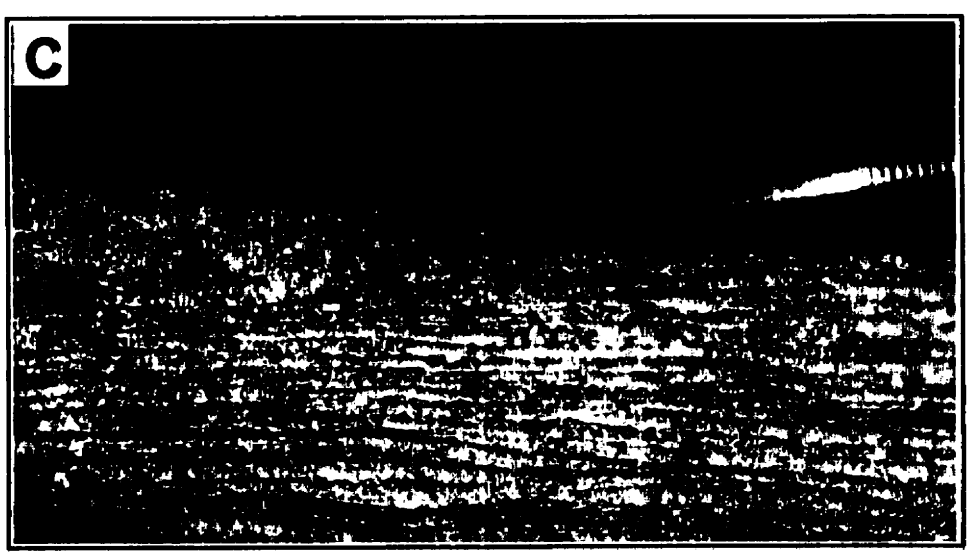

Plate 15

Plate 16 Stretching lineation. **A**: Outcrop 94-NM-127, staurolite + biotite zone, looking north. Strained gritty psammite with stretched quartz and feldspar (white) porphyroclasts. **B**: Sample 94-NM-101, staurolite + biotite zone. Large, elongate quartz grains with straight grain boundaries at high angle to foliation define ribbon quartz. These grains show deformation twins and sub-grain boundaries (open arrow), and small, dynamically recrystallized grains at their boundaries (closed arrow). Cross-polarized light. Width of field is 6 mm. **C, D**: S_T-normal, L_T-normal and L_T-parallel cuts, respectively, sample 94-NM-120Q, staurolite + biotite zone, showing ribbon quartz and strongly stretched feldspar porphyroclasts in C. Coin is 24 mm in diameter. Note: anomalous colours are an artifact of printing.

A

B

Appendix II: Outcrop locations and list of samples

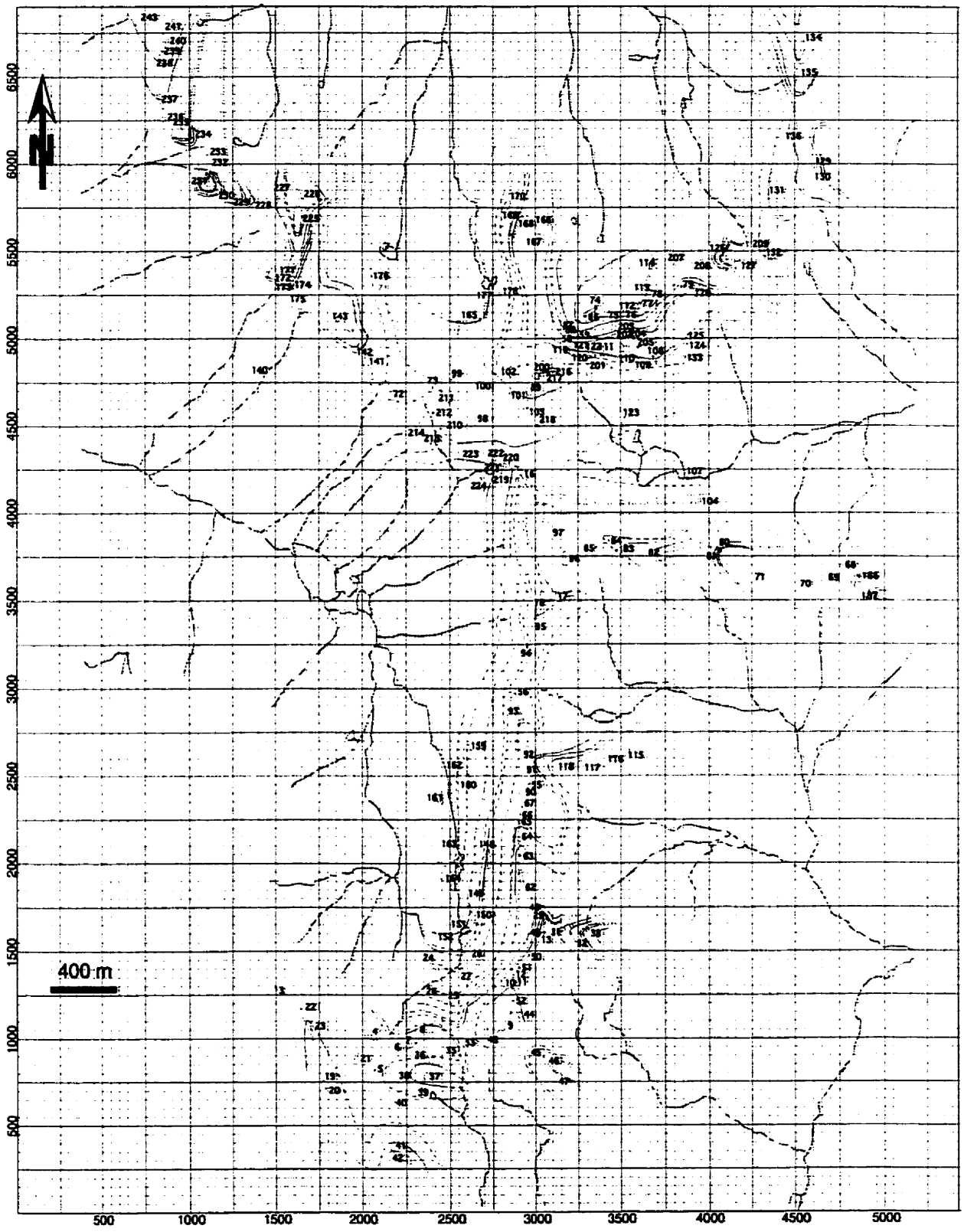

Figure A-II.1 Locations of outcrops and samples discussed in text.

List of samples

SAMPLE	TYPE	T/S	GARNET	COMMENTS
94-NM-2A	impure limestone		N	
94-NM-2B	chl-schist		N	
94-NM-2C	quartzite		N	
94-NM-2L	carb chl-schist	Y	N	
94-NM-2M	carb chl-schist	Y	N	development/transposition of ST, cut at hi-angle by late cren cleavage
94-NM-2U	carb chl-schist		N	pressure-sol'n cren. cleavage
94-NM-2LE	chl-schist	Y	N	early isoclinal fold overprinted by late crenulation****
94-NM-2ME	carb chl-schist	Y	N	
94-NM-2UE	carb chl-schist		N	pressure-sol'n cren. cleavage
94-NM-3	ms-schist		N	
94-NM-4	bt ms-schist		N	
94-NM-5	carb chl-schist		N	
94-NM-6	fu imp. limestone		N	
94-NM-8A	calc-silicate		N	
94-NM-8B	impure limestone		N	
94-NM-8C	carb vein imp. lm	Y	N	
94-NM-8L1	chl-ms-schist,rusty		N	
94-NM-8L2	carb chl-ms-schist		N	
94-NM-8M	chl-ms-schist		N	
94-NM-8U	chl-ms-schist		N	
94-NM-9A	schist		N	
94-NM-9B	schist		N	
94-NM-9C	limestone		N	folded
94-NM-9D	carb schist		N	
94-NM-9L	chl-ms-schist		N	
94-NM-9M	chl-ms-schist		N	
94-NM-9U	chl-ms-schist		N	
94-NM-11	ms-schist		N	
94-NM-15A	gt psammite	Y	N	w/ "blotchy"-chl layers
94-NM-15B	schist		Y, split	
94-NM-16A	cf schist		Y, split	
94-NM-16B	cf schist	Y(2)	Y,split	
94-NM-16C	psammite		N	
94-NM-16D	semi-pelite/psam.		Y,split	gt on vein wall and diffusion "halo" away from vein

List of samples

SAMPLE	TYPE	T/S	GARNET	COMMENTS
94-NM-16L		Y	Y	
94-NM-16M			Y,split	
94-NM-16U				
94-NM-16W				
94-NM-16X				
94-NM-16Y				
94-NM-16Z				
94-NM-16AA				
94-NM-17	gt schist	Y	Y,split	
94-NM-18B	psammite		Y,split	
94-NM-18C	strained psammite		Y,split	
94-NM-18S			Y,split	
94-NM-18T			Y,split	
94-NM-19L	schist		N	
94-NM-19M	psammite	Y	N	
94-NM-19U	psammite	Y	N	
94-NM-20L			N	
94-NM-20M			N	
94-NM-20U		Y	N	early ST-// isoclinal folds overprinted by hi-angle late cren cleavage
94-NM-21L			N	
94-NM-21U			N	
94-NM-22	impure limestone		N	
94-NM-23A	gritty psammite		N	big Ab porphyroblasts
94-NM-23B	bt schist?		N	
94-NM-23C	ms schist	Y	N	
94-NM-23D	schist	Y(1)	N	
94-NM-24	schist	Y	N	
94-NM-26L1	carb schist	Y	N	
94-NM-26M	qz-fs ms-schist		N	
94-NM-26U	carb schist		N	
94-NM-27A	bt ?	Y	N	
94-NM-27B	bt ms-schist	Y	N	
94-NM-29A	limestone	Y	N	
94-NM-29B			N	

List of samples

SAMPLE	TYPE	T/S	GARNET	COMMENTS
94-NM-30L	chl-schist		N	
94-NM-30U	chl-schist		N	
94-NM-31L	bt chl-schist	Y	N	
94-NM-31U	chl-schist		N	
94-NM-33L	carb schist	Y	N	
94-NM-33U(?)			N	
94-NM-33A	schist		N	
94-NM-34	gt-sill schist		N	float
94-NM-36A	fu qz-vein		N	
94-NM-36B	carb schist?		N	
94-NM-37A			N	
94-NM-37U			N	
94-NM-38L	carb chl-schist	Y	N	
94-NM-38M	carb chl-schist	Y	N	
94-NM-38U	carb chl-schist		N	good solution cleavage
94-NM-39	calc-silicate	Y	N	
94-NM-42A	calc-silicate	Y	N	
94-NM-42B	fu calc-silicate	Y	N	
94-NM-44A	ms-chl-schist		N	
94-NM-44B	ms-chl-schist	Y	N	
94-NM-44C	ms-chl-schist		N	
94-NM-44D	ms-chl-schist w/lm	Y	N	
94-NM-45A		Y	N	P-sol cleavage, similar to 117; early fold overprinted by cren
94-NM-45B		Y	N	
94-NM-45D			N	
94-NM-46A			N	
94-NM-46B		Y	N	
94-NM-47A			N	
94-NM-47B			N	
94-NM-48A			N	
94-NM-48B			N	
94-NM-48C		Y	N	
94-NM-48D		Y	N	
94-NM-48E		Y	N	

List of samples

SAMPLE	TYPE	T/S	GARNET	COMMENTS
94-NM-48F			N	
94-NM-48G		Y	N	
94-NM-48H			N	bt // foliation
94-NM-49A		Y	N	
94-NM-49B			N	
94-NM-49C		Y	N	
94-NM-50A		Y	N	bt // foliation
94-NM-50B			N	
94-NM-51		Y	N	
94-NM-52			N	
94-NM-53			N	
94-NM-54A		Y	N	bt-porph (1-2mm); post-k
94-NM-55	psammite	Y	N	late bt-foliation
94-NM-56	psammite		N	
94-NM-59		Y	Y,split	
94-NM-60A		Y	Y	syn-k gt
94-NM-60B		Y(2)	Y,split	
94-NM-60C			Y,split	
94-NM-60D	gray layered marble	Y	N	
94-NM-60E	gray layered marble		N	
94-NM-61B	fine-gr. psammite	Y	N	
94-NM-61U			N	
94-NM-62L			N	
94-NM-62U			N	
94-NM-63L			N	P-sol cleavage
94-NM-63U			N	post-crenulations? chl-prophyroblasts
94-NM-64	ab-porph chl-sch.		N	
94-NM-64B	semi-pelite		N	
94-NM-65L	ms-chl-schist	Y	N	solution cleavage sub-// layering
94-NM-65L2		Y	N	
94-NM-65U		Y	N	
94-NM-67A	fine-gr psammite		N	
94-NM-67B			N	strong compositional segregation
94-NM-68A	calc-pelite	Y	Y,split	post-k garnet; Ab porphyroblasts

List of samples

SAMPLE	TYPE	T/S	GARNET	COMMENTS
94-NM-68B	calc-pelite		Y,split	
94-NM-68C			Y,split	
94-NM-69		Y	N	
94-NM-69A	calc-pelite		Y,split	
94-NM-69B	marble		N	
94-NM-69C		Y		
94-NM-69D	blotchy amphibolite	Y	?	"blotchy-chl" +gt rock
94-NM-70A				
94-NM-70B			N	
94-NM-70C				
94-NM-70D	psammite			
94-NM-71A		Y	Y,split?	gt chloritized
94-NM-71B				
94-NM-72A		Y	Y,split	
94-NM-72B		Y	Y,split	
94-NM-72C	fine-gr gritty psam		N	
94-NM-73		Y	Y,split	gt chloritized
94-NM-73S			Y,split?	
94-NM-73T				
94-NM-74A			N	
94-NM-74B			N	
94-NM-74C	gray marble		N	
94-NM-74D	blotchy amphibolite		N	
94-NM-75A	amphibolite		N	
94-NM-75B		Y	Y,split	
94-NM-75C				
94-NM-76Q				
94-NM-76R		S		
94-NM-78A		Y	Y,fract'd	
94-NM-78Q		S		
94-NM-78R		S(2)		
94-NM-78S		S(2)	Y,split	
94-NM-78T		S(2)	Y,fract'd	
94-NM-78U			Y,fract'd	

List of samples

SAMPLE	TYPE	T/S	GARNET	COMMENTS
94-NM-79A	semi-pelite		Y,split?	
94-NM-79B	pelite		N	
94-NM-79C	pelite		Y,split?	
94-NM-80A				
94-NM-80B	psammite			
94-NM-80C				
94-NM-80L	pelite/psammite		Y,split	
94-NM-80U		Y	Y,split	
94-NM-81A			N	
94-NM-81B			N	
94-NM-81C			N	
94-NM-82A	blotchy psammite			
94-NM-82B		Y	Y	gt chloritized
94-NM-82C				
94-NM-82D				
94-NM-84				
94-NM-85A			N	
94-NM-85B			N	
94-NM-85C		Y	Y,split	gt chloritized
94-NM-86A		Y	Y,split	
94-NM-86B		Y	Y,split	
94-NM-86S		S	Y	
94-NM-86Q		S	Y	
94-NM-87A				
94-NM-87B				
94-NM-88A				
94-NM-88B				
94-NM-88C				
94-NM-89A	semi-pelite		Y?	strong compositional segregation
94-NM-89B			Y,split	gt chloritized
94-NM-89C			Y,split	strong compositional segregation
94-NM-90A			N	
94-NM-90B	psammite		N	
94-NM-90C			N	

List of samples

SAMPLE	TYPE	T/S	GARNET	COMMENTS
94-NM-90D			N	
94-NM-91A			N	
94-NM-91B			N	
94-NM-91C	bt-rich psammite		N	
94-NM-92A			N	
94-NM-92B			N	
94-NM-92C			N	
94-NM-92D			N	
94-NM-93A			N	
94-NM-93B			N	
94-NM-93C			N	
94-NM-93D			N	
94-NM-94A			N	
94-NM-94B			N	
94-NM-97A			Y,split	
94-NM-97B			Y,split	
94-NM-97C			Y,split	
94-NM-98A			Y,split	
94-NM-98B			Y,split	
94-NM-98C			Y,split	
94-NM-98F			Y,split	
94-NM-103A		Y	Y,split	gt chloritized
94-NM-103B			Y,split	
94-NM-103C			Y,split	
94-NM-103D		Y(4)	Y,split	core of c.f preserved andalusite
94-NM-105			N	
94-NM-107A		Y		from loose block
94-NM-108A				
94-NM-108B				
94-NM-108C		Y(2)	Y,split	gt chloritized
94-NM-109	sheared gritty psam.		N	
94-NM-110A		Y(2)	Y,split	
94-NM-110B		Y(2)	Y,split	
94-NM-110C			Y,split	

List of samples

SAMPLE	TYPE	T/S	GARNET	COMMENTS
94-NM-110D		Y	Y,split	
94-NM-110E			Y,split	
94-NM-111A			Y,split	
94-NM-111B		Y(2)	Y,split	
94-NM-111Q		S(2)	Y,split	
94-NM-112A			Y	
94-NM-112B			Y	
94-NM-112C			Y	
94-NM-112D			Y	
94-NM-112E			Y	
94-NM-113A			Y	
94-NM-113B			Y	
94-NM-113C			Y	
94-NM-113D			Y	
94-NM-113E			Y	
94-NM-113J			Y, fract'd	
94-NM-113K		Y(2)	Y	pseudomorph after actinolite (garbenschieffen)
94-NM-113L				
94-NM-114A			N	
94-NM-115A			N	
94-NM-115B	ab-porph ms-sch.	Y	N	extensional shear bands
94-NM-115C	ab-porph ms-sch.		N	strong crenulation
94-NM-116A		Y	N	
94-NM-116B		Y	N	extensional shear bands
94-NM-116C	psammite		N	
94-NM-116D			N	
94-NM-117A			N	P-sol cleavage
94-NM-117B			N	P-sol cleavage
94-NM-117C		Y	N	P-sol cleavage
94-NM-118A			N	
94-NM-118B		Y	N	
94-NM-118C		Y	N	bt-foliation/gneissosity
94-NM-118D		Y	N	
94-NM-118E			N	3 foliations

List of samples

SAMPLE	TYPE	T/S	GARNET	COMMENTS
94-NM-119A		Y	Y	
94-NM-119B		Y	N	graded bedding
94-NM-119C		Y	Y,split	
94-NM-119D		Y	Y,split	late bt associated w/ P-sol cren. Cleavage
94-NM-120Q	psammite	S	N	oriented; looking S on thin section
94-NM-124			Y,split	
94-NM-125A		Y	N	
94-NM-125B				
94-NM-126A	psammite		N	
94-NM-126B				
94-NM-126C		P(2)		
94-NM-126D				
94-NM-126E				
94-NM-126F	pl-amphibolite	Y		
94-NM-127A		Y	Y,split	rotated grt
94-NM-127B				
94-NM-129A			Y,split	
94-NM-129B				
94-NM-129C				
94-NM-129D				
94-NM-129E	stt-bearing pelite	Y	Y,split	
94-NM-129Q				
94-NM-131A				
94-NM-131B				
94-NM-135A	talc schist	Y	N	talc-trem
94-NM-135B			N	talc-trem
94-NM-135C	stt-ky (ms) schist	Y	N?	
94-NM-135D	stt-ky (ms) schist	Y	Y,split	
94-NM-135E			Y,split	syn- to late-k stt and ky
94-NM-135G?		Y	Y,split	
95-NM-141A		Y	Y,split	
95-NM-141B	gritty psammite	Y	N	oriented
95-NM-142	chl-schst/phyllonite	Y	N	oriented, highly strained
95-NM-142B		Y		

List of samples

SAMPLE	TYPE	T/S	GARNET	COMMENTS
95-NM-143		Y	Y,split	
95-NM-145				chlorite schist
95-NM-145B		Y		oriented
95-NM-147		Y		
95-NM-148				sheared psammite
95-NM-149	gritty psammite	2		oriented
95-NM-150		Y		
95-NM-151		Y		
95-NM-153A		2		
95-NM-153B		2		
95-NM-153C				
95-NM-154B		Y		
95-NM-155A		Y		
95-NM-155B				
95-NM-156		2		
95-NM-157A				
95-NM-157B		Y		
95-NM-158	gritty psammite	Y		oriented
95-NM-158B		2		
95-NM-158C		2	Y,split	gt-> sill-rich mats
95-NM-159A	med-gray pelitic schist	Y	N	
95-NM-159B			N	
95-NM-159C	semi-pelite	Y	N	
95-NM-160		Y	N	
95-NM-162		2	N	
95-NM-164A	pale-green pelite	Y	N	
95-NM-164B	semi-pelite	Y	N	
95-NM-165A	psammite		N	oriented
95-NM-165C			Y,split	
95-NM-165D			Y,split	
95-NM-166A			Y,split	
95-NM-166B			Y,split	
95-NM-167			Y,split	
95-NM-167B			Y,split	

List of samples

SAMPLE	TYPE	T/S	GARNET	COMMENTS
95-NM-168			Y,split	
95-NM-168B			Y,split	
95-NM-169			Y,fract'd	
95-NM-170A				
95-NM-170B				
95-NM-171A			Y,split	
95-NM-171B			Y,split	
95-NM-172				
95-NM-173A	gritty psammite		N	oriented
95-NM-173B				
95-NM-175			Y,fract'd	gt chloritized
95-NM-175A			Y,split	
95-NM-175B			Y,fract'd	
95-NM-176A	calc-pelite		Y	
95-NM-176B	calc-pelite		Y	
95-NM-176C	calc-pelite		Y	
95-NM-176D	calc-pelite		Y	
95-NM-176E	calc-pelite		Y	
95-NM-177				
95-NM-178				
95-NM-184A	amphibolite	Y	N	large actinolite splays
96-NM-200A		Y	Y,split	
96-NM-200B		Y	Y,split	
96-NM-201A		Y(2)	Y,split	
96-NM-201B		Y(2)	Y,split	
96-NM-202A		Y	Y,split	
96-NM-203A		Y	Y,split	
96-NM-203B		Y	Y,split	
96-NM-204A		Y		
96-NM-205A		Y		
96-NM-205B		Y(2)	Y,split?	
96-NM-207A	calc-silicate	Y		
96-NM-207B	fu? calc-silicate	Y		
96-NM-208A		Y	Y,split	

List of samples

SAMPLE	TYPE	T/S	GARNET	COMMENTS
96-NM-208B		Y	Y,split	
96-NM-209	amphibolite	Y		
96-NM-210A				
96-NM-214A		Y		
96-NM-214B		Y		
96-NM-214C		Y(2)		
96-NM-214D				
96-NM-214E?				
96-NM-214F		Y		
96-NM-214G		Y		
96-NM-214H		Y		
96-NM-214J		Y		
96-NM-214K		Y		
96-NM-214L				
96-NM-215A		Y		
96-NM-215B		Y		
96-NM-217A				
96-NM-217B				
96-NM-219A		Y		
96-NM-219B		Y		
96-NM-220A		Y		
96-NM-220B				
96-NM-221A				
96-NM-221B				
96-NM-223	psammite	Y		oriented; looking N on thin section
96-NM-225A		Y	Y,split	
96-NM-225B		Y	Y,split	
96-NM-225C		Y	Y,split	
96-NM-225D				
96-NM-225E?		Y		
96-NM-225F		Y	Y,split	
96-NM-226A		Y	Y,split	
96-NM-226B		Y	Y,split	
96-NM-226D		Y	Y,split	

List of samples

SAMPLE	TYPE	T/S	GARNET	COMMENTS
96-NM-229A		Y		
96-NM-230A		Y		
96-NM-230B		Y		
96-NM-230C				
96-NM-231A		Y		
96-NM-231B		Y		
96-NM-231C		Y		
96-NM-232A		Y		
96-NM-232B		Y		
96-NM-233A	marble	Y	N	
95-NM-235A		Y	Y,split	
96-NM-235B		Y		
96-NM-235C		Y	N?	extreme compositional segregation
96-NM-236A		Y		
96-NM-237A		Y		
96-NM-237B	mylonite	Y	Y,split	
96-NM-238A		Y	N	
96-NM-238B			N	
96-NM-239A		Y		
96-NM-240A				
96-NM-240B	marble	Y	N	
96-NM-242A	marble	Y		
96-NM-242B	marble			
96-NM-242C	marble, coarse-gr	Y	N	
96-NM-242D	marble	Y	N	
96-NM-242E	marble	Y	N	
96-NM-242F	marble	Y	N	
96-NM-242G	marble	Y	N	
96-NM-243A		Y	N	fold
95-Big-2		2		
95-Big-5A				
95-Big-5B		Y		
95-Big-6		Y		

List of samples

SAMPLE	TYPE	T/S	GARNET	COMMENTS
95-Big-7A		Y		
95-Big-7B				
95-Big-7C		Y		
95-Big-8A				
95-Big-8B		Y		
95-Big-9		Y(2)		
95-Big-10		Y		
95-Big-11		Y		
95-Big-12A				
95-Big-12B		Y		
96-CF-1	float	Y(2)		
96-F-1A	float	Y		
96-F-1B	float			

Appendix III: Mineral Analyses

Chlorite and muscovite microprobe analyses

Chlorite

Sample	NM-111B	NM-111B	NM-111B	NM-111B	NM-111B	NM-111B	NM-111B	NM-111B	NM-111B	NM-111B	NM-111B
An#	1	2	3	4	5	6	7	8	9	10	11
SiO2	24.71	24.92	25.84	24.45	24.60	24.61	24.21	24.44	24.48	24.57	24.84
TiO2	0.08	0.09	0.39	0.07	0.09	0.05	0.07	0.05	0.07	0.07	0.09
Al2O3	23.02	22.95	21.76	22.95	22.97	22.86	22.82	23.16	22.95	22.75	22.42
Cr2O3	0.00	0.00	0.00	0.00	0.03	0.01	0.01	0.00	0.03	0.00	0.00
FeO	24.19	24.61	24.59	24.01	24.42	24.68	24.16	24.80	24.20	23.93	23.58
MgO	15.11	14.84	14.64	14.77	14.95	14.81	14.68	14.41	14.86	14.97	14.49
MnO	0.15	0.16	0.19	0.16	0.14	0.15	0.14	0.14	0.15	0.18	0.14
CaO	0.00	0.00	0.00	0.00	0.00	0.00	0.00	0.00	0.00	0.01	0.02
Na2O	0.00	0.01	0.01	0.01	0.00	0.00	0.00	0.00	0.00	0.01	0.00
K2O	0.03	0.01	0.50	0.02	0.01	0.02	0.05	0.01	0.01	0.02	0.04
F	0.08	0.03	0.07	0.01	0.02	0.05	0.08	0.03	0.03	0.02	0.03
Total	87.38	87.61	88.00	86.45	87.25	87.23	86.22	87.04	86.79	86.53	85.64

Chlorite

Sample	NM-111B	NM-111B	NM-111B	NM-111B
An#	12	13	14	15
SiO2	24.61	24.66	24.66	24.59
TiO2	0.06	0.09	0.07	0.07
Al2O3	22.92	22.60	23.01	22.69
Cr2O3	0.00	0.03	0.03	0.00
FeO	24.23	23.77	24.00	23.84
MgO	14.77	14.98	14.94	14.74
MnO	0.13	0.14	0.12	0.16
CaO	0.00	0.02	0.00	0.01
Na2O	0.01	0.00	0.01	0.01
K2O	0.00	0.03	0.02	0.01
F	0.02	0.09	0.03	0.02
Total	86.76	86.41	86.89	86.15

Muscovite

NM-111B	NM-111B	NM-111B	NM-111B	NM-111B
16	17	18	22	23
48.39	49.09	47.62	47.89	48.68
0.28	0.29	0.33	0.36	0.37
34.89	34.11	35.52	35.69	34.95
0.00	0.00	0.00	0.00	0.00
1.11	1.11	1.50	0.84	1.00
0.83	1.07	0.63	0.56	0.86
0.00	0.00	0.00	0.00	0.00
0.00	0.00	0.00	0.00	0.00
0.99	0.73	0.93	1.00	1.00
9.81	9.79	9.75	9.97	9.86
0.04	0.05	0.04	0.03	0.02
96.32	96.22	96.32	96.33	96.75

Biotite analyses

Sample	NM-111B	NM-111B	NM-111B	NM-111B	NM-111B	NM-111B	NM-111B	NM-111B	NM-111B	NM-111B
An#	1	2	3	4	5	6	7	8	9	10	11
SiO2	34.72	33.97	33.31	33.10	35.46	35.11	30.56	30.30	35.17	34.22	35.31
TiO2	1.95	1.85	1.94	1.44	1.60	1.74	1.15	1.03	1.58	1.55	1.45
Al2O3	17.55	16.26	17.73	18.62	18.50	18.73	19.22	19.56	18.37	18.73	18.53
Cr2O3	0.02	0.03	0.00	0.00	0.02	0.00	0.00	0.00	0.01	0.00	0.00
FeO	18.92	18.21	19.05	21.35	19.86	19.30	22.98	23.15	19.01	18.82	18.88
MgO	11.57	9.93	12.03	11.29	9.87	9.84	12.01	12.20	9.85	9.79	10.15
MnO	0.24	0.21	0.25	0.11	0.08	0.10	0.09	0.12	0.14	0.08	0.10
CaO	0.19	0.24	0.09	0.00	0.01	0.00	0.00	0.00	0.01	0.00	0.01
BaO	0.16	0.18	0.15	0.10	0.17	0.08	0.06	0.06	0.13	0.08	0.15
Na2O	0.39	0.60	0.33	0.14	0.27	0.30	0.06	0.07	0.30	0.28	0.30
K2O	8.27	8.48	8.57	7.05	9.15	9.16	4.65	4.45	9.17	9.17	9.04
F	0.41	0.43	0.42	0.39	0.39	0.40	0.22	0.24	0.28	0.39	0.54
Total	94.40	90.37	93.87	93.59	95.39	94.75	91.01	91.17	94.02	93.11	94.47

Sample	NM-111B	NM-111B	NM-111B	NM-111B	NM-111B	NM-111B	NM-111B	NM-111B	NM-111B	NM-111B
An#	12	13	14	15	16	17	18	19	20	21
SiO2	35.95	35.78	34.81	35.19	35.97	35.09	34.48	29.37	34.94	33.20
TiO2	1.47	1.44	1.49	1.51	1.64	1.56	1.73	0.83	1.65	2.10
Al2O3	18.59	18.71	18.58	18.41	19.01	18.48	18.93	18.67	17.66	16.88
Cr2O3	0.00	0.00	0.02	0.00	0.01	0.00	0.03	0.03	0.03	0.05
FeO	18.64	18.90	19.81	19.27	18.51	19.03	18.66	24.41	21.08	21.09
MgO	10.14	10.11	10.28	10.21	10.03	9.99	10.01	12.13	9.55	11.65
MnO	0.12	0.08	0.13	0.09	0.08	0.08	0.04	0.45	0.50	0.23
CaO	0.00	0.00	0.00	0.00	0.00	0.00	0.00	0.09	0.08	0.04
BaO	0.09	0.14	0.14	0.12	0.06	0.15	0.16	0.08	0.13	0.11
Na2O	0.33	0.26	0.11	0.20	0.25	0.18	0.26	0.13	0.48	0.53
K2O	9.01	9.01	8.79	9.07	9.24	9.05	9.22	3.49	8.33	7.00
F	0.45	0.39	0.32	0.38	0.45	0.40	0.38	0.18	0.34	0.24
Total	94.79	94.81	94.48	94.44	95.25	93.99	93.89	89.87	94.76	93.13

Appendix IV: Structural Measurements

Transposition-related structural elements

	Grid position		ST		ST'		Mineral lineation		Stretching lineation		FT		Gt split	
Outcrop #	X	Y	strike	dip	strike	dip	trend	plunge	trend	plunge	trend	plunge	trend	dip
94-NM-2	1400	1300	65	50										
94-NM-3	1500	1275												
94-NM-4	2050	1000												
94-NM-5	2075	825												
94-NM-6	2020	925	65	22										
94-NM-7	2250	950												
94-NM-8	2350	1025	90	47										
			51	15										
			71	30										
94-NM-9	2825	1100	99	48							265	0		
			74	45										
			71	31										
			74	26										
			82	30										
			86	44										
94-NM-10	2875	1325												
94-NM-11	2900	1325	79	26										
94-NM-12	2875	1375	64	31										
94-NM-13	3025	1575	92	16										
94-NM-14	3053	1625												
94-NM-15	3100	3925	360	14										
94-NM-16	2925	4200	310	10			81	6						
			9	12										
94-NM-17	3225	3550												
94-NM-18	3025	3450	180	20										
94-NM-19	1775	750	0	19										
94-NM-20	1775	725	40	24										
94-NM-21	1975	900	65	29										
94-NM-22	1650	1175												
94-NM-23	1700	1050	80	28										
			53	24										
94-NM-24	2400	1425	49	18										
94-NM-25	2500	1775	88	35										
94-NM-26	2400	1300												
94-NM-27	2600	1325	72	45										
94-NM-28	2675	1450	84	35										
94-NM-29	3025	1725	90	44										
			89	44										
94-NM-30	3050	1600												
94-NM-31	3150	1625	33	34										
94-NM-32	3275	1600	37	34										

Transposition-related structural elements

	Grid position		ST		ST'		Mineral lineation		Stretching lineation		FT		Gt split	
Outcrop #	X	Y	strike	dip	strike	dip	trend	plunge	trend	plunge	trend	plunge	trend	dip
94-NM-33	3250	1625	37	16										
			307	22										
94-NM-34														
94-NM-35	2525	900	0	19										
94-NM-36	2350	875	7	17										
			49	25										
			21	22										
94-NM-37	2350	800	104	28										
			99	54										
			116	43										
			40	24										
94-NM-38	2250	750												
94-NM-39	2325	725	47	33										
94-NM-40	2175	625	248	23										
94-NM-41	2250	350	120	40										
94-NM-42	2225	325	97	46							266	9		
			91	29										
94-NM-43	2700	1025												
94-NM-44	2900	1150	92	28										
94-NM-45	3025	900	65	20										
94-NM-46	3050	850	62	29										
			60	55										
			79	41										
94-NM-47	3175	775	56	36										
			63	30										
94-NM-48	3000	1750	37	24										
			50	30										
			64	32										
			35	26										
			46	22										
94-NM-49	3025	1575	61	24										
94-NM-50	2950	1475	20	23										
94-NM-51	2900	1400												
94-NM-52	2875	1225												
94-NM-53	2625	975	132	52										
			76	45										
94-NM-54	2650	1150												
94-NM-55	2950	2425	57	25										
94-NM-56	2875	2975												
94-NM-57														
94-NM-58	3200	4975												

Transposition-related structural elements

	Grid position		ST		ST'		Mineral lineation		Stretching lineation		FT		Gt split	
Outcrop #	X	Y	strike	dip	strike	dip	trend	plunge	trend	plunge	trend	plunge	trend	dip
94-NM-59	3250	5025												
94-NM-60	3350	5100	327	25										
94-NM-61														
94-NM-62	2925	1900	57	33										
			47	27										
94-NM-63	2900	2050	18	18										
94-NM-64	2900	2150	47	27			98	8						
94-NM-65	2900	2225												
94-NM-66	2925	2275												
94-NM-67	2925	2325	57	23			89	12						
94-NM-68	4775	3700	349	45										
			335	30							74	27		
94-NM-69	4675	3650	8	39										
			23	34										
94-NM-70	4550	3600	7	46										
			345	27			66	24						
94-NM-71	4300	3650	10	27			63	24						
94-NM-72	2150	4725	265	16			257	0						
94-NM-73	2875	4725	306	19										
			297	16							88	6		
94-NM-74	3400	5175	352	14										
94-NM-75	3475	5150	331	20										
94-NM-76	3550	5150	7	33			87	34						
94-NM-77	3625	5200	303	7							319	21		
			347	33			82	35						
94-NM-78	3175	5275	329	24			76	23			74	31		
			341	18							74	15		
94-NM-79	3850	5300	335	25			65	28						
94-NM-80	4050	3775	10	35										
94-NM-81	3975	3800	365	25										
94-NM-82	3750	3750	12	28										
(all isoclinal			21	30							73	28		
folds on same											63	24		
surface)											112	25		
94-NM-83	3475	3775	1	28										
94-NM-84	3425	3850	1	25										
94-NM-85	3375	3800	352	25			87	24						
94-NM-86	3300	5125	304	25										
94-NM-87	3225	5050	306	18										
94-NM-88	3225	5025	304	15					80	10				
94-NM-89	2950	4700	285	15			75	9						

Transposition-related structural elements

	Grid position		ST		ST'		Mineral lineation		Stretching lineation		FT		Gt split	
Outcrop #	X	Y	strike	dip	strike	dip	trend	plunge	trend	plunge	trend	plunge	trend	dip
94-NM-90	2950	2425	68	25							88	18		
			1	17										
			3	17			68	16						
			25	23			69	14						
94-NM-91	2975	2525	36	24							79	15		
			20	25										
			358	23										
94-NM-92	2950	2675	9	26			80	19						
			40	25	30	32	63	20						
			65	25	36	45	66	22						
94-NM-93	2875	2900	33	25										
			14	24							78	30		
			30	26			75	22			70	25		
94-NM-94	2950	3225	18	22										
94-NM-95	3000	3375												
94-NM-96	3175	3750	15	23	26	6					74	22		
94-NM-97	3075	3925	24	18										
94-NM-98	2625	4500	292	12										
			292	20			65	10						
94-NM-99	2500	4775	294	15										
94-NM-100	2675	4750												
94-NM-101	2850	4700												
94-NM-102	2850	4775												
94-NM-103	2950	4600	275	35										
94-NM-104	3925	4050	6	24							69	30		
94-NM-105														
94-NM-106														
94-NM-107	3900	4200	351	25										
94-NM-108	3675	4900	346	23			78	23			65	22		
											74	23		
											70	22		
94-NM-109	3600	4875	311	21										
94-NM-110	3525	4900	327	26			84	26			97	24		
			335	24										
94-NM-111	3400	4900	309	26			74	24			72	27		
			311	23					61	23				
94-NM-112	3550	5150	15	20										
94-NM-113	3650	5275	325	27			71	25						
			322	15			75	15						
							61	10						
94-NM-114	3675	5425	310	30			61	30						

Transposition-related structural elements

	Grid position		ST		ST'		Mineral lineation		Stretching lineation		FT		Gt split	
Outcrop #	X	Y	strike	dip	strike	dip	trend	plunge	trend	plunge	trend	plunge	trend	dip
94-NM-115	3525	2625	42	25										
			39	22										
94-NM-116	3475	2600	28	25			71	11			78	15		
94-NM-117	3275	2575	14	25										
94-NM-118	3200	2575	38	20			74	12			90	30		
			355	30										
94-NM-119	3175	4950	339	10										
94-NM-120	3250	4900	298	10					96	3				
94-NM-121	3250	4925												
94-NM-122	3325	4925	283	20										
94-NM-123	3500	4500												
94-NM-124	3875	4975	3	45			72	45						
94-NM-125	3875	5025												
94-NM-126	4100	5475	329	36			69	35			60	28		
			335	27			70	27	68	26				
94-NM-127	4225	5425	320	29										
			320	25					69	30				
94-NM-128	3925	5250	330	30							72	30		
94-NM-129	4600	6025	0	35										
94-NM-130	4550	5950	340	32			70	29						
94-NM-131	4425	5775	325	41										
94-NM-132	4325	5525	320	40			68	40						
94-NM-133	3800	4900	359	27										
94-NM-134	4550	6650	315	35										
94-NM-135	4500	6500	335	35			65	35						
95-NM-140	1425	4825	283	15										
95-NM-141	2025	4825	283	15										
			308	31										
95-NM-142	2000	5000	277	10										
95-NM-143	1900	5075	295	21										
95-NM-144											270	8		
			310	63							285	0		
			265	15										
95-NM-145			89	59										
			30	18										
95-NM-146														
95-NM-147														
95-NM-148	2725	2025	190	28										
95-NM-149	2675	1875	53	31										
			50	22					73	10				

Transposition-related structural elements

	Grid position		ST		ST'		Mineral lineation		Stretching lineation		FT		Gt split	
Outcrop #	X	Y	strike	dip	strike	dip	trend	plunge	trend	plunge	trend	plunge	trend	dip
95-NM-150	2625	1700												
95-NM-151	2550	1650	66	24										
95-NM-152	2500	1575	71	38										
95-NM-153														
95-NM-154			31	65										
95-NM-155														
95-NM-156			10	75										
95-NM-157			150	16										
95-NM-158			220	25										
95-NM-159	2600	2650	10	25			90	15						
95-NM-160	2500	2600	60	20										
95-NM-161	2375	2425	68	55										
95-NM-162	2525	2500												
95-NM-163	2525	2200												
95-NM-164	2525	1850	70	34										
95-NM-165	2600	5100	175	7										
			335	12										
			303	14										
			313	16			25	12						
95-NM-166	3075	5675	322	24			83	18			80	16		
			305	22							55	19	170	90
			315	25										
			310	25			65	25						
95-NM-167	3000	5500	279	23					80	13				
			299	18			79	11					175	90
			304	15										
95-NM-168	2875	5650	306	22					70	14				
95-NM-169	2875	5725	282	22										
95-NM-170	2825	5750	308	25										
95-NM-171	1600	5400	297	14			80	12					190	
			246	24			287	17						
95-NM-172	1575	5325	302	22										
			275	26							20	15		
			273	23	65	40					278	4		
95-NM-173	1600	5300	275	25					26	24	92	9		
			300	15										
95-NM-174	1625	5275	268	16							265	8		
			245	22			255	4						
95-NM-175	1650	5225	245	26	15	71								
			269	23										
			244	23							260	10		

Transposition-related structural elements

	Grid position		ST		ST'		Mineral lineation		Stretching lineation		FT		Gt split	
Outcrop #	X	Y	strike	dip	strike	dip	trend	plunge	trend	plunge	trend	plunge	trend	dip
95-NM-176	2100	5325	256	14			262	2						
95-NM-177	2700	5175	315	24							103	8		
			320	24			69	24						
95-NM-178	2775	5250	303	14										
95-NM-180														
95-NM-181			9	20										
95-NM-182														
95-NM-183														
95-NM-184			11	32										
95-NM-185														
95-NM-186	4850	3625												
95-NM-187	4925	3550												
95-NM-188														
95-NM-189			80	45										
			82	50									165	50
95-NM-190			52	30										
96-NM-200	3050	4800												
96-NM-201	3325	4800	299	26							74	22		
96-NM-202	3525	4975												
96-NM-203	3475	5075												
96-NM-204	3575	5000												
96-NM-205	3600	4950												
96-NM-206	3600	4900												
96-NM-207	3800	5425												
96-NM-208	3925	5425												
96-NM-209	4350	5600												
96-NM-210	2525	4525												
96-NM-211	2500	4625	290	17										
96-NM-212	2400	4575												
96-NM-213	2375	4400	265	16										
96-NM-214	2325	4475												
96-NM-215	3150	4900												
96-NM-216	3100	4800												
96-NM-217	3050	4800												
96-NM-218	3000	4500												
96-NM-219	2825	4250												
96-NM-220	2800	4275												
96-NM-221	2775	4250												
96-NM-222	2750	4300	320	10										
96-NM-223	2650	4300	48	10					130	8				

Transposition-related structural elements

	Grid position		ST		ST'		Mineral lineation		Stretching lineation		FT		Gt split	
Outcrop #	X	Y	strike	dip	strike	dip	trend	plunge	trend	plunge	trend	plunge	trend	dip
96-NM-224	2700	4125	290	8										
96-NM-225	1625	5675	295	13										
96-NM-226	1650	5825	290	16										
96-NM-227	1525	5800												
96-NM-228	1375	5800												
96-NM-229	1300	5800												
96-NM-230	1175	5850	295	22										
96-NM-231	1100	5900												
96-NM-232	1125	5975	278	19			70	6						
			280	15			80	6			73	10		
96-NM-233	1100	6075												
96-NM-234	1000	6150												
96-NM-235	950	6200												
96-NM-236	850	6275												
96-NM-237	825	6350												
96-NM-238	825	6600	10	6										
96-NM-239	850	6650												
96-NM-240	875	6700	191	27										
96-NM-241	925	6800												
96-NM-242	800	6825	280	19			42							

Post-transposition structural elements

	Grid position		Late crenulation		Intersection lin.		Late folds		Quartz veins	
Outcrop #	X	Y	strike	dip	trend	plunge	trend	plunge	strike	dip
94-NM-2	1400	1300	281	17					142	90
94-NM-3	1500	1275								
94-NM-4	2050	1000								
94-NM-5	2075	825								
94-NM-6	2020	925								
94-NM-7	2250	950								
94-NM-8	2350	1025								
94-NM-9	2825	1100			105	20				
94-NM-10	2875	1325								
94-NM-11	2900	1325			14	28				
94-NM-12	2875	1375			65	5				
94-NM-13	3025	1575								
94-NM-14	3053	1625								
94-NM-15	3100	3925								
94-NM-16	2925	4200								
94-NM-17	3225	3550								
94-NM-18	3025	3450								
94-NM-19	1775	750								
94-NM-20	1775	725								
94-NM-21	1975	900								
94-NM-22	1650	1175							30	90
94-NM-23	1700	1050							132	90
94-NM-24	2400	1425								
94-NM-25	2500	1775								
94-NM-26	2400	1300								
94-NM-27	2600	1325								
94-NM-28	2675	1450								
94-NM-29	3025	1725								
94-NM-30	3050	1600								
94-NM-31	3150	1625								
94-NM-32	3275	1600								
94-NM-33	3250	1625			97	12				
94-NM-34										
94-NM-35	2525	900			114	10				
94-NM-36	2350	875			94	20				
94-NM-37	2350	800			114	10				
94-NM-38	2250	750			108	20				
94-NM-39	2325	725								
94-NM-40	2175	625								
94-NM-41	2250	350					107	28		
94-NM-42	2225	325								
94-NM-43	2700	1025								
94-NM-44	2900	1150					110	12		
94-NM-45	3025	900	284	74	112	24				

Post-transposition structural elements

	Grid position		Late crenulation		Intersection lin.		Late folds		Quartz veins	
Outcrop #	X	Y	strike	dip	trend	plunge	trend	plunge	strike	dip
94-NM-46	3050	850			110	18				
94-NM-47	3175	775								
94-NM-48	3000	1750	318	68	110	22				
					120	130				
					112	26				
94-NM-49	3025	1575			110	18				
94-NM-50	2950	1475								
94-NM-51	2900	1400								
94-NM-52	2875	1225								
94-NM-53	2625	975			101	25				
94-NM-54	2650	1150								
94-NM-55	2950	2425								
94-NM-56	2875	2975								
94-NM-57									135	90
94-NM-58	3200	4975								
94-NM-59	3250	5025								
94-NM-60	3350	5100								
94-NM-61										
94-NM-62	2925	1900			113	24	115	20		
					115	25	113	26		
							195	15		
94-NM-63	2900	2050								
94-NM-64	2900	2150			115	28				
94-NM-65	2900	2225								
94-NM-66	2925	2275								
94-NM-67	2925	2325			100	17				
94-NM-68	4775	3700			63	35				
					70	40	19	9		
94-NM-69	4675	3650								
					88	14				
94-NM-70	4550	3600								
94-NM-71	4300	3650								
94-NM-72	2150	4725								
94-NM-73	2875	4725								
94-NM-74	3400	5175								
94-NM-75	3475	5150								
94-NM-76	3550	5150								
94-NM-77	3625	5200								
94-NM-78	3175	5275								
94-NM-79	3850	5300								
94-NM-80	4050	3775			90	40				
94-NM-81	3975	3800								
94-NM-82	3750	3750			110	29				
94-NM-83	3475	3775								

Post-transposition structural elements

	Grid position		Late crenulation		Intersection lin.		Late folds		Quartz veins	
Outcrop #	X	Y	strike	dip	trend	plunge	trend	plunge	strike	dip
94-NM-84	3425	3850								
94-NM-85	3375	3800								
94-NM-86	3300	5125								
94-NM-87	3225	5050	6	70	356	8				
94-NM-88	3225	5025								
94-NM-89	2950	4700								
94-NM-90	2950	2425			114	16				
94-NM-91	2975	2525								
94-NM-92	2950	2675	185	22	100	25				
94-NM-93	2875	2900			107	26				
94-NM-94	2950	3225								
94-NM-95	3000	3375								
94-NM-96	3175	3750			94	23				
94-NM-97	3075	3925								
94-NM-98	2625	4500			115	0				
94-NM-99	2500	4775								
94-NM-100	2675	4750								
94-NM-101	2850	4700								
94-NM-102	2850	4775								
94-NM-103	2950	4600								
94-NM-104	3925	4050								
94-NM-105										
94-NM-106										
94-NM-107	3900	4200			100	20				
94-NM-108	3675	4900								
94-NM-109	3600	4875								
94-NM-110	3525	4900								
94-NM-111	3400	4900								
94-NM-112	3550	5150			88	22				
94-NM-113	3650	5275								
94-NM-114	3675	5425								
94-NM-115	3525	2625			95	19				
					188	8				
94-NM-116	3475	2600			89	24				
94-NM-117	3275	2575	310	52	99	27				
					182	5				
94-NM-118	3200	2575			104	16				
					110	24				
94-NM-119	3175	4950								
94-NM-120	3250	4900								
94-NM-121	3250	4925								
94-NM-122	3325	4925								
94-NM-123	3500	4500								
94-NM-124	3875	4975								

Post-transposition structural elements

	Grid position		Late crenulation		Intersection lin.		Late folds		Quartz veins	
Outcrop #	X	Y	strike	dip	trend	plunge	trend	plunge	strike	dip
94-NM-125	3875	5025								
94-NM-126	4100	5475								
94-NM-127	4225	5425								
94-NM-128	3925	5250								
94-NM-129	4600	6025								
94-NM-130	4550	5950								
94-NM-131	4425	5775			35	38				
94-NM-132	4325	5525								
94-NM-133	3800	4900								
94-NM-134	4550	6650								
94-NM-135	4500	6500								
95-NM-140	1425	4825								
95-NM-141	2025	4825								
95-NM-142	2000	5000								
95-NM-143	1900	5075								
95-NM-144			310	63	5	22				
95-NM-145					115	17				
95-NM-146										
95-NM-147										
95-NM-148	2725	2025								
95-NM-149	2675	1875								
95-NM-150	2625	1700								
95-NM-151	2550	1650	318	76						
95-NM-152	2500	1575								
95-NM-153										
95-NM-154										
95-NM-155										
95-NM-156										
95-NM-157										
95-NM-158										
95-NM-159	2600	2650								
95-NM-160	2500	2600								
95-NM-161	2375	2425								
95-NM-162	2525	2500								
95-NM-163	2525	2200								
95-NM-164	2525	1850	310	69						
95-NM-165	2600	5100			325	18				
95-NM-166	3075	5675								
95-NM-167	3000	5500								
95-NM-168	2875	5650								
95-NM-169	2875	5725								
95-NM-170	2825	5750								
95-NM-171	1600	5400								
95-NM-172	1575	5325								

Post-transposition structural elements

	Grid position		Late crenulation		Intersection lin.		Late folds		Quartz veins	
Outcrop #	X	Y	strike	dip	trend	plunge	trend	plunge	strike	dip
95-NM-173	1600	5300								
95-NM-174	1625	5275								
95-NM-175	1650	5225								
95-NM-176	2100	5325								
95-NM-177	2700	5175								
95-NM-178	2775	5250								
95-NM-180										
95-NM-181										
95-NM-182										
95-NM-183										
95-NM-184										
95-NM-185										
95-NM-186	4850	3625								
95-NM-187	4925	3550								
95-NM-188										
95-NM-189					105	29				
95-NM-190										
96-NM-200	3050	4800								
96-NM-201	3325	4800								
96-NM-202	3525	4975								
96-NM-203	3475	5075								
96-NM-204	3575	5000								
96-NM-205	3600	4950								
96-NM-206	3600	4900								
96-NM-207	3800	5425								
96-NM-208	3925	5425								
96-NM-209	4350	5600								
96-NM-210	2525	4525								
96-NM-211	2500	4625								
96-NM-212	2400	4575								
96-NM-213	2375	4400								
96-NM-214	2325	4475								
96-NM-215	3150	4900								
96-NM-216	3100	4800								
96-NM-217	3050	4800								
96-NM-218	3000	4500								
96-NM-219	2825	4250								
96-NM-220	2800	4275								
96-NM-221	2775	4250								
96-NM-222	2750	4300								
96-NM-223	2650	4300								
96-NM-224	2700	4125								
96-NM-225	1625	5675								
96-NM-226	1650	5825			110	0				

Post-transposition structural elements

	Grid position		Late crenulation		Intersection lin.		Late folds		Quartz veins	
Outcrop #	X	Y	strike	dip	trend	plunge	trend	plunge	strike	dip
					20	10				
96-NM-227	1525	5800								
96-NM-228	1375	5800								
96-NM-229	1300	5800								
96-NM-230	1175	5850								
96-NM-231	1100	5900								
96-NM-232	1125	5975			20	14				
96-NM-233	1100	6075								
96-NM-234	1000	6150								
96-NM-235	950	6200								
96-NM-236	850	6275								
96-NM-237	825	6350								
96-NM-238	825	6600								
96-NM-239	850	6650								
96-NM-240	875	6700								
96-NM-241	925	6800								
96-NM-242	800	6825								